Quantendynamik von S$_N$2–Reaktionen

Dissertation

zur Erlangung des Doktorgrades
der Mathematisch–Naturwissenschaftlichen Fakultäten
der Georg–August–Universität zu Göttingen

vorgelegt von

Carsten Hennig

aus Hamburg

Göttingen, 2006

D7

Referent: Priv.–Doz. Dr. Stefan Schmatz

Korreferent: Prof. Dr. Michael Buback

Tag der mündlichen Prüfung: 01.11.2006

Quantum Dynamics of S_N2 Reactions

Dissertation

submitted to the
Combined Faculties for the Natural Sciences
and for Mathematics
of the Georg–August–Universität of Göttingen
for the degree of
Doctor of Natural Sciences

presented by

Carsten Hennig

born in Hamburg

Göttingen, 2006

Referees: Priv.–Doz. Dr. Stefan Schmatz
Prof. Dr. Michael Buback

Kurzfassung

In dieser Arbeit werden einige quantenmechanische Untersuchungen des Reaktionsmechanismus in nukleophilen bimolekularen Substitutionsreaktionen (S_N2–Reaktionen) vorgestellt. Der S_N2–Mechanismus ist sowohl für zahlreiche Gebiete der experimentellen Chemie als auch für die theoretischen Konzepte der Reaktionsdynamik von Bedeutung. Entlang der Reaktionskoordinate befinden sich in der Gasphase zwei tiefe Potentialtöpfe, und Bindungsbruch und –bildung finden gleichzeitig statt. Dadurch weist die Reaktion einige interessante Besonderheiten wie Resonanzen verschiedenen Typs und die Möglichkeit zur Rückkehr über die Barriere auf. Mittels zeitunabhängiger quantenmechanischer Streurechnungen wird der Einfluss der symmetrischen Schwingungen der Methylgruppe sowie von Rotationen des angegriffenen Methylhalogenids an zwei Beispielreaktionen in der Gasphase untersucht. Im ersten Fall kann eine aktive Teilnahme der Moden an der Reaktion festgestellt und somit das Konzept der Beobachtermoden dafür in Frage gestellt werden. Der zweite Fall zeigt die Bedeutung der Kopplung der Rotationsbewegung mit den reaktiven Freiheitsgraden.

Abstract

This thesis presents quantum mechanical investigations of the mechanism involved in nucleophilic bimolecular substitution reactions (S_N2 reactions). The S_N2 mechanism is important both for applications in a wide field of chemistry as well as for the theoretical concepts in reaction dynamics. In the gas phase, the presence of two deep wells in the reaction profile before and after passage of the central barrier and the simultaneous breaking and forming of bonds give rise to several interesting features like resonances of different types and the possibility of recrossing the barrier. Time–independent quantum mechanical scattering theory is applied to investigate the role of the symmetric vibrations of the methyl group and of rotations of the attacked methyl halide for two model reactions in the gas phase. While the former can be shown to actively participate in the reaction, questioning the spectator mode concept in this case, the investigation of the latter reveals the importance of the coupling of rotational motion with the reactive degrees of freedom.

Contents

Chapter 1

Introduction

Nucleophilic bimolecular substitution reactions (S_N2 reactions) are of high practical as well as fundamental significance in organic chemistry, physical chemistry, biology and medicine. An example for such a process is the synthesis of adrenaline from noradrenaline (see Fig. 1.1). While the molecules involved are themselves fairly large from the point of view of theoretical chemistry, only a small part of them actually takes part in the reaction. To be more specific, Fig. 1.2 shows the essential steps in the reaction for the synthesis of synephrine from octopamine, which differ only by a hydroxyl group on the opposite part of the molecules from noradrenaline and adrenaline, respectively. The key step is the nucleophilic attack of an amino group on the dipolar part of the enzyme acting as a methyl donor. For a generic theoretical modeling, we can thus simplify the reactants to a halogenide anion attacking a dipolar methyl halide in the gas phase (see Fig. 1.3).

Such S_N2 reactions in the gas phase have attracted a huge interest over the past decade that manifests itself by four review articles that appeared between 1994 and 2004 [1, 2, 3, 4]. The halogen exchange Walden inversion reactions

$$X^- + CR_3Y \rightarrow XCR_3 + Y^- \tag{1.1}$$

(X, Y: halogen atoms; R: hydrogen or organyl) as prototype S_N2 reactions have been the subject of extensive experimental as well as theoretical investigations (see Refs. [7, 8, 9, 10, 11, 12, 13, 14, 15, 16, 17, 18, 19, 20, 21, 22, 23, 24, 25, 26, 27, 28, 29, 31, 89, 90, 91, 92, 96, 97] and references cited in Refs. [1, 2, 3, 4]).

The S_N2 mechanism involves the simultaneous making and breaking of two single bonds and can be regarded as a simple and exemplary elementary chemical reaction. Most other important reaction mechanisms in organic and inorganic chemistry involve double bonds and the existence of several chemically stable intermediates. The latter are not present in reactions that proceed according to the S_N2 mechanism so that they are particularly well suited for a detailed quantum–dynamical investigation.

Gas–phase S_N2 reactions are governed by Feshbach and sometimes, e.g. in the system $Cl^- + CH_3Br$ [32], also shape resonances that are connected with relatively stable intermediate structures created by the strong electrostatic attraction between
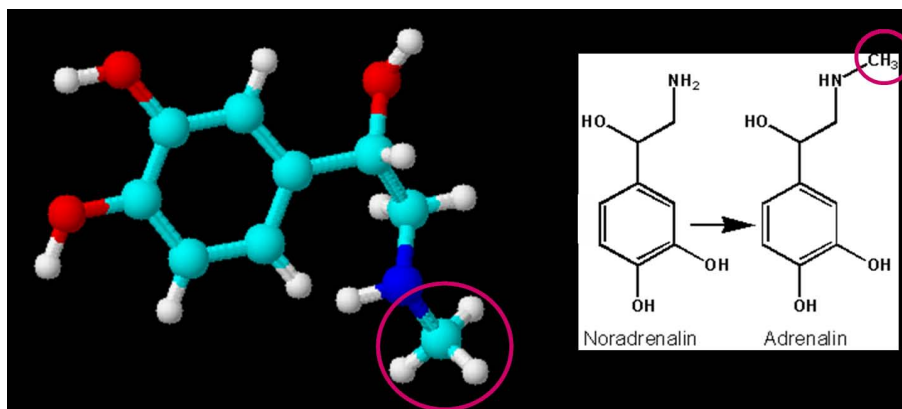
Figure 1.1: Synthesis of adrenaline from noradrenaline by addition of a methyl group which proceeds via an S_N2 mechanism [5].
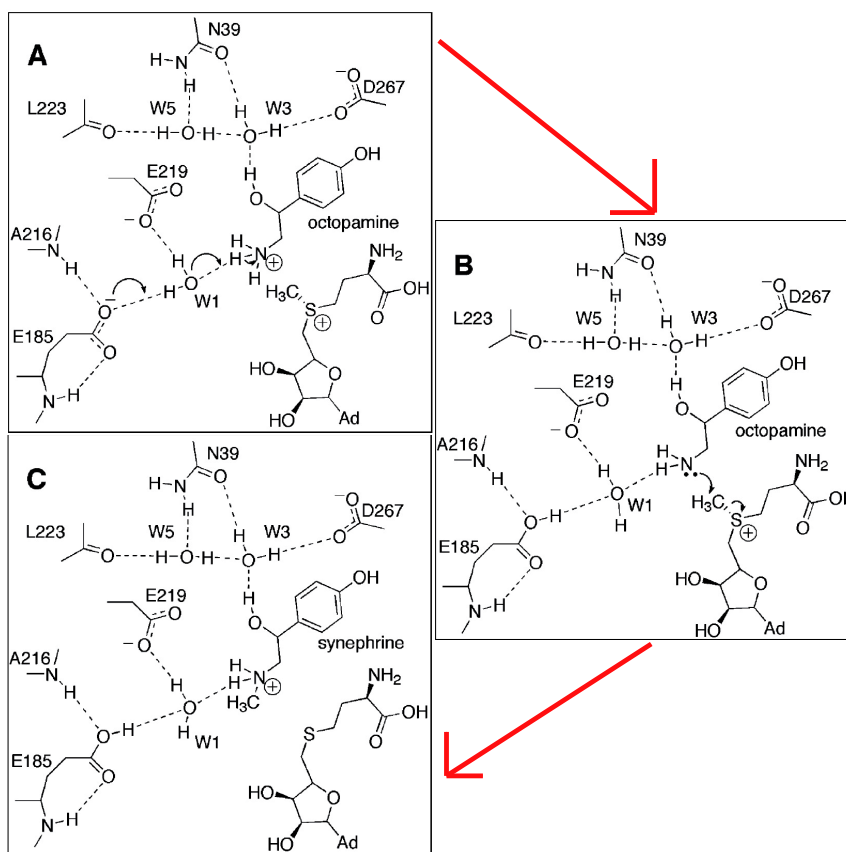

Figure 1.2: Detailed steps in the synthesis of synephrine from octopamine [6].
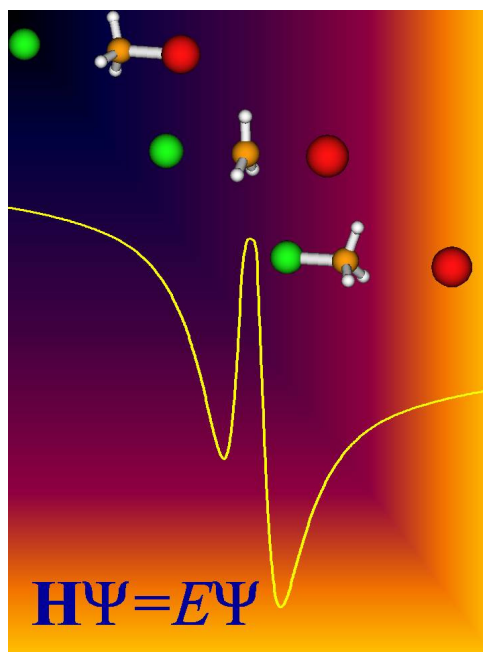
Figure 1.3: Potential along the reaction coordinate for the Cl–Br exchange reaction $Cl^- + CH_3Br \rightarrow Br^- + CH_3Cl$ (see [102]).

the attacking nucleophile, mostly an ion, and the dipolar substrate molecule, often a methyl halide. As is well known [1, 2, 3, 4, 7, 8, 9], two relatively deep wells (ca. 0.5 eV) are present in the reaction profile that correspond to two complexes $X^- \cdots CH_3Y$ and $XCH_3 \cdots Y^-$ being formed before and after passage of the central barrier.

It was shown by Hase and co–workers in a series of papers on classical dynamics calculations on these reactions [20, 21, 22, 25, 26, 27, 28, 30, 97] that there is only a very limited energy flow between the inter– and intramolecular modes of the collision complex so that a detailed quantum–dynamical study is required. In particular, it is worth investigating whether excitation of particular vibrational and/or rotational modes in the reactant molecule result in a non–negligible influence on the reactivity in gas–phase S_N2 reactions. Moreover, state–selected reaction probabilities and cross sections give valuable information on vibrational and/or rotational product distributions.

This thesis presents quantum mechanical studies on two model systems, the symmetric chlorine–chlorine exchange reaction

$$Cl^- + CH_3Cl' \rightarrow ClCH_3 + Cl'^-$$
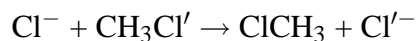
and the exothermic bromine–chlorine substitution

$$Cl^- + CH_3Br \rightarrow ClCH_3 + Br^-.$$
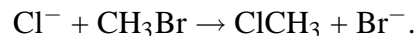
Using time–independent quantum mechanical scattering theory, the symmetric vibrations of the methyl group (umbrella bend and C–H stretch) are treated exactly within

C_{3v} symmetry for the first time, shedding more light on the active role of the methyl group in the Walden inversion. In addition, methods and results on the inclusion of the rotational motion of the methyl halide are shown, providing the first state–selective treatment of spatial degrees of freedom beyond collinearity in heavy six–atom reactions with long–range interaction potentials. For that purpose, numerical techniques are presented in detail and suitable extensions are proposed.

Chapter 2

Theoretical Framework

The technical goal of the calculations is to obtain complete asymptotic scattering information about the processes via computation of the **S**–matrix. As the reactions under study do not possess a unique time scale due to the many resonances the lifetimes of which vary over several orders of magnitude, time–independent scattering theory is used. In the implementation, we essentially need to solve the time–independent Schroedinger equation for the nuclei in the potential given by the energy of the electronic ground state in the Born–Oppenheimer approximation. This energy, in turn, can be calculated by standard program packages and will not be considered here.

The first section provides the coordinates used and the corresponding Hamiltonians, the second briefly summarizes the scattering formalism and the third gives an outline of the possible strategies to handle rotation of the diatom system.

2.1 Coordinate Systems and Hamiltonians

2.1.1 Jacobi Coordinates

Collinear System

The dynamically essential degrees of freedom (the bonds being broken and formed) are well described by Jacobi coordinates r and R which easily incorporate the conservation of center of mass and avoid mixed derivatives in the Hamiltonian. In a three–atom system, r is the distance of two of the particles and R the distance of the third from the center of mass of the other two (see Fig. 2.1).

For the collinear calculations, the two doubly–degenerate symmetric vibrations of the methyl group are additionally included, yielding a complete and exact description within C_{3v} symmetry. The methyl group is treated as a kinematically independent system with the center of mass of the CH_3 group as origin. Its internal motion is then described by the two coordinates $z = r_{CH} \cos(\theta)$ and $q = r_{CH} \sin(\theta)$ (see Fig. 2.1) that correspond to the motion of the center of mass of the H_3 unit against the carbon atom
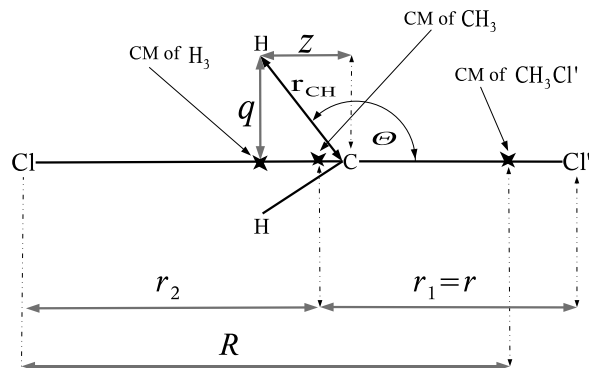
Figure 2.1: Definition of the coordinate system for the four–dimensional collinear calculations.

(z) and the 'breathing' motion of the D_{3h}–symmetric H_3 unit in a plane perpendicular to the molecular axis of symmetry (q).

In these coordinates, the kinetic energy is completely decoupled and the Hamiltonian reads

$$\hat{H} = -\frac{\hbar^2}{2\mu_1}\frac{\partial^2}{\partial R^2} - \frac{\hbar^2}{2\mu_2}\frac{\partial^2}{\partial r^2} - \frac{\hbar^2}{2\mu_3}\frac{\partial^2}{\partial z^2} - \frac{\hbar^2}{2\mu_4}\frac{\partial^2}{\partial q^2} + V(R,r,z,q), \qquad (2.1)$$

where the reduced masses are given by

$$\mu_1 = \frac{m_X m_{CH_3Y}}{m_X + m_{CH_3Y}}, \qquad (2.2)$$

$$\mu_2 = \frac{m_{CH_3} m_Y}{m_{CH_3} + m_Y}, \qquad (2.3)$$

$$\mu_3 = \frac{3 m_H m_C}{3 m_H + m_C}, \qquad (2.4)$$

and

$$\mu_4 = 3 m_H. \qquad (2.5)$$

Here, m_X and m_Y denote the masses of the two halogen atoms (i.e. the isotopes ^{35}Cl or ^{79}Br) and m_C and m_H refer to the masses of the carbon and hydrogen atoms. $V(R,r,z,q)$ is the energy of the electronic ground state with the nuclei at the positions specified by (R,r,z,q).

Three–Dimensional Coordinates

To properly treat the rotation of the diatomic part, we additionally include the angle γ describing the position of the third particle w.r.t. the diatom (see Fig. 2.2) and omit the

Figure 2.2: Definition of the coordinate system including rotation.

two degrees of freedom of the methyl group. The remaining degree of freedom needed for a complete description of the system on the three–particle level (the azimuthal rotation of the diatom) can be handled as being purely dynamical.
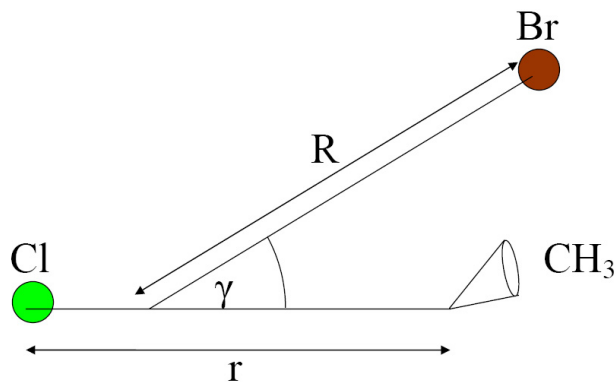
The full Hamiltonian $\hat{H} = \hat{H}^{J=0} + \hat{H}^J + \hat{V}$ then consists of [34]

$$\hat{H}^{J=0} = \delta_{j'j}\delta_{k'k}\left[-\frac{\hbar^2}{2\mu_1}\frac{\partial^2}{\partial R^2} - \frac{\hbar^2}{2\mu_2}\frac{\partial^2}{\partial r^2} + \frac{\hbar^2}{2}j(j+1)\left(\frac{1}{\mu_1 R^2} + \frac{1}{\mu_2 r^2}\right)\right], \qquad (2.6)$$

$$\hat{H}^J = \delta_{j'j}\delta_{k'k}\frac{\hbar^2}{2\mu_1 R^2}[J(J+1) - 2k^2] - \delta_{j'j}\delta_{k'k\pm1}\frac{\hbar^2}{2\mu_1 R^2}C_{Jk}^{\pm}C_{jk}^{\pm}, \qquad (2.7)$$

$$\hat{V} = \delta_{k'k}\langle j'k|V(R,r,\gamma)|jk\rangle_\gamma \qquad (2.8)$$

where in the second part

$$C_{jk}^{\pm} = \sqrt{j(j+1) - k(k\pm1)}.$$

In these equations, J denotes the conserved total angular momentum quantum number, $j = 0, 1, \ldots$ the angular momentum quantum number of the rotating diatom and $k = -J, \ldots, J$ is the quantum number of the projection of the total angular momentum $\hat{\mathbf{J}}$ onto the body–fixed axis defined by the third atom and the center of mass of the diatom. $|jk\rangle$ denotes a spherical harmonic and $\langle\ldots\rangle_\gamma$ indicates integration over γ.

The angular momentum quantum numbers j and k act as dynamical variables, resulting in a four–dimensional Hamiltonian. In principle, taking conservation of total angular momentum and center of mass into account, three coupled degrees of freedom should suffice; however, removing all Coriolis couplings is possible only if at most one large amplitude motion exists [33].

$\hat{H}$ contains terms which become singular for $r \to 0$ or $R \to 0$. While the first represent physical singularities (vanishing distance of two particles) and thus pose no problems, the second are due to the non–Cartesian coordinate system (Eckart singularities). They do not lead to infinite energies, but cancel each other. This cancellation, however, should be treated with care in any numerical calculation.

2.1.2 Hyperspherical Coordinates

In Jacobi coordinates, each of two variables r and R may become infinite to describe different asymptotic configurations. As it is desirable to have a single reaction coordinate only, a transformation to hyperspherical coordinates [35, 36, 37, 38, 39, 40] (ρ, δ) is made by the simple formulas

$$\rho = \sqrt{\tilde{R}^2 + \tilde{r}^2}, \tag{2.9}$$
$$\delta = \arctan\left(\frac{\tilde{r}}{\tilde{R}}\right),$$

where

$$\tilde{r} = \sqrt{\frac{\mu_2}{\mu}}r, \tilde{R} = \sqrt{\frac{\mu_1}{\mu}}R \text{ and } \mu = \sqrt{\mu_1 \mu_2}.$$

The Hamiltonian for the collinear calculation becomes[1]

$$\hat{H} = -\frac{\hbar^2}{2\mu}\left(\frac{\partial^2}{\partial\rho^2} + \frac{1}{4\rho^2}\right) + \hat{H}_{\text{surf}} \tag{2.10}$$

with the parametrically ρ–dependent surface Hamiltonian

$$\hat{H}_{\text{surf}}(\rho) = -\frac{\hbar^2}{2}\left(\frac{1}{\mu\rho^2}\frac{\partial^2}{\partial\delta^2} + \frac{1}{\mu_3}\frac{\partial^2}{\partial z^2} + \frac{1}{\mu_4}\frac{\partial^2}{\partial q^2}\right) + V(\delta, z, q; \rho). \tag{2.11}$$

To include rotation, we have now $\hat{H}_{\text{surf}} = \hat{H}_{\text{surf}}^{J=0} + \hat{H}_{\text{surf}}^J + \hat{V}$ with

$$\hat{H}_{\text{surf}}^{J=0} = \delta_{j'j}\delta_{k'k}\left[-\frac{\hbar^2}{2\mu\rho^2}\frac{\partial^2}{\partial\delta^2} + \frac{\hbar^2}{2}j(j+1)\left(\frac{1}{\mu\rho^2\cos^2\delta} + \frac{1}{\mu\rho^2\sin^2\delta}\right)\right], \tag{2.12}$$

$$\hat{H}_{\text{surf}}^J = \delta_{j'j}\delta_{k'k}\frac{\hbar^2}{2\rho^2\cos^2\delta}[J(J+1) - 2k^2] - \delta_{j'j}\delta_{k'k\pm1}\frac{\hbar^2}{2\rho^2\cos^2\delta}C_{Jk}^{\pm}C_{jk}^{\pm}, \tag{2.13}$$

$$\hat{V} = \delta_{k'k}\langle j'k|V(\delta, \gamma; \rho)|jk\rangle_\gamma. \tag{2.14}$$

2.2 Scattering Formalism

In time–independent scattering theory, we are searching for a solution ψ of the time–independent Schroedinger equation at fixed energy E which represents asymptotically a free incoming plain wave (the reactants) and a scattered spherical wave (the products). We thus impose the boundary condition

$$g_{nm}^J(R) \sim \delta_{nm}e^{-i(k_n R - l_n\pi/2)} - \sqrt{\frac{k_n}{k_m}}S_{nm}^J e^{i(k_m R - l_m\pi/2)} \tag{2.15}$$

---

[1]This requires the wave function $\psi(\rho, x)$ to be normalized according to $\int |\psi(\rho, x)|^2 \, d\rho \, dx = 1$, where x collectively denotes the remaining degrees of freedom [41].

for $R \to \infty$, initial state n and final state m. k_n is the wavenumber corresponding to energy E and state n, l_n the orbital angular momentum quantum number corresponding to state n and total angular momentum J. $g_{nm}^J(R)$ denotes the radial part of an expansion of the wavefunction ψ_n^J,

$$\psi_n^J = \frac{1}{R} \sum_m g_{nm}^J(R) \phi_m^J(x). \tag{2.16}$$

The $\phi_m^J(x)$ are "surface" functions depending on all other coordinates collectively denoted by x.

In Eq. (2.15), S_{nm}^J is an element of the **S**-matrix which yields reaction probabilities P_{nm}^J via $P_{nm}^J = |S_{nm}^J|^2$. Total state–selective cross sections σ_{nm} can be computed as

$$\sigma_{nm} = \frac{\pi}{k_n^2} \sum_J (2J+1) P_{nm}^J \tag{2.17}$$

and (exact) rate constants are obtained by

$$k(T) = \frac{1}{hQ_r} \int_0^\infty e^{-E/(k_\mathrm{B}T)} P_\mathrm{cum}(E) \mathrm{d}E \tag{2.18}$$

where $P_\mathrm{cum} = \sum_{i,j} P_{ij}$ and Q_r is the partition function per unit volume for the reactants.

The **S**–matrix elements themselves provide additional information about time delays [42] and differential cross sections.

2.3   Strategies for the Treatment of Rotation

In the definition of the Jacobi coordinates, we can choose any two of the three particles to be the diatom and the other one to be the single atom the position of which is described by (R, γ). The three possible choices yield three different coordinate systems, and each of these is asymptotically well suited to describe one of the possible reactant/product configurations. This implies that for reactive scattering at least two different coordinate systems need to be related in the interaction region which poses the key challenge in this field of research. Fortunately, the hyperradius ρ can be shown to be independent of the coordinate system: For a given physical configuration of the molecules, all three pairs of Jacobi coordinates yield the same radius. For collinear scattering, also the hyperangle δ can be easily related by a shift and all coordinate systems can be treated on an equal footing. If we deviate from collinearity, the transformation of the coordinates (R, r, γ) into another system involves all three of them in a more complicated manner (see [43] for a detailed presentation), and each set of coordinates is well suited for one configuration only.

There are several different approaches to this problem in the literature. First, one can define adiabatically adjusting, principal axis hyperspherical coordinates [44]

which treat all arrangements equivalently. In addition, they can avoid Eckart singularities in linear transition state configurations. However, the Hamiltonian contains a mixed derivative, and the transformation to Jacobi coordinates needed for the boundary condition in the asymptotic region is more complicated. Fortunately, for S_N2 systems, in the configurations leading to singular terms in the Hamiltonian both halogen atoms are on the same side of the methyl group; therefore, this situation is important for high energies only. Other sets of hyperspherical coordinates can be used which are also less biased towards one of the arrangement configurations (cf. [45]); however, the drawback will be a more complicated transformation to the appropriate asymptotic coordinates.

Second, the wavefunctions can be computed in different coordinate systems and be connected by computing an overlap matrix [38]. This requires the choice of reference potentials which might be critical for a proper description of the interaction region.

In this thesis, we use a third approach to compute the wavefunctions based on one of the (biased) hyperspherical coordinate systems in the interaction region. This method has already been used directly in Jacobi coordinates [54]. By a proper basis set adaptation, we can still accurately describe all arrangement configurations. For an exact Hamiltonian, at fixed hyperradius ρ all arrangement channel coordinates will yield the same eigenstates (with a different parametrization) such that matching onto the (different) asymptotic coordinate systems is feasible once the interaction region is left.

Chapter 3

Numerical Methods

This chapter treats the different numerical strategies employed in the calculations. We first outline the solution of the scattering problem after eigenfunctions have been computed. The following sections deal with the necessary basis set techniques which are crucial for a satisfactory performance. As a conceptually complete review could not be found, the presentation is set to derive the algorithm from general principles of orthogonal polynomials as it was first discovered in [50]. The text should give information on the efficient implementation of this method and bridge the gap between the mathematical and the physical point of view. The last section gives material about diagonalization techniques and possible combinations of these to achieve an improved performance for the systems under study.

3.1 R–Matrix Propagation

In solving the scattering problem, we used the technique of $\mathbf{R}$–matrix propagation [46]. The $\mathbf{R}$–matrix relates a matrix valued wavefunction ψ_{nm} and its derivatives by $\mathbf{R}\psi' = \psi$. If such a matrix $\mathbf{R}_{\mathrm{asym}}$ is available asymptotically, the $\mathbf{S}$–matrix can be obtained by

$$\mathbf{S} = (\mathbf{R}_{\mathrm{asym}}\mathbf{O}' - \mathbf{O})^{-1}(\mathbf{R}_{\mathrm{asym}}\mathbf{I}' - \mathbf{I}), \tag{3.1}$$

where $\mathbf{I}$ and $\mathbf{O}$ are diagonal matrices representing the incoming and outcoming waves, resp., according to Eq. (2.15). The advantage of using the $\mathbf{R}$–matrix lies in the fact that it is stable and not affected by the exponential behavior of closed (energetically forbidden) channels.

For exact results, $\mathbf{R}_{\mathrm{asym}}$ needs to be obtained at a large value of the Jacobi coordinate R. However, if only reaction probabilities are needed, it is usually sufficient to evaluate the $\mathbf{S}$–matrix directly in hyperspherical coordinates ρ and average [40].

For the construction of $\mathbf{R}_{\mathrm{asym}}$, the reaction coordinate ρ is divided into small sectors with midpoints[1] ρ_i. For each ρ_i, the wavefunction is expanded in a finite product

---

[1]This puts some restriction on the distribution of the ρ_i and the equations should be rewritten if

basis similar to the infinite expansion (2.16),

$$\psi_n(\rho;\rho_i) = \frac{1}{\rho} \sum_{m=1}^{N_{\text{ch}}} g_{nm}(\rho;\rho_i)\phi_m(x;\rho_i). \tag{3.2}$$

Note that an additional factor of $\rho^{-1/2}$ has to be included if the explicitly ρ–dependent terms in (2.10) are written in the form obtained by directly transforming the differential operator from Jacobi to hyperspherical coordinates (using the normalization $\int |\psi(\rho,x)|^2 \rho \, d\rho \, dx = 1$).

The surface functions $\phi_m(x;\rho_i)$ depend parametrically on the hyperradius ρ. If they are chosen to be eigenfunctions of the surface Hamiltonian $\hat{H}_{\text{surf}}(\rho)$,

$$\hat{H}_{\text{surf}}(\rho)\phi_m(x;\rho_i) = \varepsilon_m(\rho_i)\phi_m(x;\rho_i), \tag{3.3}$$

insertion of the finite expansion (3.2) in the Schroedinger equation $\hat{H}\psi = E\psi$ will yield decoupled equations for the $g_{nm}(\rho;\rho_i)$:

$$\frac{d^2 \tilde{\mathbf{g}}_n(\rho;\rho_i)}{d\rho^2} + \mathbf{W}(\rho_i)\tilde{\mathbf{g}}_n(\rho;\rho_i) = 0 \tag{3.4}$$

where the column vector $\tilde{\mathbf{g}}_n$ contains the elements g_{nm}/ρ and the matrix $\mathbf{W}$ is given by

$$W_{mn}(\rho_i) = \left[\frac{2\mu}{\hbar^2} \left(E - \varepsilon_n(\rho_i) \right) - \frac{1}{4\rho_i^2} \right] \delta_{mn}. \tag{3.5}$$

These are easily solved to give a local $\mathbf{R}$–matrix in each sector. By continuity requirements of the wavefunction and its derivative at the boundary of each sector, a global $\mathbf{R}$–matrix can be assembled (cf. [46]). For that purpose, the surface eigenfunctions $\phi_m(x;\rho_i)$ for adjacent sectors ρ_{i-1}, ρ_i will have to be mapped to each other by virtue of their overlap matrix elements $O_{mn}^{(i-1,i)}$,

$$O_{mn}^{(i-1,i)} = \langle \phi_m(x;\rho_{i-1}) | \phi_n(x;\rho_i) \rangle. \tag{3.6}$$

These, in turn, do not depend on energy and need to be computed only once.

3.2   Collocation Method: Basic Properties

3.2.1   A Simple Example

Consider the linear differential operator in one dimension

$$\hat{D} = -(1-x^2)\frac{\partial^2}{\partial x^2} + 2x\frac{\partial}{\partial x}, \; x \in [-1,1]. \tag{3.7}$$

---

arbitrary ρ_i are needed, e.g. when avoided crossings are traced.

It results from the "ϑ"–part of $-\hat{\Delta}$ with $\hat{\Delta}$ being the Laplace operator in spherical coordinates,

$$\hat{\Delta} = \frac{1}{r^2}\frac{\partial}{\partial r}r^2\frac{\partial}{\partial r} + \underbrace{\frac{1}{r^2\sin\vartheta}\frac{\partial}{\partial\vartheta}\sin\vartheta\frac{\partial}{\partial\vartheta}} + \frac{1}{r^2\sin^2\vartheta}\frac{\partial^2}{\partial\varphi^2},$$

by setting $r = 1$ and substituting $x = \cos\vartheta$. Its eigenfunctions are well known: The Legendre polynomials P_l, given by the recurrence relation

$$(l+1)P_{l+1}(x) = (2l+1)xP_l(x) - lP_{l-1}(x)$$

and $P_0(x) = 1$, $P_1(x) = x$. They are orthogonal on the interval $[-1,1]$ with the normalization factors $\gamma_i = 2/(2i+1)$,

$$\int\limits_{-1}^{1} P_i(x)P_j(x)\,\mathrm{d}x = \underbrace{\frac{2}{2i+1}}_{=\gamma_i}\delta_{ij},$$

and satisfy $\hat{D}P_l = l(l+1)P_l$.

Suppose we intend to solve a differential equation which is in some sense derived from $\hat{D}$, for example an inhomogeneous equation like

$$\hat{D}u = g \tag{3.8}$$

for some function g on $[-1,1]$ or an eigenvalue problem $\tilde{\hat{D}}u = \lambda u$ for the modified operator $\tilde{\hat{D}}$,

$$\tilde{\hat{D}} = \hat{D} + V(x). \tag{3.9}$$

Instead of using a "black–box"–method like finite differences or finite elements to locally approximate the solution u, it is tempting to expand the solution in terms of the known eigenfunctions of $\hat{D}$,

$$u(x) = \sum_{l=0}^{\infty} a_l P_l(x), \tag{3.10}$$

and determine the expansion coefficients a_l. The basis used to expand the solution (the Legendre polynomials in this case) will be call the *trial functions* in the following. Contrary to the basis functions used in finite elements or finite differences, they are global functions. As they are derived as eigenfunctions of an associated operator, the method is termed *spectral method*.

To be able to solve numerically for the coefficients a_l, one first needs a finite expansion for u and cut the series (3.10) after the first N terms,

$$u_N^P := \sum_{l=0}^{N-1} a_l P_l(x). \tag{3.11}$$

Formally, u_N^P is obtained by applying a projection operator $\hat{P}_N$ to u, $\hat{P}_N u = u_N^P$, where $\hat{P}_N$ will project each continuous function onto the first N Legendre polynomials, i.e. in Dirac notation

$$\hat{P}_N := \sum_{l=0}^{N-1} |P_l><P_l|. \tag{3.12}$$

The efficiency of the method will depend on the convergence speed of the expansion (3.10) which, in turn, is determined by the decay rate of the expansion coefficients a_l. In the next section, we can see in a quite general setting that our ansatz is promising.

3.2.2   Spectral Accuracy

Suppose we have some linear differential operator $\tilde{\hat{D}}$ and we would like to solve a differential equation

$$\tilde{\hat{D}}u = g. \tag{3.13}$$

If we know the eigenfunctions ϕ_k of a "similar" operator $\hat{D}$,

$$\hat{D}\phi_k = \lambda_k \phi_k, \tag{3.14}$$

then it is reasonable to expand the solution u of the differential equation (3.13) in terms of the ϕ_k:

$$u = \sum_k u_k \phi_k. \tag{3.15}$$

If the eigenfunctions of $\hat{D}$ are orthonormal w.r.t. a scalar product $(,)$, the expansion coefficients u_k are obtained from $u_k = (u, \phi_k)$. Now, if the operator is hermitian, we can write

$$u_k = (u, \phi_k) = \frac{1}{\lambda_k}(u, \hat{D}\phi_k) = \frac{1}{\lambda_k}(\hat{D}u, \phi_k)$$

and by iteration

$$u_k = \frac{1}{\lambda_k^m}(\hat{D}^m u, \phi_k)$$

for every $m \geq 1$. If $\hat{D}^m u$ is still "well–behaved", i.e. $\|\hat{D}^m u\|$ exists, we get by Cauchy–Schwarz the inequality

$$|u_k| \leq \frac{1}{|\lambda_k|^m}\|\hat{D}^m u\|. \tag{3.16}$$

If the eigenvalues λ_k grow at least like k^α, $\alpha > 0$ (which is the case for the usual orthogonal polynomials) and $\|\hat{D}^m u\|$ remains bounded for $m \to \infty$, the expansion coefficients $|u_k|$ will decay faster than any inverse power of k (*exponential convergence, spectral accuracy*).

The main assumptions made in this argument concern the hermiticity of the operator $\hat{D}$ and the growth of $\|\hat{D}^m u\|$. The first assumption can be closely related to appropriate boundary conditions if we think in terms of partial integration. For the

second, note that the expansion coefficients u_k can be linked to the difference $\hat{D} - \tilde{\hat{D}}$ of the operators $\hat{D}$ and $\tilde{\hat{D}}$ and also to the expansion coefficients of g:

$$u_k = (u, \phi_k) = \frac{1}{\lambda_k}(\hat{D}u, \phi_k) \quad = \quad \frac{1}{\lambda_k}\big(((\hat{D} - \tilde{\hat{D}}) + \tilde{\hat{D}})u, \phi_k\big)$$

$$= \quad \frac{1}{\lambda_k}\big((\hat{D} - \tilde{\hat{D}})u + g, \phi_k\big).$$

In general, spectral accuracy is an asymptotic statement for large k, i.e. it need not imply an efficient numerical behavior. However, if the trial functions ϕ_k are chosen properly, fast convergence will in practice often be achieved [47, 67]. An example is given in Sec. 3.4.3. In theory, the expansion coefficients of Tschebyscheff series of entire functions converge to zero even faster than exponential; in case of singularities off the real line, the convergence is exponential, and with singularities in the domain of definition $[-1, 1]$, only algebraic convergence is achieved (see [48] for a brief summary and further references).

3.2.3   Generating a Matrix Representation

To generate a numerical solution for our examples in Eq. (3.8) or (3.9), resp., we will substitute u by the finite expansion u_N^P, Eq. (3.11),

$$\hat{D}u_N^P(x) \approx g(x), \tag{3.17}$$

or

$$(\hat{D} + V(x))u_N^P(x) \approx \lambda u_N^P(x), \tag{3.18}$$

and then solve for the expansion coefficients a_l, $l = 0, \ldots, N - 1$. For this purpose, additional procedures have to be invented to reduce each remaining trial function to a finite set and to ensure that the approximate solution will satisfy the differential equation as closely as possible. The various choices for minimizing the residual error will create the difference between one spectral method and another. In general, the obtained solutions $\tilde{a}_l$, $l = 0, \ldots, N - 1$ will differ from the coefficients a_l in the exact solution and depend on the procedure invented.

One possibility is to form matrix elements with *test functions* and solve the resulting matrix equation or matrix eigenvalue problem, respectively. If we use the trial functions as test functions, the approach is called *Galerkin* in the context of fluid dynamics [47], *variational* or a *Variational Basis Representation (VBR)* in quantum mechanics [60]. (The procedure is essentially the same as for finite elements, the difference lies in the choice of the functions.) We obtain a system of linear equations for the expansion coefficients $\tilde{a}_l$ which in matrix form reads for (3.17)

$$D_{lm}\tilde{a}_m = g_l \tag{3.19}$$

with

$$D_{lm} = l(l+1)\gamma_l\delta_{lm}, \tag{3.20}$$

$$g_l = (P_l, g)_{L^2[-1,1]}. \tag{3.21}$$

While this system is immediately solvable, we get for the second example (3.18) an eigenvalue problem for the matrix

$$\tilde{D}_{lm} = l(l+1)\gamma_l\delta_{lm} + (P_l, VP_m)_{L^2[-1,1]}. \tag{3.22}$$

In the variational approach it is assumed that the integrals for the matrix elements are computed exactly (or at least with a negligible error). If we allow the integration to be performed with finite precision (for example, using a quadrature formula with N points x_i, $1 \le i \le N$), the resulting matrix representation of the differential equation is called *Finite Basis Representation (FBR)* in quantum mechanics. The quadrature formula is applied only to those terms which cannot be determined exactly; usually, these are matrix elements of functions. Denoting the $L^2[-1,1]$ scalar product in the quadrature approximation by $(,)_N$, the first example becomes

$$D_{lm}\tilde{a}_m = g_l^N \tag{3.23}$$

with $g_l^N = (P_l, g)_N$; the second is then an eigenvalue problem for

$$\tilde{D}_{lm}^P = l(l+1)\gamma_l\delta_{lm} + (P_l, VP_m)_N. \tag{3.24}$$

Another strategy which at first glance is completely different is to enforce the differential equation in Eq. (3.17) or (3.18) only at discrete points x_i, $1 \le i \le N$, instead of computing matrix elements:

$$D_{ij}^C u_N^P(x_j) = g(x_i) \tag{3.25}$$

or

$$D_{ij}^C u_N^P(x_j) + V(x_i)u_N^P(x_i) = \lambda u_N^P(x_i), \tag{3.26}$$

respectively. (Formally, we can use delta–functions $\delta(x - x_i)$ as test functions to arrive at these equations). The unknowns to solve for are the function values $u(x_i)$ at the *collocation points* x_i instead of the expansion coefficients a_l. This approach is denominated *collocation method* in fluid dynamics or *Discrete Variable Representation (DVR)* in quantum mechanics. Evaluation of the derivative terms $\mathbf{D}^C$ in (3.25) or (3.26) needs an explanation. It will be clarified by a crucial connection between collocation methods and finite basis representations: For orthogonal polynomials and Gauss quadrature points as collocation points, there is a simple orthogonal transformation relating the two approaches. The advantage of collocation methods is then the sparsity of the representing matrices in several dimensions, as can be guessed from (3.26).

3.3   Collocation Method and Orthogonal Polynomials

3.3.1   Orthogonal Polynomials

Collocations methods can be best understood in the framework of orthogonal polynomials. For this reason we first collect some properties of these, following [51].

Basic Properties

Orthogonal polynomials are a sequence $\phi_n(x)$, $n = 0, 1, 2, \ldots$, of polynomials which are orthogonal w.r.t. a weight function $w(x)$ on an interval $[a, b]$. More precisely:

Definition 3.3.1 *A weight function* $w : [a, b] \rightarrow \mathbb{R}_{\geq 0}$ *is a nonnegative function on a finite or infinite interval* $[a, b]$ *for which all moments* μ_n *exist and are finite:*

$$\mu_n := \int_a^b x^n w(x)\, dx < \infty \quad (n = 0, 1, 2, \ldots). \tag{3.27}$$

In addition, we require $\mu_0 > 0$.

For continuous functions f, g on $[a, b]$ every weight function defines a scalar product (f, g) by

$$(f, g)_w := \int_a^b f(x)g(x)w(x)\, dx. \tag{3.28}$$

The resulting notion of orthogonality can be used to orthonormalize the linear independent polynomials $1, x, x^2, \ldots$ by the Gram–Schmidt–procedure, resulting in an orthonormal sequence $\{\phi_n(x)\}_0^\infty$ where $\phi_j(x)$ is of (exact) degree j. The only remaining ambiguity is a choice of sign. If we require the highest coefficient k_n of $\phi_n(x)$ to be positive, we finally obtain

Theorem 3.3.1 *For every weight function w there is exactly one sequence $\{\phi_n(x)\}_0^\infty$ of polynomials satisfying ($m, n \geq 0$)*

$$(\phi_m, \phi_n)_w = \delta_{mn}, \tag{3.29}$$
$$\phi_n \text{ is of exact degree } n, \tag{3.30}$$
$$k_n > 0 \ (k_n : \text{ highest coefficient of } \phi_n). \tag{3.31}$$

As $\{\phi_j(x)\}_0^{n-1}$ ($n \geq 1$) form a basis of the space $\mathbb{P}_{n-1}$ of polynomials of degree $n-1$, we can conclude

Corollary 3.3.1 ϕ_n *is orthogonal to every polynomial in* $\mathbb{P}_{n-1}$ *($n = 1, 2, \ldots$).*

Of specific importance are the zeros of the polynomials ϕ_n. A priori, they might be outside of the interval $[a, b]$ or even be complex. However, one can show that

Theorem 3.3.2 *The n zeros of the polynomials ϕ_n are real, distinct and contained in the interval (a, b) ($n = 0, 1, 2, \ldots$).*

Recurrence Relation

In a sequence $\{\phi_j(x)\}_0^\infty$ of orthogonal polynomials, each $\phi_n(x)$ $(n \geq 1)$ can be expressed as a linear combination of $\phi_0(x), \ldots, \phi_{n-1}(x)$ and $x\phi_{n-1}(x)$. However, due to the orthogonality property of each ϕ_n to all polynomials of lower degree (corollary 3.3.1), none of the $\phi_j(x)$ with $j < n-2$ are needed:

Theorem 3.3.3 *Every sequence $\{\phi_j(x)\}_0^\infty$ of orthogonal polynomials satisfies a three–term–recurrence of the form ($n \geq 2$)*

$$\phi_n(x) = \left(\frac{k_n}{k_{n-1}} x + B_n \right) \phi_{n-1}(x) - \frac{k_n k_{n-2}}{k_{n-1}^2} \phi_{n-2}(x), \, B_n \in \mathbb{R}. \tag{3.32}$$

Note that this form requires the polynomials to be normalized according to (3.29). If we set $\phi_{-1} \equiv 0$, it extends to $n = 1$.

Jacobi Matrix

By rewriting the recurrence relation (3.32) as

$$x\phi_{n-1}(x) = \frac{k_{n-1}}{k_n}\phi_n(x) + \frac{k_{n-2}}{k_{n-1}}\phi_{n-2}(x) - \beta_{n-1}\phi_{n-1}(x), \, \beta_{n-1} \in \mathbb{R}, \tag{3.33}$$

we notice a symmetry in the coefficients for $\phi_n(x)$ and $\phi_{n-2}(x)$. In matrix form for $n = 1, \ldots, N$, it reads

$$x\mathbf{p}_N(x) = \mathbf{J}_N\mathbf{p}_N(x) + \frac{k_{N-1}}{k_N}\phi_N(x)\mathbf{e}_N \tag{3.34}$$

where $\mathbf{p}_N(x) := \left(\phi_0(x), \ldots, \phi_{N-1}(x)\right)^T$, $\mathbf{e}_N := (0, \ldots, 0, 1)^T$ and the *Jacobi matrix*

$$\mathbf{J}_N := \begin{pmatrix} \beta_0 & \frac{k_0}{k_1} & 0 & 0 & \ldots & 0 \\ \frac{k_0}{k_1} & \beta_1 & \frac{k_1}{k_2} & 0 & \ldots & 0 \\ 0 & \frac{k_1}{k_2} & \beta_2 & \frac{k_2}{k_3} & \ldots & 0 \\ \vdots & \vdots & \vdots & \vdots & & 0 \\ \vdots & \vdots & \vdots & \vdots & & \vdots \\ 0 & 0 & 0 & 0 & \ldots & \beta_{N-1} \end{pmatrix}. \tag{3.35}$$

$\mathbf{J}_N$ is obviously symmetric. By the orthogonality of the ϕ_n,

$$(\mathbf{J}_N)_{ij} = (\phi_i, x\phi_j)_w, \tag{3.36}$$

$i, j = 0, \ldots, N - 1$, i.e. in physical terms $\mathbf{J}_N$ is the matrix representation of the position operator $\hat{X}$ (which in this setting acts on a function by multiplying it with its argument) in the basis $\left\{ \sqrt{w(x)}\phi_n(x) \right\}_{n=0}^{N-1}$ w.r.t. the $L^2[a, b]$ scalar product.

Christoffel–Darboux–Identity

The matrix form (3.34) of the recurrence relation enables us to establish an explicit expression for "scalar products" of polynomials with fixed arguments which will be crucial in the following:

Theorem 3.3.4 *(The Christoffel–Darboux–Identity.)*

$$\mathbf{p}_N(x) \cdot \mathbf{p}_N(y) = \sum_{n=0}^{N-1} \phi_n(x)\phi_n(y) = \frac{k_{N-1}}{k_N} \frac{\phi_{N-1}(y)\phi_N(x) - \phi_{N-1}(x)\phi_N(y)}{x - y}. \qquad (3.37)$$

In the limit of $y \to x$, we obtain for every zero x_ν ($\nu = 1, \ldots, N$) of $\phi_N(x)$

$$\|\mathbf{p}_N(x_\nu)\|^2 = \sum_{n=0}^{N-1} \phi_n^2(x_\nu) = \frac{k_{N-1}}{k_N}\phi_{N-1}(x_\nu)\phi_N'(x_\nu). \qquad (3.38)$$

Gauss Quadrature

It is well known that the zeros of orthogonal polynomials yield an efficient choice of quadrature points. In our presentation of Gauss quadrature, we focus especially on an explicit relation for the weights:

Theorem 3.3.5 *Let $w(x)$ be a weight function for the interval $[a,b]$ and $\{\phi_j(x)\}_0^\infty$ be the resulting sequence of orthogonal polynomials. For each $N \geq 1$ the zeros $a < x_1, \ldots, x_N < b$ of $\phi_N(x)$ and the weights*

$$H_\nu = \frac{1}{\|\mathbf{p}_N(x_\nu)\|^2} = \left(\sum_{n=0}^{N-1} \phi_n^2(x_\nu) \right)^{-1} \quad (\nu = 1, \ldots, n) \qquad (3.39)$$

are the unique numbers with the following property: The formula

$$\int_a^b f(x)w(x)\,\mathrm{d}x \approx \sum_{\nu=1}^{N} H_\nu f(x_\nu) =: Q_N(f) \qquad (3.40)$$

is exact for every polynomial f of degree $\leq 2N - 1$.

Differential Equation

A certain class of orthogonal polynomials has an additional important property: It solves a differential equation or, more specifically, these polynomials are eigenfunctions of a differential operator. The following theorem can be shown by simple partial integration:

Theorem 3.3.6 *(Rodrigues' Formula). If a sequence of infinitely differentiable ("generating") functions G_n satisfy*

$$\frac{\mathrm{d}^{n+1}}{\mathrm{d}x^{n+1}}\left(\frac{1}{w(x)}\frac{\mathrm{d}^n G_n(x)}{\mathrm{d}x^n}\right) = 0,$$

$$G_n(a) = G'_n(a) = \ldots = G_n^{(n-1)}(a) = 0,$$

$$G_n(b) = G'_n(b) = \ldots = G_n^{(n-1)}(b) = 0,$$

then

$$\phi_n(x) = \frac{1}{w(x)}\frac{\mathrm{d}^n G_n(x)}{\mathrm{d}x^n}$$

is the sequence of orthogonal polynomials associated with the weight function $w(x)$ on the interval $[a,b]$.

A little bit of algebra (see [51]) then reveals the differential equation; its meaning is best explained by the examples in the next subsection:

Theorem 3.3.7 *If $G_n(x)$ has the special form*

$$G_n(x) = w(x)[G(x)]^n$$

with G(x) being a quadratic polynomial,

$$G(x) = \alpha + \beta x + \gamma x^2,$$

*then the functions $y_n(x) = w(x)\phi_n(x)$ composed of a weight function $w(x)$ and the associated orthogonal polynomials $\phi_n(x)$ fulfill the following differential equation of second order (*Sturm–Liouville *type):*

$$G(x)y''_n(x) + \{2G'(x) - \phi_1(x)\}y'_n(x) -$$
$$\left\{\frac{n^2 - n - 2}{2}G''(x) + (n+1)\phi'_1(x)\right\}y_n(x) = 0.$$

Common Examples

It is often convenient to normalize orthogonal polynomials according to $(\phi_n, \phi_n)_w = \gamma_n \neq 1$. With this convention, the following table collects the properties of four widely used examples (Tschebyscheff (T), Legendre (P), Hermite (H) and Laguerre (L) poly-

nomials):

	T	P	H	L
Weight fct. $w(x)$	$(1-x^2)^{-1/2}$	1	e^{-x^2}	e^{-x}
Interval	$[-1,1]$	$[-1,1]$	$(-\infty,\infty)$	$[0,\infty)$
Conventional Normalization	$\gamma_0 = \pi,$ $\gamma_n = \frac{\pi}{2}\ (n \geq 1)$	$\dfrac{2}{2n+1}$	$2^n n! \sqrt{\pi}$	$(n!)^2$
First Polynomial	$T_0(x) = 1$	$P_0(x) = 1$	$H_0(x) = 1$	$L_0(x) = 1$
Second Polynomial	$T_1(x) = x$	$P_1(x) = x$	$H_1(x) = 2x$	$L_1(x) = 1-x$
Highest coeff. k_n	2^{n-1}	$\frac{1\cdot3\cdot5\cdots(2n-1)}{n!}$	2^n	$(-1)^n$

- Recurrence Relation:

$$T:\ T_{n+1}(x) = 2xT_n(x) - T_{n-1}(x)$$
$$P:\ (l+1)P_{l+1}(x) = (2l+1)xP_l(x) - lP_{l-1}(x)$$
$$H:\ H_{n+1}(x) = 2xH_n(x) - 2nH_{n-1}(x)$$
$$L:\ L_{n+1}(x) = (2n+1-x)L_n(x) - n^2 L_{n-1}(x)$$

- Differential Equation:

$$T:\ (1-x^2)T_n''(x) - xT_n'(x) + n^2 T_n(x) = 0$$
$$P:\ (1-x^2)P_l''(x) - 2xP_l'(x) + l(l+1)P_l(x) = 0$$
$$H:\ H_n''(x) - 2xH_n'(x) + 2nH_n(x) = 0$$
$$L:\ xL_n''(x) + (1-x)L_n'(x) + nL_n(x) = 0$$

3.3.2 Collocation Basis

Basic Properties

It is now easy to derive a key property of the Jacobi matrix (3.35):

Theorem 3.3.8 *The eigenvalues of the Jacobi matrix $\mathbf{J}_N$ are the zeros x_j ($j = 1,\ldots,N$) of the polynomial $\phi_N(x)$, the normalized eigenvector corresponding to the eigenvalue x_j is $\sqrt{H_j}\big(\phi_0(x_j),\ldots,\phi_{N-1}(x_j)\big)^T$. The $N \times N$ matrix $\mathbf{U}_N$,*

$$(\mathbf{U}_N)_{ij} := \sqrt{H_j}\phi_i(x_j) \quad (j = 1,\ldots,N;\ i = 0,\ldots,N-1), \tag{3.41}$$

is thus orthogonal and diagonalizes $\mathbf{J}_N$:

$$\big(\mathbf{U}_N^T \mathbf{J}_N \mathbf{U}_N\big)_{jk} = x_j \delta_{jk},\ j,k = 1,\ldots,N. \tag{3.42}$$

Proof: From (3.34), we obtain by substituting a zero x_j for x

$$x_j \mathbf{p}_N(x_j) = \mathbf{J}_N \mathbf{p}_N(x_j),$$

i e. $\left(\phi_0(x_j), \ldots, \phi_{N-1}(x_j)\right)^T$ is eigenvector of $\mathbf{J}_N$ corresponding to the eigenvalue x_j. The normalization of the rows and columns, resp., of $\mathbf{U}_N$ follows from the explicit formula (3.39) for the weights of the associated Gauss quadrature.   □

While the properties (3.41) and (3.42) are interesting in themselves and provide a numerically stable algorithm to compute roots and weights for a Gauss quadrature [55, 56], their importance extend to the option of performing orthogonal basis transformations via the matrix $\mathbf{U}_N$ [50]. In particular, we can apply this transformation to the orthogonal basis $\{\phi_n(x)\}_{n=0}^{N-1}$ of the space $\mathbb{P}_{N-1}$ of polynomials with degree $\leq N-1$:

Definition 3.3.2 *For every sequence $\{\phi_n(x)\}_{n=0}^{\infty}$ and every $N \geq 1$, the associated collocation basis is given by*

$$\psi_n^N := \left(\mathbf{U}_N^T \mathbf{p}_N\right)_n \ (n = 1, \ldots, N). \tag{3.43}$$

Note that the collocation basis depends on N in the sense that – contrary to the orthogonal polynomials – enlarging the basis will not simply add another basis function, but change all of them. The shape of these functions is clarified by

Theorem 3.3.9 *Every collocation basis $\left\{\psi_n^N\right\}_{n=0}^{N-1}$ associated to a weight function $w(x)$ on an interval $[a,b]$ has the following properties ($m, n \geq 0$, f any continuous function):*

$$(\psi_m^N, \psi_n^N)_w = \delta_{mn}, \tag{3.44}$$

$$\psi_n^N(x_m) = \frac{1}{\sqrt{H_n}} \delta_{mn}, \tag{3.45}$$

$$(\psi_n^N, f)_w \approx Q_N(\psi_m^N f) = \sqrt{H_n} f(x_n), \tag{3.46}$$

$$(\psi_m^N, f\psi_n^N)_w \approx Q_N(\psi_m^N f \psi_n^N) = f(x_n)\delta_{mn}. \tag{3.47}$$

Proof: The first statement immediately follows from the orthogonality of $\mathbf{U}_N$ and the orthonormality (3.29) of the orthogonal polynomials $\phi_n(x)$. For the second, note the explicit formula

$$\psi_n^N(x) = \sqrt{H_n} \sum_{i=0}^{N-1} \phi_i(x_n) \phi_i(x) \tag{3.48}$$

and the orthonormality of the columns of $\mathbf{U}_N$. The third and fourth are easy consequences then; the latter, for example, follows from

$$(\psi_m^N, f\psi_n^N)_w = \int_a^b \psi_m^N(x) f(x) \psi_n^N(x) w(x) \, dx$$

$$\approx\ Q_N(\psi_m^N f \psi_n^N)$$

$$=\ \sum_{\nu=1}^{N} H_\nu \psi_m^N(x_\nu) f(x_\nu) \psi_n^N(x_\nu)$$

$$=\ \sum_{\nu=1}^{N} H_\nu \delta_{m\nu} \frac{1}{\sqrt{H_m}} f(x_\nu) \delta_{n\nu} \frac{1}{\sqrt{H_n}}$$

$$=\ f(x_n) \delta_{mn}.$$

$\square$

Eq. (3.45) reveals the collocation basis to be suitably weighted Lagrange polynomials for the roots of the relevant Gauss quadrature,

$$\psi_n^N(x) = \frac{1}{\sqrt{H_n}} \prod_{\substack{i=1 \\ i \neq k}}^{N} \frac{x - x_i}{x_n - x_i}. \tag{3.49}$$

(In particular, each $\psi_n^N(x)$ is a polynomial of (exact) degree $N - 1$). In this sense, the collocation points x_i themselves can be regarded as the basis (instead of viewing them as simple technical quantities needed to evaluate integrals), and the mesh created by them is called a *Lagrange Mesh* [57].

Algorithm

Of special interest is the last property (3.47) as it yields a diagonal matrix representation for terms without derivatives in a partial differential equation. In the case of an operator $\hat{D}$ containing derivatives, the corresponding matrix elements in the collocation basis are

$$D_{ij}^C = (\psi_i^N, \hat{D} \psi_j^N)_w. \tag{3.50}$$

They can either be computed directly (based on the explicit formula (3.49) for the basis functions) or be evaluated in the basis of orthogonal polynomials (where they often have a simple shape, cf. (3.20)),

$$D_{ij}^P = (\phi_i, \hat{D} \phi_j)_w, \tag{3.51}$$

and then transformed via the matrix $\mathbf{U}_N$:

$$\mathbf{D}^C = \mathbf{U}_N \mathbf{D}^P \mathbf{U}_N^T. \tag{3.52}$$

The algorithm to approximately solve a linear differential equation (cf. (3.8)) or eigenvalue problem of a differential operator (cf. (3.9)) for u_N^P in the collocation method can be summarized as follows:

1. Choose an appropriate basis of orthogonal polynomials $\phi_n{}^2$ and the basis size N.

---

[2] A generally useful choice is provided by the Tschebyscheff polynomials, see Sec. 3.4.2.

2. Set up the Jacobi matrix $\mathbf{J}_N$ (3.35) with the coefficients k_n, β_n from the normalized recursion relation (3.33).

3. Diagonalize $\mathbf{J}_N$ as in (3.42) to obtain the transformation matrix $\mathbf{U}_N$ and collocation points x_i.

4. Set up the problem in the collocation basis:

   (a) Derivatives: Transform by (3.52) from the finite basis representation or compute directly using (3.49);

   (a) Functions as multiplicative operators: Evaluate at the collocation points according to (3.47), yielding a diagonal matrix representation;

   (a) Functions g as vectors on the right hand side: Evaluate pointwise in each entry as $\sqrt{H_i}g(x_i)$, see (3.46).

5. Solve the resulting matrix problem. The solution vector(s) $\mathbf{u}$ contain $\sqrt{H_i}u_N^P(x_i)$ as entries, see (3.45).

In our examples (3.8) and (3.9), the diagonal entries in the Jacobi matrix $\mathbf{J}_N$ are $\beta_i = 0$ (see Sec. 3.3.1). For the off-diagonal ones, note that the sequence needs to be normalized by $\phi_l = P_l/\sqrt{\gamma_l}$. The highest coefficient of the polynomial ϕ_l is then $k_l/\sqrt{\gamma_l}$ and the matrix entries turn out to be

$$
(\mathbf{J}_N)_{ij} = \begin{cases} \dfrac{i}{\sqrt{4i^2 - 1}} & \text{for } i = j - 1, \\ \dfrac{j}{\sqrt{4j^2 - 1}} & \text{for } j = i - 1, \\ 0 & \text{otherwise.} \end{cases} \tag{3.53}
$$

After transforming the derivative matrix $D_{lm}^P = l(l+1)\delta_{lm}$ in the collocation basis via (3.52) to yield $\mathbf{D}^C$, we finally get the matrix equation

$$
\mathbf{D}^C \mathbf{u} = \mathbf{g} \tag{3.54}
$$

with $g_i = \sqrt{H_i}g(x_i)$ or the matrix eigenvalue problem for

$$
\mathbf{D}^C + \mathbf{V} \tag{3.55}
$$

with $V_{ij} = V(x_i)\delta_{ij}$. (Note that both (3.25) and (3.26) imply a different normalization).

Convergence Properties

- Convergence of the Expansion

For a sequence of orthogonal polynomials $\{\phi_n(x)\}_0^\infty$ and a function f, we can try to expand the function in terms of the polynomials, i.e.

$$f(x) \sim \sum_{n=0}^{\infty} c_n \phi_n(x) \tag{3.56}$$

with

$$c_n = (\phi, f)_w = \int_a^b \phi_n(x) f(x) w(x) \, dx. \tag{3.57}$$

While the general answer to the problem of what $\sim$ means in (3.56) opens up the field of approximation theory which shall not be considered here, an interesting statement can be given for the case that a and b are finite [61] (similar to the Dini–Lipschitz test for the pointwise convergence of Fourier–series):

Theorem 3.3.10 *Let f be continuous on the finite interval $[a,b]$ and satisfy a Lipschitz– condition at x_0, i.e. $|f(x) - f(x_0)| \leq K|x - x_0|$ for some $K > 0$. Suppose in addition that $\phi_n(x_0)$ remains bounded for $n \to \infty$. Then (3.56) holds pointwise at x_0.*

Proof: The partial sum $S_N(x)$ is

$$
\begin{aligned}
S_N(x_0) &= \sum_{n=0}^{N} (\phi, f)_w \phi_n(x_0) \\
&= \sum_{n=0}^{N} \int_a^b \phi_n(y) f(y) w(y) \, dy \, \phi_n(x_0) \\
&= \int_a^b f(y) w(y) \left(\sum_{n=0}^{N} \phi_n(x_0) \phi_n(y) \right) dy.
\end{aligned}
$$

For the term in brackets, we can insert the Christoffel–Darboux–Identity (3.37). By multiplying this identity with $w(y)$ and integrating over y, we get by orthogonality

$$1 = \frac{k_N}{k_{N+1}} \int_a^b \frac{\phi_N(y) \phi_{N+1}(x_0) - \phi_N(x_0) \phi_{N+1}(y)}{x_0 - y} w(y) \, dy.$$

After multiplying with $f(x_0)$ and subtracting from $S_N(x_0)$, we obtain for the difference

$$
S_N(x_0) - f(x_0) =
$$
$$
\frac{k_N}{k_{N+1}} \int_a^b [f(y) - f(x_0)] \frac{\phi_N(y) \phi_{N+1}(x_0) - \phi_N(x_0) \phi_{N+1}(y)}{x_0 - y} w(y) \, dy.
$$

The fraction k_N/k_{N+1} can be estimated to remain bounded: It is an entry of the Jacobi matrix the eigenvalues of which are the zeros of ϕ_N and thus lie in the finite interval $[a,b]$; as the diagonal entries β_n are positive, k_N/k_{N+1} is bounded by the largest zero $x_{\max}$ as can be seen with a suitably chosen test vector $\mathbf{x}$ in

$$x_{\max} \geq \frac{(\mathbf{x}, \mathbf{J}_N \mathbf{x})}{(\mathbf{x}, \mathbf{x})}.$$

Therefore it remains to show that the integral tends to zero. The expression can be rewritten as

$$S_N(x_0) - f(x_0) = \frac{k_N}{k_{N+1}} \left((h, \phi_{N+1})_w \phi_N(x_0) - (h, \phi_N)_w \phi_{N+1}(x_0) \right)$$

where $h(y) = (f(y) - f(x_0))/(y - x_0)$. By the Lipschitz–condition for f, h is bounded and continuous (except, possibly, at x_0); the numbers $(h, \phi_N)_w$ as the generalized Fourier coefficients of h thus tend to zero for $N \to \infty$. As $\phi_N(x_0)$ remains bounded, the total right hand side vanishes for $N \to \infty$.   □

- Error Classification

The principle error in every spectral method will be caused by using only a finite expansion u_N^P like (3.11) to generate the approximate solution. As pointed out in the introduction, Sec. 3.2.3, the expansion coefficients $\hat{u}_k^N$ in the numerical solution will depend on N itself. In other words, if u is a solution for a differential equation like $\hat{D}u = g$, then $\hat{P}_N u$, the solution projected onto the first N orthogonal polynomials (with $\hat{P}_N$ as in (3.12)), will in general not be a solution of the reduced matrix equation $\hat{P}_N \hat{D} \hat{P}_N u = \hat{P}_N g$. However, the difference $u - \hat{P}_N u$ between the exact and the projected solution can serve to analyze the error by looking at its norm,

$$\|u - \hat{P}_N u\|_w, \tag{3.58}$$

where $\| \cdot \|_w$ is derived from the scalar product $(,)_w$.

A second type of error arises from the approximate evaluation of the matrix elements by (Gauss) quadrature. Note that this error is the same for the collocation method and the finite basis representation which are related by an orthogonal transformation. To shed more light on this error, we exploit the special integration property (3.47) of the collocation basis to define an adapted discrete scalar product [47]:

Definition 3.3.3 *For any two continuous functions f, g on $[a,b]$, we define*

$$(f,g)_N := Q_N(fg) = \sum_{v=1}^{N} H_v f(x_v) g(x_v). \tag{3.59}$$

For two polynomials f, g the product of which has a degree of at most $2N-1$, we get

$$(f,g)_N = (f,g)_w \tag{3.60}$$

by the Gaussian integration property (3.40). Thus, $(,)_N$ is a scalar product on the space $\mathbb{P}_{N-1}$ of polynomials of degree $\leq N-1$ and we have orthonormality of the finite polynomial basis ϕ_n for $n=0,\ldots,N-1$ and the collocation basis ψ_n^N for $n=1,\ldots,N$:

$$(\phi_n, \phi_m)_N = (\psi_n^N, \psi_m^N)_N = \delta_{mn}. \tag{3.61}$$

The collocation aims at finding the values $u(x_i)$ of the solution u at the collocation points. If we again neglect the fact that the numerically obtained values will differ from the exact ones for finite N, the collocation solution can essentially be described by an interpolation polynomial $\hat{I}_N u$ of degree $N-1$ which agrees with the exact solution in all x_i:

$$(\hat{I}_N u)(x_i) = u(x_i),\ 1 \leq i \leq N,\ \hat{I}_N u \in \mathbb{P}_{N-1}. \tag{3.62}$$

(The additional factor $\sqrt{H_i}$ contained in the solution vectors is not relevant for this analysis). In terms of the finite basis ϕ_n, we can write

$$\hat{I}_N u = \sum_{i=0}^{N-1} \tilde{u}_i \phi_i$$

with the *discrete polynomial coefficients* $\tilde{u}_i$; their difference to the expansion coefficients describes the quadrature error. For every continuous f, we have

$$(\hat{I}_N u, f)_N = (u, f)_N, \tag{3.63}$$

i.e. $\hat{I}_N u$ is the projection of u onto $\mathbb{P}_{N-1}$ w.r.t. the discrete scalar product $(,)_N$, whereas $\hat{P}_N u$ projects w.r.t. $(,)_w$. As a consequence, we can compute the discrete polynomial coefficients from

$$\tilde{u}_i = (u, \phi_i)_N,$$

and by (3.61) we can express them as

$$\begin{aligned}
\tilde{u}_i &= \left(\sum_{k=0}^{\infty} u_k \phi_k, \phi_i \right)_N \\
&= \hat{u}_i + \sum_{k=N}^{\infty} (\phi_k, \phi_i)_N u_k.
\end{aligned}$$

Multiplying with ϕ_i and summing from $i=0$ to $N-1$, this reads

$$\hat{I}_N u = \hat{P}_N u + \hat{R}_N u \tag{3.64}$$

with the *quadrature error* or *aliasing error*

$$\hat{R}_N u := \sum_{i=0}^{N-1} \left(\sum_{k=N}^{\infty} (\phi_k, \phi_i)_N u_k \right) \phi_i. \tag{3.65}$$

Now $\hat{R}_N u$ is orthogonal to $u - \hat{P}_N u$ w.r.t. $(,)_w$ as the former is a linear combination of polynomials ϕ_i up to index $N-1$ and the latter starts at index N. Therefore

$$\|u - \hat{I}_N u\|_w^2 = \|u - \hat{P}_N u\|_w^2 + \|\hat{R}_N u\|_w^2. \tag{3.66}$$

By (3.65), the additional error $\|\hat{R}_N u\|_w^2$ is caused by quadrature instead of exact integration and will crucially depend on the decay of the expansion coefficients u_k which, in case of spectral accuracy, can be expected to be faster than polynomial.

- Spectral Accuracy Revisited

A qualitative argument in addition to the one given in Sec. 3.2.2 might support the expected fast convergence of the method [63]. In the analysis of the convergence properties of finite differences or finite elements, the error is usually of the form $O(h^\alpha)$, where h refers to the spacing of the points and $\alpha > 0$ depends on the method chosen, i.e. the polynomial degree. For collocation methods, increasing the size N of the basis will both decrease the grid spacing $h \approx 1/N$ and increase the polynomial degree $N \approx \alpha$, so that the resulting error is

$$\approx O[(1/N)^N],$$

i.e. it decreases faster than any finite power of N.

3.4   Generalizations

3.4.1   Several Dimensions

Passing from one to d dimensions (and thus from ordinary to partial differential equations), the sparsity (3.47) of matrix elements of functions is the key element for efficiency of the collocation method. More precisely, let $\hat{T}$ be a linear partial differential operator in d coordinates $q_1, \ldots, q_d$ of the form

$$\hat{T} = \sum_{i=1}^{g} \prod_{j=1}^{d} \hat{d}^{(i,j)}(q_j), \tag{3.67}$$

where $\hat{d}^{(i,j)}(q_j)$ is supposed to act on coordinate q_j only, i.e. $\hat{T}$ is a sum of products of such operators. This involves mixed partial derivatives of arbitrary order, multiplied with functions in one of the coordinate, for example terms like

$$\frac{\partial^2}{\partial x^2}, \quad \frac{\partial^3}{\partial x \partial y^2}, \quad f(x)g(y)\frac{\partial^2}{\partial x \partial y}.$$

In addition, we allow operators $\hat{V}$ which consist of functions of all variables as multiplicative operators (with possibly a derivative term in one of the variables), for example

$$V(x,y,z), \quad f(x,y)\frac{\partial}{\partial x}.$$

Let the total operator be $\hat{D} = \hat{T} + \hat{V}$. (An example for an operator of this type is the Hamiltonian in quantum mechanics. For several particles, the dimension d will not be restricted to three). In order to solve a differential equation or the eigenvalue problem for $\hat{D}$ by the collocation method, we choose N_i orthogonal polynomials for coordinate q_i (possibly different) and form the product basis

$$\psi_{(n_1,\ldots,n_d)}(q_1,\ldots,q_d) = \prod_{i=1}^{d} \psi_{n_i}^{N_i}(x), \ 1 \leq n_i \leq N_i. \tag{3.68}$$

This basis has a size of $N = N_1 \cdots N_d$. For computationally demanding problems, it is not feasible to solve the resulting matrix equation or matrix eigenvalue problem by black box algorithms like the Gauss algorithm or Householder tridiagonalization which scale like N^3 and are by far too costly. Instead, iterative procedures (Krylov–space algorithms like the Lanczos tridiagonalization or others) come into play which do not need the matrix representation of $\hat{D}$ itself, but evaluate matrix–vector products $\hat{D}v$ for arbitrary vectors v. For simplicity of the presentation, let us assume that $N_1 = \ldots = N_d = n$. A full matrix would require $N^2 = n^{2d}$ operations (flops) for a matrix vector product whereas the product collocation basis scales much better [62]:

Theorem 3.4.1 *In a product collocation basis like (3.68), the number of flops F for a matrix–vector product $\hat{D}v$ will scale like*

$$F(\hat{D}v) \sim dn^{d+1} \tag{3.69}$$

with the number of dimensions d and the one–dimensional basis size n.

Proof: Due to the product structure of the basis, a single derivative term like $\partial/\partial q_i$ has a matrix representation like

$$\left(\psi_{(n_1,\ldots,n_d)}, \frac{\partial}{\partial q_i}\psi_{(n'_1,\ldots,n'_d)}\right) = \left(\psi_{n_i}, \frac{\partial}{\partial q_i}\psi_{n'_i}\right)\prod_{\substack{j=1 \\ j\neq i}}^{d}\delta_{n_j n'_j},$$

i.e. it has $n^2 \cdot n^{d-1} = n^{d+1}$ nonvanishing matrix elements. Mixed derivatives have a more dense matrix representation; however, this representation consists of products of matrices with n^{d+1} nonzero elements and the matrix vector product can be evaluated sequentially. The number of derivatives terms will be roughly d in d dimensions so that the numerical effort for the $\hat{T}$–part of $\hat{D}$ scales like dn^{d+1}. While these arguments simply rely on the product structure of the basis, for the $\hat{V}$–part of the operator we exploit the property (3.47) of the collocation basis: Matrix elements with functions $V(q_1,\ldots,q_d)$ as operators turn out to be

$$\left(\psi_{(n_1,\ldots,n_d)}, V\psi_{(n'_1,\ldots,n'_d)}\right) = V(q_{n_1,1},\ldots,q_{n_d,d})\prod_{j=1}^{d}\delta_{n_j n'_j} \tag{3.70}$$

where $q_{n_i,i}$ is the n_i–th collocation point in coordinate q_i. In other words, the matrix representation of such a term is diagonal and the contribution to the matrix–vector product scales like n^d which is negligible. (If in addition a derivative appears, we arrive at the same scaling as for terms in $\hat{T}$).   □

As an example, consider $d = 3$ and $n = 50$ basis functions in each coordinate for the operator

$$-\frac{\partial^2}{\partial x^2} - \frac{\partial^2}{\partial y^2} - \frac{\partial^2}{\partial z^2} + V(x,y,z).$$

A full matrix representation has $\approx 10^{10}$ elements requiring ≈ 10 seconds of computing time for one matrix–vector product on a processor with a gigaflop performance, while in a collocation product basis only $\approx 10^7$ flops, i.e. $\approx 10^{-2}$ seconds of computing time are needed. In addition, it is of high practical importance that the representation of the individual derivatives consists of smaller submatrices. If the vectors are blocked accordingly, matrix–vector products can be computed as several matrix–matrix products of smaller size, allowing the use of high–performance BLAS 3–routines.

3.4.2 Arbitrary Orthogonal Functions

An Adaptive Algorithm

While the properties of collocation methods can be best described in the framework of orthogonal polynomials, it is of a high practical importance to extend these concepts to orthogonal functions in general.

First, the algorithm presented in Sec. 3.3.2 allows for a straightforward generalization to a sequence $\{f_n(x)\}_0^\infty$ of orthogonal functions. The key ingredient is the Jacobi matrix $\mathbf{J}_N$ which provides the collocation points as eigenvalues and the transformation to the collocation basis via its eigenvectors. The general sequence $\{f_n(x)\}_0^\infty$ will not satisfy a three–term recursion by which we introduced $\mathbf{J}_N$; however, Eq. (3.36) provides an alternative characterization for $\mathbf{J}_N$ as the matrix elements of the coordinate as a multiplicative operator. Thus, if we define

$$(\mathbf{J}_N^f)_{ij} := (f_i, x f_j),\ 0 \le i, j \le N - 1, \tag{3.71}$$

a collocation method can be set up for an arbitrary sequence of orthogonal functions [49]. As it suffices to compute the matrix elements in (3.71), the sequence may even consist of only numerically known functions, for example one–dimensional eigenfunctions of suitable "reference differential operators" to a higher dimensional problem. This opens up the possibility for an efficient adaptive algorithm [52].

Of course, the question of the validity of using (3.71) arises. It can be shown that the quadrature obtained in this way is a Gauss quadrature w.r.t. a suitably chosen set of orthogonal polynomials [59]. In this sense, (3.71) generalizes the concept of an optimal quadrature to arbitrary orthogonal functions. However, regarding the collocation method, we will demonstrate that a general set of orthogonal functions will not have the same properties as orthogonal polynomials do.

General Conditions

A decisive property of the collocation basis is Eq. (3.45) which states that the collocation basis function behave essentially like finite dimensional delta functions within the space of the first N orthogonal polynomials. The projection operator $\hat{P}_N$ onto N orthogonal functions $f_0, \ldots, f_{N-1}$, Eq. (3.12), has the kernel

$$p_N(x,y) = \sum_{n=0}^{N-1} f_n(x) f_n(y) \tag{3.72}$$

which allows to compute matrix elements of $\hat{P}_N$ with functions g and h by

$$(g, \hat{P}_N h) = \int_a^b g(x) p_N(x,y) h(y) \, dx \, dy \tag{3.73}$$

(formally $p_N(x,y) = (\delta_x, \hat{P}_N \delta_y)$). The projection of a δ–function δ_{x_i} centered around x_i has then the form

$$(\hat{P}_N \delta_{x_i})(x) = \sum_{n=0}^{N-1} f_n(x) f_n(x_i) \tag{3.74}$$

(apart from normalization which is different in Eq. (3.48)). In order to retain orthogonality between two such functions centered around x_i and x_j for $i \neq j$, we need

$$\left(\sum_{n=0}^{N-1} f_n(x) f_n(x_i), \sum_{n=0}^{N-1} f_n(x) f_n(x_j) \right) = \sum_{n=0}^{N-1} f_n(x_i) f_n(x_j)$$
$$= 0 \tag{3.75}$$

where in the first step we assumed orthonormality of the f_n. These equations give $1/2N(N-1)$ conditions for the N points $x_1, \ldots, x_N$ which in general cannot be satisfied [57]. For orthogonal polynomials, however, the kernel p_N has a simple shape given by the Christoffel–Darboux Identity (3.37), and the conditions (3.75) are fulfilled by using the zeros of ϕ_N. Collocation methods can nevertheless be set up (less efficiently) with non–orthogonal basis sets [68], and generalizations of this formula might serve to characterize the class of orthogonal functions with the same properties as orthogonal polynomials and help to find a multidimensional extension [58].

A Generic Basis

In the search of a suitable basis for a specific problem, the following Fourier–type functions derived from Tschebyscheff polynomials will yield an often useful possibility. First, note that the Tschebyscheff polynomials T_k can also be expressed as

$$T_k(x) = \cos\left(k \cos^{-1}(x)\right) \tag{3.76}$$

on the interval $[-1, 1]$. A collocation basis derived from these polynomials will certainly satisfy the orthogonality condition (3.75), and so do the functions $T_k(\cos\varphi) = \cos(k\varphi)$ on the interval $[0, \pi]$ [57] w.r.t. a modified weight function which turns out to be constant in our case. To get a basis that vanishes at the endpoints of an interval $[a, b]$ (which is a suitable boundary condition for functions that vanish at infinity), we switch to

$$f_k(x) = \sqrt{\frac{2}{b-a}} \sin\left(\frac{k\pi(x-a)}{b-a}\right) \tag{3.77}$$

with $k = 1, \ldots, N-1$ and the grid points $x_i = a + i\Delta x$, $i = 1, \ldots, N-1$ having a distance $\Delta x = (b-a)/N$ [53]. These function are orthonormal w.r.t. a unit weight function. By Sec. 3.4.2, the collocation basis is

$$\begin{aligned}
\psi_i^{N-1}(x) &= \sum_{n=0}^{N-1} \frac{2}{b-a} \sin\left(\frac{k\pi(x-a)}{b-a}\right) \sin\left(\frac{k\pi(x_i-a)}{b-a}\right) \\
&= \frac{1}{2(b-a)} \frac{\sin\left(\frac{\pi(x_i-a)}{b-a}\right) \sin\left(\frac{\pi(x-x_i)}{\Delta x}\right)}{\cos\left(\frac{\pi(x_i-a)}{b-a}\right) - \cos\left(\frac{\pi(x-a)}{b-a}\right)}
\end{aligned} \tag{3.78}$$

after a bit of algebra. These functions still satisfy the orthogonality condition (3.75) and a nice result is obtained in the limit of infinite intervals $b - a \to \infty$ and infinite order $N \to \infty$, but finite spacing $\Delta x = (b-a)/N$:

$$\begin{aligned}
\psi_i^{N-1}(x) &\rightarrow \frac{\sin\left(\frac{\pi(x-x_i)}{\Delta x}\right)}{\pi(x - x_i)} \\
&= \frac{1}{\Delta x} \mathrm{sinc}\left(\frac{\pi(x - x_i)}{\Delta x}\right)
\end{aligned} \tag{3.79}$$

with $x_i = i\Delta x$, $i = 0, \pm 1, \pm 2, \ldots$ and $\mathrm{sinc}(x) := \sin(x)/x$. This "sinc"–basis can be seen as an analytic version of "hat"–functions used in finite elements. Of course, the infinitely many collocation points have to be reduced to a finite set, corresponding to setting the solution to zero everywhere else. Matrix elements of derivatives can be evaluated analytically in this basis [53] (with the proper normalization of $1/\sqrt{\Delta x}$ instead of $1/\Delta x$ [54]):

$$\left(\psi_k^N, \frac{\partial}{\partial x} \psi_l^N\right) = \frac{1}{(\Delta x)}(-1)^{k-l} \left\{ \begin{array}{ll} 0 & k = l \\ \frac{1}{(k-l)} & k \neq l \end{array} \right\}, \tag{3.80}$$

$$\left(\psi_k^N, \frac{\partial^2}{\partial x^2} \psi_l^N\right) = \frac{-1}{(\Delta x)^2}(-1)^{k-l} \left\{ \begin{array}{ll} \pi^2/3 & k = l \\ \frac{2}{(k-l)^2} & k \neq l \end{array} \right\}. \tag{3.81}$$
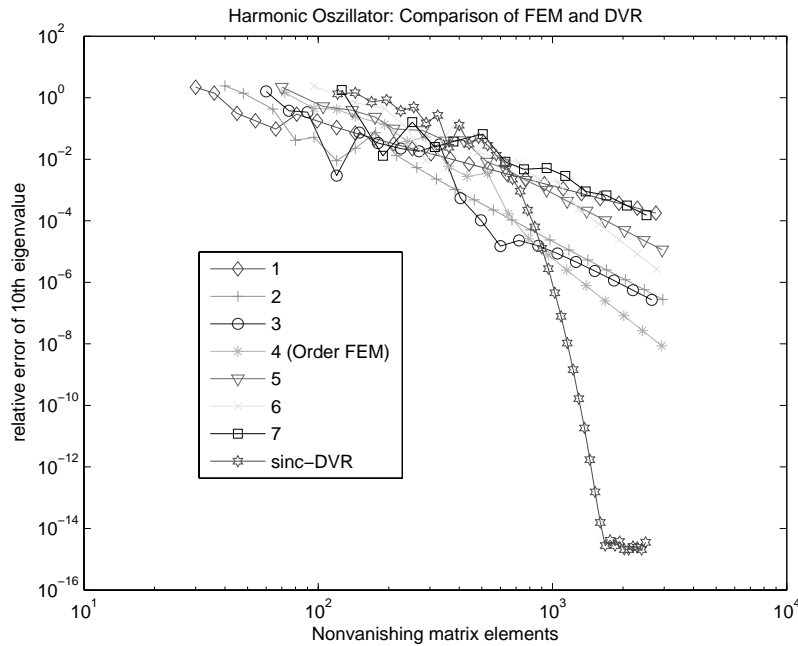
Figure 3.1: Comparison of the convergence behavior of finite elements and a sinc–DVR.

3.4.3   Comparison to Finite Elements

Figure 3.1 shows a comparison between the sinc–collocation from Sec. 3.4.2 and Lagrange elements of different order for the eigenvalue problem of the operator

$$\hat{D} = -\frac{1}{2}\frac{\partial^2}{\partial x^2} + \frac{1}{2}x^2. \tag{3.82}$$

Its eigenfunctions are composed of the Hermite Polynomials (see Sec. 3.3.1 and note that the polynomials have to be multiplied with the square root of the weight function), its eigenvalues are $E_n = 1/2 + n$. The plot shows the relative error of E_9 as a function of the numerical effort (the number of nonvanishing matrix elements).

For small basis sizes and large errors, the collocation method does not converge faster; however at about 500 matrix elements corresponding to ca. 22 basis functions, the basis is large enough to capture the main features of the eigenfunction (which is essentially a polynomial of degree 9) and exponential convergence sets in up to numerical accuracy. The FEM results of order 3 and above probably suffer from roundup errors which can be removed; however, the principal (polynomial type) behavior of convergence will not change. In addition, if the same number of nonvanishing matrix elements offers a similar error for two different methods, the one with the smaller basis is preferable as matrix elements can be easier accessed and the vectors used to build the solution are smaller. This is another argument in favor of the collocation method.

In the literature, an absolute accuracy of $\approx 10^{-9}$ has been reported for E_9 when using 20 [65] and 28 [64] Lagrange elements of order eight, corresponding to about $20 \cdot 8 \cdot 10 = 1600$ and $28 \cdot 8 \cdot 10 = 2240$ nonvanishing matrix elements; for the latter, a nonuniform grid was used. In the first case, also mean–square and maximum–norm errors of the eigenfunctions were computed to be of the order 10^{-6}. For a product ansatz, the FEM error is restricted to these figures while in a collocation basis the (true) eigenfunctions up to an arbitrary high precision can be used. Taking into account that quadrature errors will induce spurious states at about $3/4$ of the maximum eigenvalue [66], a collocation method can accurately represent the eigenfunction to the above problem with ≈ 14 basis functions having 196 nonvanishing matrix elements only.

Of course, the global ansatz functions of spectral methods induce certain limitations. First, one is restricted to essentially rectangular geometries ("essentially" intends that in the collocation method, grid points in regions where the solution (nearly) vanishes can be omitted [53]; see Sec. 3.5). Second, boundary conditions are determined by the orthogonal functions used to build the collocation basis so that varying the boundary values requires further effort. Especially, Gauss quadrature points never lie on the boundary by theorem 3.3.2; to enforce a (Dirichlet) boundary condition not automatically satisfied by the basis, Gauss–Lobatto or Gauss–Radau quadrature schemes need to be used [47].

3.5   PODVR of the Schroedinger Equation

In view of the general background outlined in sections 3.2, 3.3 and 3.4, the potential optimized discrete variable representation (PODVR) of the Hamiltonian presented as a numerical recipe in [52] can be associated with its general background. Specifically, consider a Hamiltonian of the form

$$\hat{H} = \underbrace{\sum_{i=1}^{n} \hat{D}_i}_{\hat{T}} + V(x^1, \ldots, x^n) \tag{3.83}$$

with $\hat{T}$ representing the kinetic energy operator in n degrees of freedom. Each $\hat{D}_i$ is a derivative operator depending on one coordinate x_i only and $V(x^1, \ldots, x^n)$ a function (acting as a multiplicative operator) representing the potential energy of the configuration specified by $x^1, \ldots, x^n$. Finally, we would like to compute the lower spectrum of this operator (a fixed number of eigenfunctions or all eigenfunctions below a certain energy, resp.). For that purpose, we use a product collocation basis of the form of Eq. (3.68); the individual collocation basis functions $\psi_{n_i}^{N_i}$ are not derived from orthogonal polynomials, but from a more general set of orthogonal functions as described in Sec. 3.4.2. These, in turn, are chosen to be the N_i lowest eigenfunctions of a suitable one–dimensional symmetric operator for each degree of freedom. While the choice of the kinetic energy part for these "reference Hamiltonians" is obvious, the potential

energy part needs some consideration. A possibility that often works is to minimize the potential energy V along all other coordinates,

$$V_{\text{ref}}^i(x^i) := \min_{x^j, j \neq i} V(x^1, \ldots, x^n). \tag{3.84}$$

For each degree of freedom, we then diagonalize the reference Hamiltonian

$$\hat{H}_{\text{ref}}^i(x^i) := \hat{D}_i + V_{\text{ref}}^i(x^i), \tag{3.85}$$

yielding N_i (orthogonal) eigenfunctions f_i which, in a next step, are used in Eq. (3.71). The f_i can in turn be conveniently computed by using the generic sinc–DVR, Eq. (3.80) and (3.81), for radial degrees of freedom and Legendre polynomials (see Eq. (3.53)) for angular variables. The matrix elements of the f_i with the position operator needed in Eq. (3.71) are then consistently evaluated in a quadrature approximation by representing the position operator in the collocation basis as diagonal and transforming this representation to the basis of the f_i functions.

In a last step, all product collocation basis functions are discarded for which the corresponding collocation points $(x_{i_1}^1, \ldots, x_{i_n}^n)$ satisfy

$$V(x_{i_1}^1, \ldots, x_{i_n}^n) > V_{\text{cut}} \tag{3.86}$$

with a suitably chosen energy V_{cut} which can be considered infinite for the purpose of the calculation. This amounts to setting the wavefunction to zero at these points. Blocking of the vectors to use BLAS 3–routines (cf. Sec. 3.4.1) requires these points to be filled with zeros; nevertheless, storage requirements are less and the condition of the matrix will be improved.

3.6 Diagonalization Techniques

The choice of a proper method to diagonalize the matrix representation of the Hamiltonian is another key issue for the efficiency of the entire algorithm. The appropriate class of diagonalization techniques consists in matrix–vector algorithms owing to the sparsity of the (large) matrices. A standard program package for that purpose is ARPACK [69].

In the first subsection, we discuss the error measure to be used in approximate matrix–vector algorithms. A measure different from the one used in the ARPACK package is proposed. The second subsection contains a summary of the algorithm used in the present calculations (Lanczos with Partial Reorthogonalization). The third briefly summarizes another strategy (the Jacobi–Davidson method) and investigates its criterion to determine the number of iteration steps. The fourth finally contains a proposal to better exploit the search subspaces build in the Jacobi–Davidson method in order to obtain an efficient method for many eigenvalues.

3.6.1 Error Measure

For any approximation $\tilde{\mathbf{x}}$ of an eigenvector $\mathbf{x}$ of a (symmetric) matrix $\mathbf{H}$, the residual $\mathbf{r}$ is given by

$$\mathbf{r} = \mathbf{H}\tilde{\mathbf{x}} - \theta\tilde{\mathbf{x}}, \tag{3.87}$$

where $\theta = (\tilde{\mathbf{x}}, \mathbf{H}\tilde{\mathbf{x}})$ is a (Ritz) approximation for the true eigenvalue λ, $\mathbf{H}\mathbf{x} = \lambda\mathbf{x}$ (all eigenvectors and approximate eigenvectors assumed normalized). If a specific tolerance ε is allowed for the approximation of $\tilde{\mathbf{x}}$, the first idea is to compare ε to the norm $||\mathbf{r}||$ of the residual. This measure, however, would not be scale invariant. ARPACK essentially uses the criterion

$$\frac{1}{\theta}||\mathbf{r}|| \leq \varepsilon \tag{3.88}$$

which solves the problem of scale invariance. However, this measure still does not account properly for clustered eigenvalues. We thus propose

$$r_\lambda := \frac{1}{\delta}||\mathbf{r}|| \leq \varepsilon \tag{3.89}$$

where $\delta := \min_j |\theta - \theta_j|$ and the θ_j summarize all other Ritz values. This criterion, being both shift–and scale invariant, gives reliable error bounds on scalar products of approximate eigenvectors. To be more specific, we have the following error bound for the eigenvector approximation $\tilde{\mathbf{x}}$ [70, 71, 72]:

$$\sin(\mathbf{x}, \tilde{\mathbf{x}}) \leq \frac{||\mathbf{r}||}{\delta_e} \tag{3.90}$$

with $\delta_e := \min_j |\theta - \lambda_j|$ and λ_j being the exact eigenvalues. For the overlap matrix elements of two eigenvectors $\mathbf{x}_1, \mathbf{x}_2$ in two adjacent sectors, this gives an error estimate

$$|(\tilde{\mathbf{x}}_1, \tilde{\mathbf{x}}_2) - (\mathbf{x}_1, \mathbf{x}_2)| \lesssim 2r_\lambda \tag{3.91}$$

where the estimate would hold exactly if, on the one hand, $\mathbf{x}_1$ and $\mathbf{x}_2$ referred to the same matrix (the difference of adjacent surface Hamiltonians is small, however). On the other hand, we would have to use δ_e instead of δ in the definition of r_λ; again, in practice this will not cause problems: The Ritz values are close to the true eigenvalues as they usually are better converged than the approximations for the eigenvectors.

Along the same line of argument, the non–orthogonality of two approximate eigenvectors will also be bound by this quantity such that one can be sure of a certain level of orthogonality without (re–)orthogonalization of all eigenvectors.

3.6.2 Lanczos with Partial Reorthogonalization

To obtain the first N_{ch} eigenvalues and eigenstates used in the scattering calculations, we can exploit the sparsity of the resulting PODVR Hamiltonian matrix and implement

a slight variation of the Lanczos algorithm [73] with partial reorthogonalization [74]. The latter procedure in its original form has, for example, been already used by Yu and Nyman [75] in quantum-chemical calculations.

By the well–known Lanczos recursion relation,

$$\mathbf{H}\mathbf{q}_k = \beta_{k-1}\mathbf{q}_{k-1} + \alpha_k\mathbf{q}_k + \beta_k\mathbf{q}_{k+1}, \tag{3.92}$$

with $\beta_0\mathbf{q}_0 = 0$ and an initial vector $\mathbf{q}_1$ we generate a tridiagonal matrix representation $\mathbf{T}_n = \mathbf{Q}_n^T\mathbf{H}\mathbf{Q}_n$, $\mathbf{Q}_n = (\mathbf{q}_1,\ldots,\mathbf{q}_n)$ with orthonormal columns $\mathbf{q}_k$,

$$\mathbf{T}_n = \begin{pmatrix} \alpha_1 & \beta_2 & & \ldots & 0 \\ \beta_2 & \alpha_2 & \ddots & & \vdots \\ & \ddots & \ddots & \ddots & \\ \vdots & & \ddots & \ddots & \beta_n \\ 0 & \ldots & & \beta_n & \alpha_n \end{pmatrix}. \tag{3.93}$$

$\mathbf{T}_n$ is the orthogonal projection of the PODVR Hamiltonian matrix $\mathbf{H}$ onto the Krylov subspace $\mathcal{K}(\mathbf{q}_1,\mathbf{H},n) = \mathrm{span}\{\mathbf{q}_1,\mathbf{H}\mathbf{q}_1,\ldots,\mathbf{H}^n\mathbf{q}_1\}$ with basis $\mathbf{Q}_n$. Evaluation of the recursion relation, Eq. (3.92), uses matrix–vector multiplications only, thus exploiting the sparsity of $\mathbf{H}$. The eigenvalues θ_k and eigenvectors $\mathbf{s}_k$ of $\mathbf{T}_n$ can be determined at low computational cost. If n equals the number of rows resp. columns of $\mathbf{H}$, the eigenvalues are the same as those of $\mathbf{H}$ and the eigenvectors can be easily transformed to yield $\mathbf{y}_k = \mathbf{Q}_n\mathbf{s}_k$. For smaller n, we have an error bound

$$\mathrm{res}(k) = ||\mathbf{H}\mathbf{y}_k - \theta_k\mathbf{y}_k||_2 = |\beta_n||s_{nk}| \tag{3.94}$$

where s_{nk} is the last component of the k-th eigenvector of $\mathbf{T}_n$.

The common problem of numerical non–orthogonality of the $\mathbf{q}_k$ can be handled by full reorthogonalization of each new $\mathbf{q}_n$ against all previous ones. However, this computationally demanding procedure is unnecessary as non–orthogonality usually arises from the convergence of an eigenvector (cf. Eq. (3.94) and (3.92)) which does not occur in every Lanczos step. If $n+1$ steps are performed, partial reorthogonalization [74] estimates the orthogonality components in the $(n+1)$–th step, $\omega_{n+1,k} = \mathbf{q}_{n+1}^T\mathbf{q}_k$, by the recurrence relation

$$\omega_{kk} = 1, \; k = 1,\ldots,n,$$

$$\omega_{k,k-1} = \Psi_k, \; k = 2,\ldots,n, \tag{3.95}$$

$$\omega_{n+1,k} = \frac{1}{\beta_{n+1}}\Big(\beta_{k+1}\omega_{n,k+1} + (\alpha_k - \alpha_n)\omega_{nk} + \beta_k\omega_{n,k-1} - \beta_n\omega_{n-1,k}\Big) + \vartheta_{nk}$$

for $1 \leq k < n$, with $\omega_{n0} = 0$. Ψ_k and ϑ_{nk} are suitably chosen random numbers to account for the roundoff errors. This relation avoids to compute the scalar products $\mathbf{q}_{n+1}^T\mathbf{q}_k$ in every step.

Non–orthogonal vectors usually come in batches; we intend to keep semi–orthogonality at a level $\sqrt{\varepsilon_{\mathrm{mach}}}$ where $\varepsilon_{\mathrm{mach}}$ is the machine precision. Reorthogonalization

is performed for $\mathbf{q}_{n+1}$ if $|\omega_{n+1,k}| \geq \sqrt{\varepsilon_{\text{mach}}}$ against all neighboring $\mathbf{q}_i$, $k - s < i < k + r$, where r and s are the smallest positive indices such that $|\omega_{n+1,k-s}| < \eta$ and $|\omega_{n+1,k+r}| < \eta$, with η being usually chosen as $\eta = \varepsilon_{\text{mach}}^{3/4}$. If a batch has been found, it is used in two consecutive Lanczos steps for reorthogonalization. After reorthogonalization, $\omega_{n+1,i}$ is reset to a random value reflecting the regained orthogonality up to round-off level.

To our experience, Eq. (3.95) estimates the round-off errors quite well, but small underestimations which are randomly occurring might nevertheless destroy orthogonality at a certain point. We thus use the absolute values in the last line of Eq. (3.95), i.e.

$$\omega_{n+1,k} = \frac{1}{\beta_{n+1}}\left(|\beta_{k+1}\omega_{n,k+1}| + |(\alpha_k - \alpha_n)\omega_{nk}| + |\beta_k\omega_{n,k-1}| + |\beta_n\omega_{n-1,k}|\right) + |\vartheta_{nk}| \tag{3.96}$$

and replace ϑ_{nk} (proposed by Simon [74] as $\vartheta_{nk} = \varepsilon_{\text{mach}}(\beta_{k+1} + \beta_{n+1})\Theta$, where Θ is normally distributed with mean 0 and standard deviation 0.3) by the non–random quantity $\vartheta_{nk} = \varepsilon_{\text{mach}}(\beta_{k+1} + \beta_{n+1})$. (Note that $\beta_k > 0$ for all k). $\omega_{n+1,n}$ is evaluated as scalar product instead of using a random number Ψ_{n+1}. While this formula largely overestimates the orthogonality components, no random underestimations will occur in our calculation that could destroy orthogonality. After orthogonalization of $\mathbf{q}_{n+1}$ against $\mathbf{q}_i$, $\omega_{n+1,i}$ is set to $\varepsilon_{\text{mach}}$.

It is reasonable to test for convergence of the first N_{ch} eigenvectors in regular intervals, for example after each integer multiple of N_{ch}. The iteration will then be stopped at a step $N_{\text{Lanczos}} = M_{\text{rep}}N_{\text{ch}}$ if $\max_{k=1,\dots,n}\text{res}(k) \leq r_{\text{max}}$ (this can be replaced by the criterion (3.89)).

For the initial vector $\mathbf{q}_1$, we observe a slight increase in convergence speed when it is computed as the normalized average of the first N_{ch} eigenvectors of the previous sector instead of a randomly chosen vector. Overall, the performance is superior to ARPACK due to the many eigenvectors computed such that contraction of the search space is unfavorable.

3.6.3   The Jacobi–Davidson Method

In the Jacobi–Davidson method [76], the Ritz approximation $(\tilde{\mathbf{x}}, \theta)$ to an eigenpair $(\mathbf{x}, \lambda)$ is not obtained in a Krylov subspace, but in a more general search space $\mathcal{V}_n = \text{span}\{\mathbf{v}_1, \dots, \mathbf{v}_n\}$. The interesting property of this ansatz is that several starting vectors instead of just one can be provided so that the eigenvector information from the previous sector does not have to be collapsed into a single vector. This is especially interesting for the proper resolution of avoided crossings occurring in a small range of the reaction coordinate.

The space $\mathcal{V}_n$ is expanded by computing a Jacobi–Davidson update [77] to the Ritz approximation $\tilde{\mathbf{x}}$:

$$(\mathbf{I} - \tilde{\mathbf{x}}\tilde{\mathbf{x}}^*)(\mathbf{H} - \theta\mathbf{I})(\mathbf{I} - \tilde{\mathbf{x}}\tilde{\mathbf{x}}^*)\mathbf{t} = -\mathbf{r} \tag{3.97}$$

where $\tilde{\mathbf{x}}^*$ denotes transposition. $\tilde{\mathbf{x}} + \mathbf{t}$ is then a better approximation for $\mathbf{x}$.

Eq. (3.97), in turn, has to be solved by some approximate method; a possible choice is MINRES [78]. In this algorithm, a Krylov subspace of size m is build up by the Lanczos recursion and the correction equation is solved approximately in this space. The (maximum) iteration number $m_{\max}$ need not be guessed: The norm of the residual of $\tilde{\mathbf{x}} + \mathbf{t}$ is composed of the norm $||\mathbf{r}_2||$ of the residual resulting from the approximate solution of (3.97) and an error contribution from the deviation of θ from the true eigenvalue:

$$||\mathbf{H}(\tilde{\mathbf{x}} + \mathbf{t}) - \theta(\tilde{\mathbf{x}} + \mathbf{t})||^2 = (\tilde{\mathbf{x}}, \mathbf{H}\mathbf{t})^2 + ||\mathbf{r}_2||^2. \tag{3.98}$$

The Krylov subspace in MINRES can then be expanded as long as $||\mathbf{r}_2||^2$ dominates. Otherwise, it is better to restart with the optimized Ritz value obtained either directly from $\tilde{\mathbf{x}} + \mathbf{t}$ or from rediagonalization of $\mathbf{H}$ in the extended subspace $\mathscr{V}_{n+1} = \mathrm{span}\{\mathbf{v}_1, \dots, \mathbf{v}_n, \mathbf{t}\}$.

3.6.4 Combining Lanczos and Jacobi–Davidson

The drawback we experienced in using the Jacobi–Davidson method lies in the fact that for many eigenvectors to be computed, during the update of a single vector, the Krylov subspace of MINRES will also generate information about the other vectors which is lost once the correction equation (3.97) has been solved. In addition, the subspace $\mathscr{V}_n$ and thus the matrix to be diagonalized might become very large.

A possible way to tackle these problems is to first replace $\tilde{\mathbf{x}}$ by $\tilde{\mathbf{x}} + \mathbf{t}$ instead of augmenting $\mathscr{V}_n$ by $\mathbf{t}$. Second, we can solve the correction equation for the other eigenvector approximations in the same Krylov subspace. More specifically, let $\tilde{\mathbf{y}}$ be such an eigenvector approximation with Ritz value σ, residual $\mathbf{s}$ and assume $\mathscr{W}_m = \mathrm{span}\{\mathbf{w}_1, \dots, \mathbf{w}_m\}$ to be a reasonable part of this Krylov subspace (for example, composed of the m lowest eigenvectors of the tridiagonal matrix $\mathbf{T}_n$, Eq. (3.93)), projected onto the space orthogonal to $\tilde{\mathbf{y}}$. In view of Eq. (3.98), we then need to find a solution to

$$\min_{\mathbf{w} \in \mathscr{W}_m} \left(||\mathbf{b} - \mathbf{H}_\sigma \mathbf{w}||^2 + (\tilde{\mathbf{y}}, \mathbf{H}\mathbf{w})^2 \right) \tag{3.99}$$

with $\mathbf{H}_\sigma = (\mathbf{I} - \tilde{\mathbf{y}}\tilde{\mathbf{y}}^*)(\mathbf{H} - \sigma\mathbf{I})(\mathbf{I} - \tilde{\mathbf{y}}\tilde{\mathbf{y}}^*)$ and $\mathbf{b} = -\mathbf{s}$. Writing

$$\mathbf{w} = \sum_{i=1}^{m} a_i \mathbf{w}_i,$$

and setting the partial derivatives w.r.t the a_i to zero, we obtain the matrix equation

$$\mathbf{H}_{\mathrm{red}}\mathbf{a} = \mathbf{b}_{\mathrm{red}} \tag{3.100}$$

with

$$(\mathbf{H}_{\mathrm{red}})_{ij} = (\mathbf{H}_\sigma \mathbf{w}_i, \mathbf{H}_\sigma \mathbf{w}_j) + (\tilde{\mathbf{y}}, \mathbf{H}\mathbf{w}_i)(\tilde{\mathbf{y}}, \mathbf{H}\mathbf{w}_j) \text{ and} \tag{3.101}$$
$$(\mathbf{b}_{\mathrm{red}})_i = (-\mathbf{s}, \mathbf{H}_\sigma \mathbf{w}_i). \tag{3.102}$$

We can rewrite $\mathbf{H}_{\mathrm{red}}$ as

$$(\mathbf{H}_{\mathrm{red}})_{ij} = \big((\mathbf{H} - \sigma\mathbf{I})\mathbf{w}_i, (\mathbf{H} - \sigma\mathbf{I})\mathbf{w}_j\big) \tag{3.103}$$

showing the positive definiteness (unless σ is an exact eigenvalue) and thus the existence of a local minimum. Solution of the (lower dimensional) equation (3.100) gives the vector $\mathbf{w}$ which can then be used to update $\tilde{\mathbf{y}}$ as $\tilde{\mathbf{y}} + \mathbf{w}$.

The benefit of this procedure lies in the possibility of using several smaller subspaces instead of one large space, and this will decrease reorthogonalization effort which scales quadratically with the number of basis vectors. The Lanczos algorithm usually converges the eigenvalues at the outer parts of the spectrum first; therefore, repeated construction of Krylov subspaces recomputes very similar information. We can of course orthogonalize against converged eigenvector approximations, but doing this in every Lanczos step will introduce unnecessary overhead. In an exact calculation, it should suffice to start with an orthogonalized vector $\mathbf{q}_1$: If the eigenvector approximation $\tilde{\mathbf{x}}$ of $\mathbf{x}$ to be orthogonalized against were exact and if exact arithmetic were used, all consecutive Lanczos vectors would remain orthogonal to $\mathbf{x}$. In practice, similar to (3.91), the scalar product of the initial vector $\mathbf{q}_1$ with $\mathbf{x}$ will be no larger than $\varepsilon_1 = r_\lambda$ if $\mathbf{q}_1$ is numerically orthogonal to $\tilde{\mathbf{x}}$; and the analogous quantities ε_k for the vectors $\mathbf{q}_k$ fulfill a recursion relation

$$\beta_k \varepsilon_{k+1} = (\lambda - \alpha_k)\varepsilon_k - \beta_{k-1}\varepsilon_{k-1} \tag{3.104}$$

where λ is the exact eigenvalue corresponding to $\mathbf{x}$. By monitoring the components of the $\mathbf{q}_k$ in the directions of the converged eigenvectors in this way, we should have to reorthogonalize only when necessary.

Chapter 4

Results

The contents of the first three sections of this chapter have been published [79, 82, 83]. For the sake of brevity, theoretical particularities and numerical details can be found in the corresponding papers. Additional material concerning cross sections can be found in [81] and kinetic isotope effects are studied in [80, 84].

4.1   Cl–Cl Exchange Reaction

4.1.1   Abstract

Time–independent quantum scattering calculations have been carried out on the Walden inversion S_N2 reaction $Cl^- + CH_3Cl'$ $(v_1, v_2, v_3) \rightarrow ClCH_3$ $(v_1', v_2', v_3') + Cl'^-$. The two C–Cl stretching modes (quantum numbers v_3 and v_3') and the totally symmetric internal modes of the methyl group (C–H stretching vibration, v_1 and v_1', and inversion bending vibration, v_2 and v_2') are treated explicitly. A four–dimensional coupled cluster potential energy surface is employed. The scattering problem is formulated in hyperspherical coordinates using the exact Hamiltonian and exploiting the full symmetry of the problem. Converged state–selected reaction probabilities and product distributions have been calculated up to ca. 6000 cm^{-1} above the vibrational ground state of CH_3Cl, i.e. up to initial vibrational excitation $(2, 0, 0)$. In order to extract all scattering resonances, the energetic grid was chosen to be very fine, partly down to a resolution of 10^{-12} cm^{-1}. Up to 2500 cm^{-1} translational energy, initial excitation of the umbrella bending vibration, $(0, 1, 0)$, is more efficient for reaction then exciting the C–Cl stretching mode, $(0, 0, 1)$. The combined excitation of both vibrations results in a synergic effect, i.e. a considerably higher reaction probability than expected from the sum of both independent excitations, even higher than $(0, 0, 2)$ up to 1500 cm^{-1} translational energy. Product distributions show that the umbrella mode is strongly coupled to the C–Cl stretching mode and cannot be treated as a spectator mode. The reaction probability rises almost linearly with increasing initial excitation of the umbrella bending mode. The effect with respect to the C–Cl stretch is five times larger for

more than two quanta in this mode, and in agreement with previous work saturation is found. Exciting the high–frequency C–H stretching mode, $(1,0,0)$, yields a large increase for small energies (more than two orders of magnitude larger than $(0,0,0)$), while for translational energies higher than 2000 cm^{-1}, it becomes a pure spectator mode. For combined initial excitations including the symmetric C–H stretch, the spectator character of the latter is even more pronounced. However, up to more than 1500 cm^{-1} translational energy, the C–H vibration does not behave adiabatically during the course of reaction because only 20 % of the initial energy is found in the same mode in the product molecule. The distribution of resonance widths and peak heights is discussed, and it is found that individual resonances pertinent to intermediate complexes Cl$^-$···CH$_3$Cl show product distributions independent of the initial vibrational state of the reactant molecule. The relatively high reactivity, with respect to excitation of any mode, of resonance states found in previous work is confirmed in the present calculations. However, reactivity of intermediate states and reactivity with respect to initial vibrational excitation have to be distinguished. There is a strong mixing between the vibrational states reflected in numerous avoided crossings of the hyperspherical adiabatic curves.

4.1.2 Introduction

Clary and Palma [91] performed the first quantum scattering and additional classical trajectory calculations on the symmetric chlorine exchange S$_N$2 reaction

$$Cl^- + CH_3Cl' \rightarrow ClCH_3 + Cl' \tag{4.1}$$
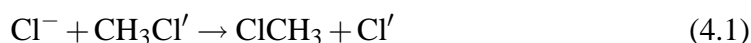
including three internal degrees of freedom: the broken and the formed C–Cl bonds and the CH$_3$ umbrella bending angle. The kinetic energy of the latter mode was expressed in terms of an approximate operator with Legendre polynomials as eigenfunctions. These authors found that excitation of the inversion mode apparently does not have a large influence on the reaction probability. These three–mode calculations were repeated by Yu and Nyman [92] employing a different Hamiltonian that was based on their rotating line umbrella (RLU) method and was exact within the chosen 3D model for the reaction. Here, the umbrella mode was considered as a stretching–type motion of the carbon atom against the three hydrogens with the other degrees of freedom optimized. Yu and Nyman obtained a conclusion very similar to that of Clary and Palma.

In this work, the Hamiltonian developed for the filter–diagonalization calculations of resonances states [94] is used in four–mode quantum scattering calculations on the Walden inversion reaction Cl$^-$ + CH$_3$Cl' $\rightarrow$ ClCH$_3$ + Cl'. To our best knowledge, these are the first four–dimensional (4D) time–independent quantum scattering calculations on a complex–forming bimolecular reaction. They require a high energy resolution and are thus very CPU-intensive.

For an exact description of the Cl$^-$ + CH$_3$Cl' S$_N$2 system, twelve degrees of freedom have to be taken into account explicitly so that a rigorous state–selective quantum

mechanical treatment appears to be impossible at present. Furthermore, if the rotational motion of the whole system were included, the three Euler angles would have to be considered additionally. We thus reduce the dimensionality of the $Cl^- + CH_3Cl'$ $\rightarrow ClCH_3 + Cl'^-$ reaction and study the system under the restriction that C_{3v} symmetry is maintained throughout the reactive process. Since the minimum energy path pertinent to the Walden inversion reaction is collinear and the potential energy rises in all directions perpendicular to the minimum energy path, we adopt a model that explicitly takes into account the two carbon–chlorine distances and the totally symmetric coordinates of the methyl group (corresponding to umbrella bending and symmetric C–H stretching vibrations). As was described in Ref. [94], the motion of the atoms under the restriction of C_{3v} symmetry (for total angular momentum $J = 0$) can be described exactly, i.e., without any further dynamical approximation. However, even in this symmetry–restricted dimensionality–reduced model, the present S_N2 system is computationally rather demanding because the clusters exhibit low intermolecular frequencies in conjunction with far–reaching ion–dipole potentials. Time–independent quantum scattering calculations in four dimensions have been reported for the reaction O (^3P) + $CH_4 \rightarrow OH + CH_3$ by Palma and Clary [85, 86] and Yu and Nyman [87]. However, in this reaction not the methyl group but only a hydrogen atom is transferred and resonances do not play any role because intermediate complexes between the open-shell atom and the spherical top methane are not formed. Palma and Clary studied the influence of excitation of umbrella bending and symmetric and antisymmetric C–H stretching modes on the reaction probability and found that all modes promote the reaction. While this effect is evident for O + CH_4 because one C–H bond is broken and both symmetric and antisymmetric C–H stretch in CH_4 affect this bond, the nature of the C–H stretch in an S_N2 process is entirely different: it does not change during the course of reaction and thus a spectator–like behavior is expected.

Experiments on the detailed, state–selective dynamics of gas–phase S_N2 reactions are scarce. Ervin and co–workers studied the promotion of the $Cl^- + CH_3Cl' \rightarrow ClCH_3$ + Cl' reaction by kinetic energy via guided ion beam tandem mass spectrometry [14]. Bierbaum and coworkers [10] could determine the thermal rate coefficient at 300 K to be $k = (3.5 \pm 1.8) \times 10^{-14} \, cm^3 \, s^{-1}$.

4.1.3   Results

Potential and Surface Eigenstates

Plots along the hyperangle δ with z and q optimized are shown in Fig. 4.1. The cut for $\rho = 10 \, a_0$ has a local maximum in the saddle point region of the PES. For very large values of ρ, two deep wells corresponding to reactants and products are separated by a broad and high potential barrier. Due to the symmetry of the potential, the wavefunctions are either symmetric (gerade) or antisymmetric (ungerade) with respect to $\frac{1}{2}\delta_{max}$. In order to localize the wavefunctions in either of the asymptotic channels, appropriate linear combinations of gerade and ungerade wavefunctions are formed. Note that the
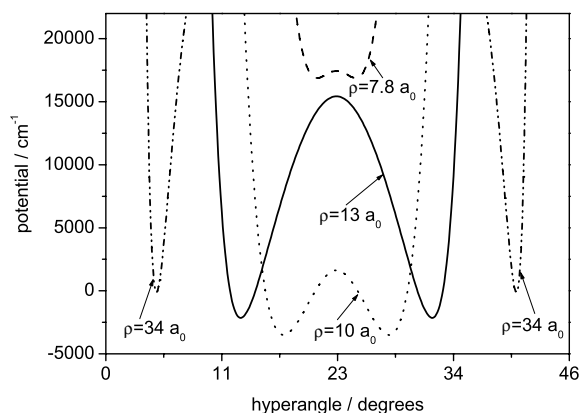
Figure 4.1: Potential cuts along the hyperangle δ for different values of the hyperradius ρ. The energy is optimized with respect to z and q.

spurious wells around $\frac{1}{2}\delta_{max}$ in the PES of Vande Linde and Hase [97] that was used in the quantum scattering calculations reported in Refs. [89, 91, 92] are missing.

The hyperspherical adiabatic curves $\varepsilon_n(\rho)$ as obtained from diagonalization of the surface Hamiltonian for different values of the hyperradius ρ are graphically displayed in Fig. 4.2(a). All curves show a similar behavior with a relatively deep well that resembles the textbook case of a diatomic molecule. Fig. 4.2(b) shows the numerous avoided crossings between the adiabatic curves that mediate the vibrationally non–adiabatic transitions between different channels. In the 2D case [90], the reactivity is determined by the splitting of curves pertinent to the same degree of vibrational excitation but different symmetry [90, 91, 93]. The many additional avoided crossings in the 4D model are the consequence of the two CH_3 modes that are additionally included.

Data are given up to $E = 6100$ cm^{-1} above the vibrational ground state of CH_3Cl. Thus, 35 initial and final states, respectively, are included in our analysis. The energy levels of the asymptotic reactant and product states up to the maximum total energy considered in this work are reported in table 4.1. The wavenumber of the totally symmetric C–H stretching vibration, $v_1 = 3042.5$ cm^{-1}, perfectly agrees with the number obtained in Ref. [94], while the umbrella bending (v_2) and C–Cl stretching (v_3) vibrations are calculated slightly too high and too low, respectively: $v_2 = 1386.0$ (1371.4) cm^{-1} and $v_3 = 720.3$ (727.8) cm^{-1}, where the values in parentheses are those obtained in Ref. [94]. The experimental data are 2967.8 (v_1), 1354.9 (v_2) and 732.8 (v_3) cm^{-1} [95]. It can be seen from table 4.1 that the wavenumber of the umbrella bending mode is almost twice that of the C–Cl stretching mode, $v_2 \approx 2v_3$. The consequence is that there are several groups of initial and final vibrational states (v_1, v_2, v_3) with very similar energies while only a few states, e.g. v_1, are isolated in

Table 4.1: Assignments of quantum numbers (v_1, v_2, v_3) to the initial and final states of the CH_3Cl molecule. Here, v_1, v_2 and v_3 denote the C–H stretching, CH_3 umbrella bending and C–Cl stretching vibrations. Energies $E_{tot} - E_0$ (in cm^{-1}) are given with respect to the vibrational ground state of CH_3Cl ($E_0 = 2446.6$ cm^{-1}).

(v_1, v_2, v_3)	$E_{tot} - E_0$	(v_1, v_2, v_3)	$E_{tot} - E_0$	(v_1, v_2, v_3)	$E_{tot} - E_0$
$(0,0,1)$	720.3	$(1,0,1)$	3764.6	$(1,0,3)$	5186.9
$(0,1,0)$	1386.0	$(0,3,0)$	4114.0	$(0,4,0)$	5457.0
$(0,0,2)$	1432.8	$(0,2,2)$	4156.2	$(0,3,2)$	5496.2
$(0,1,1)$	2098.1	$(0,1,4)$	4181.3	$(0,2,4)$	5510.1
$(0,0,3)$	2138.0	$(0,0,6)$	4215.9	$(0,1,6)$	5539.8
$(0,2,0)$	2757.1	$(1,1,0)$	4434.1	$(0,0,8)$	5576.0
$(0,1,2)$	2801.1	$(1,0,2)$	4479.3	$(1,2,0)$	5805.1
$(0,0,4)$	2836.3	$(0,3,1)$	4812.8	$(1,1,2)$	5849.4
$(1,0,0)$	3042.5	$(0,2,3)$	4837.2	$(1,0,4)$	5887.8
$(0,2,1)$	3462.2	$(0,1,5)$	4862.6	$(2,0,0)$	6049.4
$(0,1,3)$	3495.1	$(0,0,7)$	4898.3	$(0,4,1)$	6149.8
$(0,0,5)$	3528.8	$(1,1,1)$	5146.3		

the spectrum. Groups with two states are $\{(0,1,0), (0,0,2)\}$, $\{(0,1,1), (0,0,3)\}$, $\{(1,1,0), (1,0,2)\}$ and $\{(1,1,1), (1,0,3)\}$. Three states of similar energy are found in the groups $\{(0,2,0), (0,1,2), (0,0,4)\}$, $\{(0,2,1), (0,1,3), (0,0,5)\}$ and $\{(1,2,0),$ $(1,1,2), (1,0,4)\}$, four states in $\{(0,3,0), (0,2,2), (0,1,4), (0,0,6)\}$ and $\{(0,3,1),$ $(0,2,3), (0,1,5), (0,0,7)\}$, and five in $\{(0,4,0), (0,3,2), (0,2,4), (0,1,6), (0,0,8)\}$. The grouping of states is also depicted in Fig. 4.2(a). Note that the asymptotically isolated curve for $(1,0,0)$ starts to interact with other vibrational states at about $\rho = 12$ a_0.

State–Selected Reaction Probabilities

One of the most important fundamental issues in chemistry is the mode–selectivity in elementary chemical reactions. The time–independent quantum scattering calculations yield detailed information on state–to–state reaction probabilities.

Fig. 4.3 depicts the diagonal element of the reaction probability, $P_{mm}(E)$, for the highest open channel m at energy E. As can be seen, $P(E)$ exhibits a pronounced resonance structure. Note that the height of the peaks becomes smaller for higher energies. Since in recent filter diagonalization calculations on lifetimes of resonance states for the $Cl^- + CH_3Cl$ reaction exceedingly long-lived states with very narrow linewidths (smaller than 10^{-8} cm^{-1}) [94] have been found, a much higher energy resolution (down to 10^{-12} cm^{-1}) than in the previous three–dimensional calculations [91, 92]
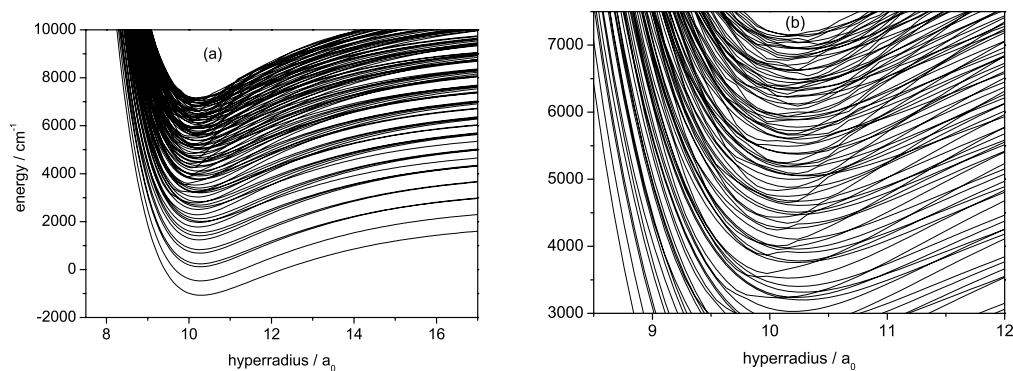
Figure 4.2: Hyperspherical adiabatic curves. Shown are the first 100 states with gerade symmetry. The classical asymptotic limit of the PES is set to zero. While figure 4.2(a) gives the full energy range covered by our calculations, 4.2(b) displays only a small part including many avoided crossings between the curves that mediate transitions between the different adiabatic vibrational states. Note that the curves are plotted only up to hyperradii of 17 a_0 while the actual calculations extend to 34 a_0. The lowest curve approaches the zero point vibrational energy of free CH_3Cl for large ρ (cf. table 4.1).
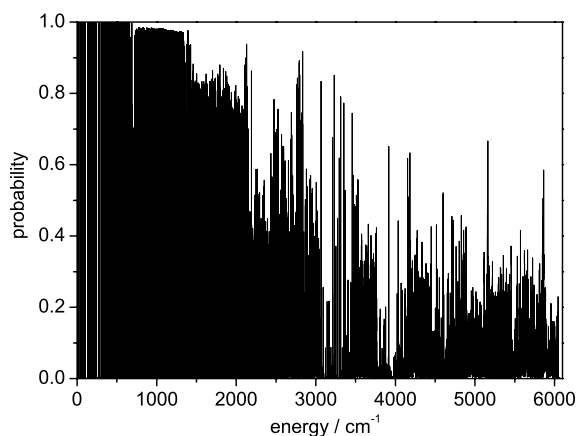
Figure 4.3: The reaction probability $P(E)$ as a function of energy E is strongly dominated by scattering resonances. Shown are the diagonal probabilities $P_{mm}(E)$ for in each case highest open channel m at energy E.
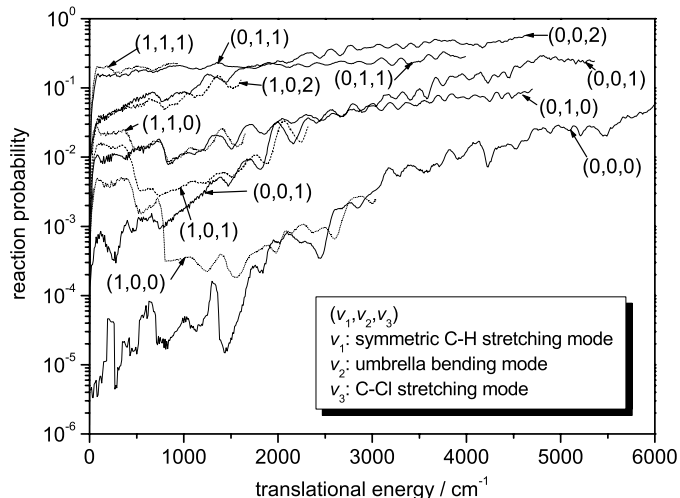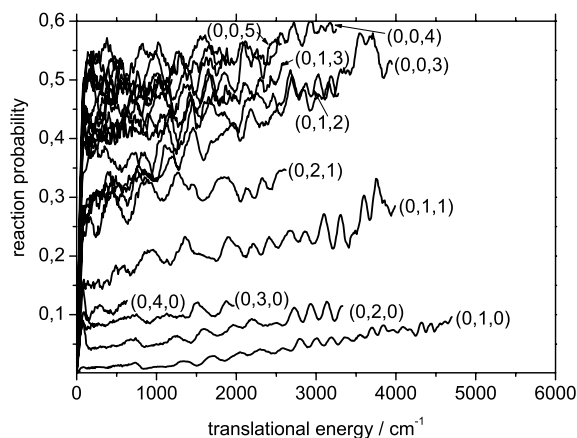
Figure 4.4: Initial state–selected reaction probabilities $P_m(E)$ for $Cl^- + CH_3Cl'$ $(v_1, v_2, v_3) \rightarrow ClCH_3 + Cl'^-$ as functions of translational energy E_{trans}. The data is smoothed over intervals of 80 cm^{-1}. $P_{mn}(E)$ is summed over all accessible product channels n. The dashed curves belong to initial excitation with one quantum in the high–frequency C–H stretching vibration.

was used in order to detect *all* resonances. In order to be able to quantitatively compare the influence of different initial vibrational excitations in the reactant molecules, in the following the strongly fluctuating probabilities were averaged over intervals of $\Delta = 80$ cm^{-1}, i.e. each point $P(E)$ is the average of the probability in the energetic range $[E - \frac{1}{2}\Delta, E + \frac{1}{2}\Delta]$.

The initial state–selected reaction probabilities $P_m(E)$, summed over all product states,

$$P_m(E) = \sum_n P_{mn}(E) = \sum_n |S_{mn}(E)|^2 \qquad (4.2)$$

as functions of translational energy E_{trans} are graphically displayed in Figs. 4.4 and 4.5. Since the curves are not shown as functions of total energy, their energetic range is different. To obtain the probabilities as functions of E_{tot}, shift the energetic scale by the respective level energies given in table 4.1. As anticipated from the two–dimensional results [96], the reaction probability increases with excitation of the intramolecular C–Cl stretching mode v_3.

As seen from Fig. 4.4, the probability with initial excitation $(0,0,0)$ rises with some fluctuations continuously and exponentially. When the C–Cl stretching mode is excited by one quantum, $P(E)$ becomes larger by 2–3 orders of magnitude. For small translational energies, the reaction probability for initial excitation $(0,0,2)$ is

Figure 4.5: Initial state–selected reaction probabilities $P_m(E)$ for $Cl^- + CH_3Cl'$ $(\nu_1, \nu_2, \nu_3) \rightarrow ClCH_3 + Cl'^-$ as functions of translational energy E_{trans}. Same as figure 4.4, but different initial states are shown. Note that the scale of the ordinate is not logarithmic. The curves for initial excitations $(0, 1, 0)$ and $(0, 1, 1)$ are taken from Fig. 4.4 and included for comparison.

two orders of magnitude larger than that for $(0, 0, 1)$. The difference becomes smaller for higher values of E_{trans}, but there is still a considerable jump between these two curves.

According to Fig. 4.5, the probability for initially three quanta in the C–Cl stretch is again somewhat larger, but for initial excitations $(0, 0, 4)$ and $(0, 0, 5)$ a saturation effect is reached in the region $P(E) = 0.5$–0.6. The curves for initial excitation $(0, 0, 6)$, $(0, 0, 7)$ and $(0, 0, 8)$ are not labeled in Fig. 4.5 because they cannot easily be distinguished. All these curves are found in the saturation regime. This behavior is in agreement with the reaction cross sections from two–dimensional calculations on the same PES [96].

From chemical intuition, excitation of the umbrella bending vibration should result in an enhancement of the reactivity. As seen both from Fig. 4.4 and Fig. 4.5, for low translational energies, the curve for $(0, 1, 0)$ is three orders of magnitude higher than that for CH_3Cl initially in its vibrational ground state. Up to about $E_{\text{trans}} = 2500 \text{ cm}^{-1}$, it is even higher than the probability for C–Cl stretch excitation with one quantum, $(0, 0, 1)$. Fig. 4.5 shows that additional quanta in the umbrella bending mode almost linearly increase the reaction probability, but obviously, similar to the excitation in the C–Cl vibration, a saturation effect at around $P(E) \approx 0.1$ is found for even more quanta in ν_2. Note that in particular the oscillation pattern in the averaged $P(E)$ curves is very similar, e.g. between the curves $(0, 1, 0)$ and $(0, 2, 0)$ in the range around $E_{\text{trans}} = 3000$ cm^{-1}.
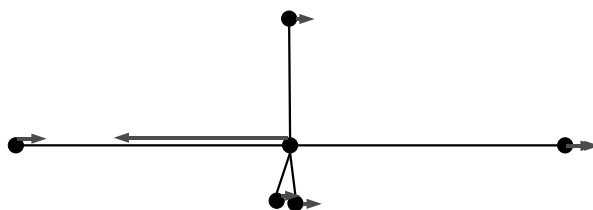
Figure 4.6: Transitional mode of the complex $[\text{Cl}\cdots\text{CH}_3\cdots\text{Cl}]^-$. The normal mode turns out to be a superposition of the antisymmetric Cl–C–Cl stretching and umbrella bending vibrations.

Most striking is a synergic effect when the combination mode $(0,1,1)$ in the reactant CH_3Cl molecule is excited, resulting in a particularly high reaction probability $P(E) \approx 0.15$ that is larger than that for initially four quanta in the umbrella bending mode. Up to about 1500 cm^{-1} translational energy, exciting the combination mode is more effective than putting two quanta into the C–Cl stretching mode. The synergic effect can be explained by the fact that – within the classical picture – in the transition normal mode (with imaginary frequency) both antisymmetric Cl–C–Cl stretch and umbrella bend are included (see Fig. 4.6). This is clear evidence that the umbrella mode does not behave as a spectator in the Walden inversion reaction.

Exciting ν_1, on the contrary, has only a minor effect (see Fig. 4.4) as is expected from the well–known 'spectator' mode concept: A bond that is not directly involved in the reaction can be treated adiabatically and does not show a significant influence on the reactivity. However, this picture is too simplified as is further discussed in the following section. The reaction probability for one quantum in the C–H stretch, $(1,0,0)$, is only small, but in the range up to ca. 1900 cm^{-1} translational energy remarkably larger than the probability for reaction out of the vibrational ground state of CH_3Cl. Above this energy, the two curves show a very similar structure, where the $(1,0,0)$ probability is slightly shifted to higher values of E_{trans}. For the combination mode $(1,1,0)$ excited in reactant CH_3Cl, the corresponding probability is larger than that for pure umbrella bending excitation, $(0,1,0)$, only for translational energies up to ca. 500 cm^{-1}, while for higher energies, the curves almost coincide. The same effect is observed for initial states $(1,0,1)$ and $(0,0,1)$, where the reaction probability corresponding to the former excitation is higher up to translational energies of about 1250 cm^{-1}. This behavior can be explained by the fact that the actual reaction barrier is higher than that given by the classical potential. For the reaction to proceed with a

considerable probability, three quanta are necessary in the stretching mode corresponding to the C–Cl bond to be broken. Below this energy, the high–frequency C–H stretch plays an important role, as can be seen from the $(1,0,0)$ reaction probability. For a simultaneous excitation of the C–Cl stretching mode, $(1,0,1)$, there is already one quantum in that mode and the range of translational energy where v_1 is of importance becomes smaller. The same holds for initial excitation of v_2 which is strongly coupled to the reaction coordinate (see above) so that the different offsets between the curves can be explained. Accordingly, the probabilities for initial excitations $(1,0,2)$, $(1,1,1)$ and $(1,0,3)$ almost coincide with those for $(0,0,2)$, $(0,1,1)$ and $(0,0,3)$, respectively, because there is already sufficient energy in the reactant molecule to overcome the barrier to reaction.

Two approximate 3D time–independent quantum studies of the reaction

$$Cl^- + CH_3Cl'(v_2, v_3) \rightarrow ClCH_3(v_2', v_3') + Cl'^- \qquad (4.3)$$
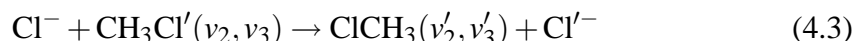
have been published by Clary and Palma [91] and Yu and Nyman [92], respectively. In both cases, the old PES of Vande Linde and Hase [97] was used and the energetic resolution of the calculated reaction probabilities was rather low (0.81 cm^{-1}). Clary and Palma modified the RBA model and used the rotational kinetic energy of a linear molecule without azimuthal dependence for the umbrella bending motion and thus obtained an approximate Hamiltonian. Yu and Nyman employed the C–H$_3$ distance to describe that mode (similar to the present work) and optimized the C–H bond length in the potential energy. The latter model is exact in 3D with the C–H bond distance optimized with respect to energy and thus somewhat more reliable than that of Clary and Palma. In the present work, the previous investigations are extended in five directions: (1) The symmetric C–H stretching mode is included explicitly in the quantum treatment; (2) within the four–dimensional C_{3v} symmetric coordinate subspace, the corresponding Hamiltonian is formulated exactly; (3) a reliable PES constructed from *ab initio* energy points at the CCSD(T) level of theory is employed; (4) the energetic resolution is orders of magnitude higher so that also extremely small resonances can be detected; (5) the range of total energy considered in the collision process is about twice as large.

While the absolute reaction probability for initial excitation of the umbrella bending mode is only slightly smaller in Clary and Palma's work compared to the present results, its relative magnitude with respect to the probability for reaction out of the vibrational ground state of CH$_3$Cl is considerably smaller in Ref. [91] because Clary and Palma obtain a larger result for the latter quantity. Thus, their conclusion was that the umbrella bending mode behaves as a spectator. Our finding that exciting state $(1,1)$ in the reactant molecule has a particularly large effect on the reactivity is in clear contrast to Clary and Palma [91] who predict the influence of the combination excitation to be even smaller than initial excitation $(0,1)$. This is additional evidence that the umbrella mode must not be neglected in quantum reaction dynamics on S$_N$2 and related reactions.

Yu and Nyman[1] cover translational energies for initial excitation $(0,0)$ up to ca. 3200 cm^{-1} and correspondingly smaller ranges for $(0,1)$ and $(1,0)$. The reaction probability for initial excitation of the umbrella bending mode rises from 0.1 to 0.2 at $E_{\text{trans}} = 1600$ cm^{-1}, in good agreement with the results of the present work. The probability for $(0,0)$ is slightly larger than that of the present work, while that for $(0,1)$ is considerably increased. The present results show that in the energetic regime of Yu and Nyman's work, the reaction probability for initial excitation $(0,1)$ is throughout below that for $(1,0)$, while Yu and Nyman, on the contrary, obtain the reverse result for $E_{\text{trans}} > 700$ cm^{-1}. Results on the effect of a combined excitation of v_2 and v_3 on the reactivity of the S$_N$2 reaction are not reported by Yu and Nyman. Since their Hamiltonian was exact within their 3D model, the differences to the reaction probabilities from the present work are mainly due to the disparate potential energy surfaces.

Product Distributions

If state–to–state reaction probabilities are normalized, $P_{mn}(E)/P_m(E)$, product distributions are obtained. They are equivalent to relative probabilities with respect to a particular initial state. Absolute state–to–state reaction probabilities can be recovered by multiplying the summed absolute values in Figs. 4.4 and 4.5 with the percentage amounts of the product distributions.

Product distributions for the Cl$^-$ + CH$_3$Cl$'$ (v_1, v_2, v_3) → ClCH$_3$Cl (v_1', v_2', v_3') + Cl$'^-$ reaction are graphically displayed in Figs. 4.7–4.11. Only the most important product channels are shown, the curves corresponding to channels which are populated only to a very minor extent are not shown in the figures.

From Fig. 4.7, it is obvious that the reaction out of the vibrational ground state of CH$_3$Cl is most likely to end in product states with a high degree of vibrational excitation in the C–Cl stretching mode. Of course, for low translational energies, the only open channel is $(0,0,0)$. When a new channel with pure excitation in v_3 opens up, it becomes dominating in the product distribution until the next one opens (up to $v_3 = 4$). However, for E_{trans} larger than 4000 cm^{-1}, the product states $(0,0,1)$ and $(0,0,2)$ become most important. Also, the umbrella mode, $(0,1,0)$, and the combined excitation $(0,1,1)$ exhibit significant values in the product distribution.

Inspecting the product distributions for initial vibrational states $(0,0,i)$, $i = 1,2,3$ (Fig. 4.8), a similar behavior is observed, in particular for initially one quantum in the C–Cl stretching vibration; for high E_{trans}, product excitations $(0,0,1)$ and $(0,0,2)$ dominate, while all other product vibrational states have only small probabilities. Thus, the transfer from vibrational energy (V) into translational energy (T) is only weak. For initial state $(0,0,2)$, reaction in the equivalent product state is most likely, but also final state $(0,0,3)$ is important for E_{trans} between 700 and 3000 cm^{-1}. For higher translational energies, it is most likely to find the same number of quanta in

---

[1]Note that in their work, Yu and Nyman use the convention (v_3, v_2) instead of the spectroscopically motivated nomenclature (v_2, v_3).
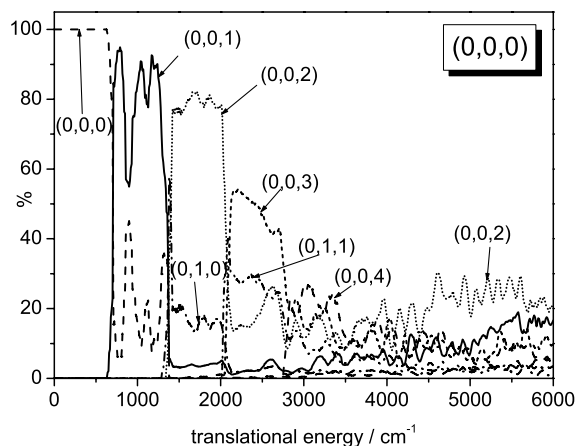
Figure 4.7: Product distribution for $Cl^- + CH_3Cl'$ $(0,0,0) \rightarrow ClCH_3$ (v'_1, v'_2, v'_3) + Cl'^- for CH_3Cl being initially in its vibrational ground state. The data is smoothed over intervals of 80 cm^{-1}.

v_3 in reactant and product CH_3Cl. Note that also product states with excitation of the umbrella bending mode play an important role, indicating the active role of this mode in the reaction. For initial excitation $(0,0,3)$, a similar effect can be seen. The same product state as in the reactant molecule dominates up to 3000 cm^{-1}. Also, the near–resonant mode $(0,1,1)$ has a significant role, as well as the neighboring states $(0,0,2)$ and $(0,0,4)$ and the combined excitation $(0,1,2)$. Again, V $\rightarrow$ T energy transfer is not observed.

As can be seen from Fig. 4.9, exciting the umbrella bending mode in reactant CH_3Cl favors products in the near–resonant state $(0,0,2)$ while the state $(0,1,0)$ is important only for low translational energies and shows a low population indicating that v_2 is not to be considered as a spectator mode. Also the states $(0,0,3)$, and to a minor extent, $(0,0,1)$ and $(0,0,4)$ are populated in the product molecule. Furthermore, the combined excitations $(0,1,1)$ and $(0,1,2)$ are found in the product, indicating a strong tendency for T $\rightarrow$ V energy transfer when the umbrella mode is initially excited. Analogously, two quanta in the umbrella bending mode yield the product most likely in the state $(0,0,4)$, but also in the neighboring states $(0,0,3)$ and $(0,0,5)$. The near–resonant product state $(0,1,2)$ is particularly important; its contribution drops from 40 to 5% at 1500 cm^{-1} and then slowly rises again. The percentage of product state $(0,2,1)$ is also remarkable, confirming the tendency to T $\rightarrow$ V energy transfer. Three or four quanta in v_2 yield preferably a product with a high degree of excitation in the C–Cl mode, viz. $(0,0,6)$ and $(0,0,8)$, respectively. Initially $v_2 = 3$ populates also the near–resonant product states $(0,1,4)$ and $(0,2,2)$ as well as $(0,0,7)$ and $(0,3,1)$ while $v_2 = 4$ prefers the near–resonant states $(0,1,6)$, $(0,2,4)$ and $(0,3,2)$ and a state with
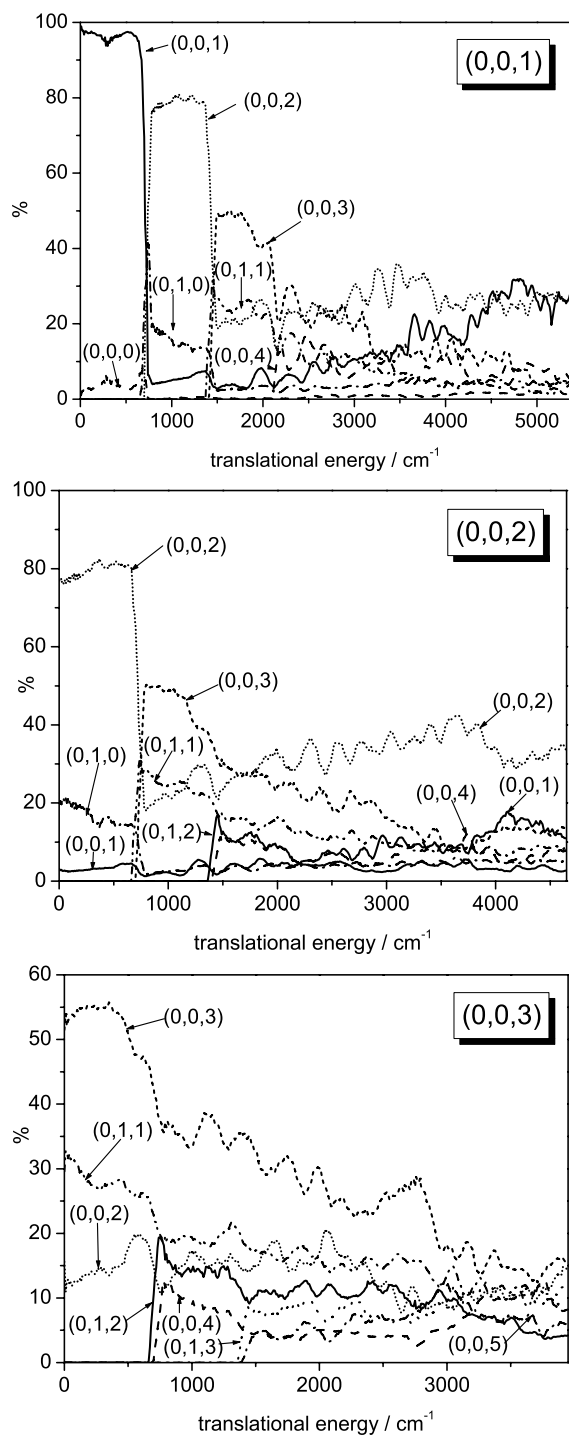
Figure 4.8: Product distribution for $Cl^- + CH_3Cl'$ $(0,0,i) \rightarrow ClCH_3$ $(v_1', v_2', v_3') + Cl'^-$ with the C–Cl stretching vibration in CH_3Cl initially excited with $i = 1$, 2, or 3 quanta, respectively. The data is smoothed over intervals of 80 cm^{-1}.
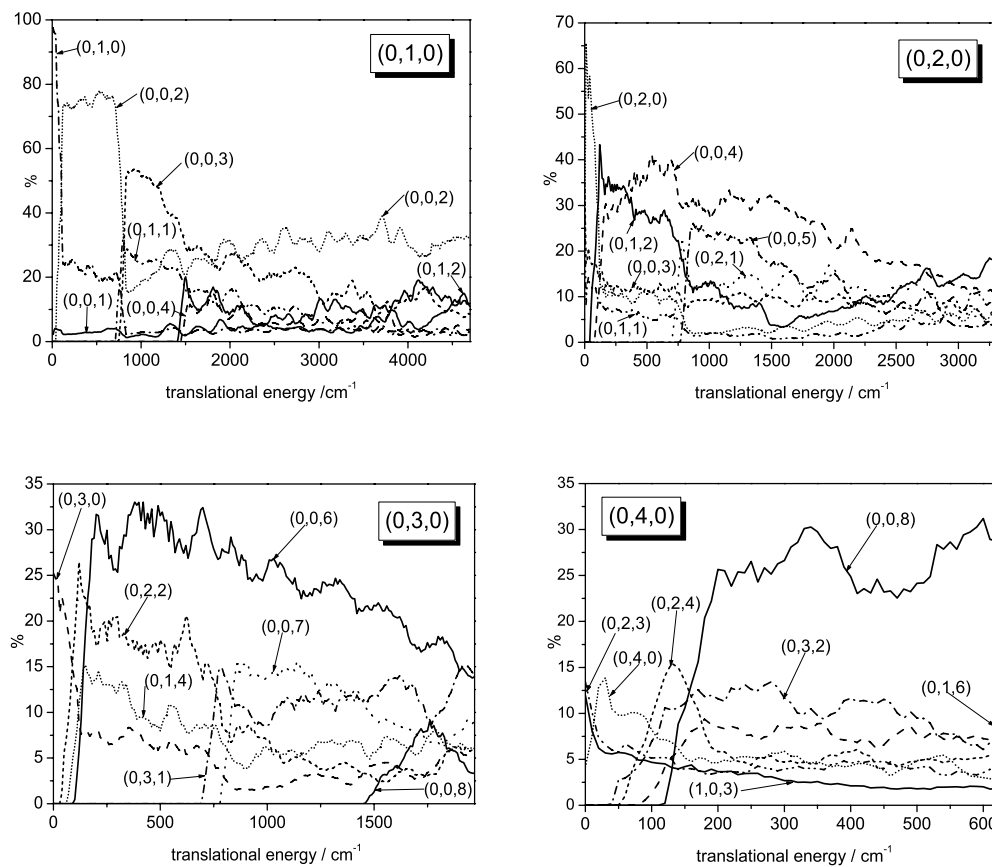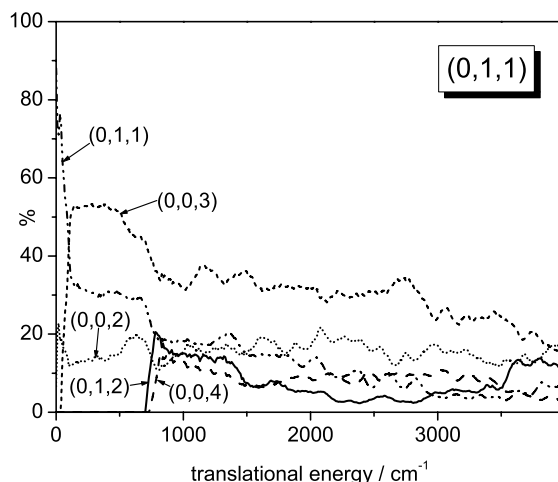
Figure 4.9: Product distribution for $Cl^- + CH_3Cl'$ $(0,i,0) \rightarrow ClCH_3$ $(v_1', v_2', v_3') + Cl'^-$ with the umbrella bending vibration in CH_3Cl initially excited with $i = 1$, 2, 3 or 4 quanta, respectively. The data is smoothed over intervals of 80 cm^{-1}.

Figure 4.10: Product distribution for $Cl^- + CH_3Cl'$ $(0,1,1) \rightarrow ClCH_3$ (v_1', v_2', v_3') + Cl'^- where CH_3Cl is initially excited with one quantum in the umbrella bending and one quantum in the C–Cl stretching vibration. The data is smoothed over intervals of $80 \, \text{cm}^{-1}$.

excitation of the high–frequency C–H stretching mode, $(1,0,3)$.

Fig. 4.10 shows the product distribution for initially one quantum in the C–Cl and one in the umbrella mode. The most important product state is the near–resonant level $(0,0,3)$, followed by $(0,0,2)$, $(0,0,4)$ and $(0,1,2)$.

Finally, the product distribution for initial vibrational state $(1,0,0)$ is shown in Fig. 4.11. Compared to all other product distributions discussed above, a strong mixing between the states is observed. The probability for finding products with $(1,0,0)$, i.e. adiabatic behavior of v_1, is about 20% up to $E_{\text{trans}} = 800 \, \text{cm}^{-1}$. There, the percentage of the adiabatic reaction drops down to zero. Asymptotically, the reactant v_1 mode is not in near–resonance with any other energy level, but interacts with other states (cf. Fig. 4.2) for smaller ρ values. We find product excitations $(0,0,3)$, $(0,0,4)$, $(0,0,5)$, $(0,1,2)$ and $(0,2,2)$ indicating vibrational energy redistribution from the C–H stretching mode into the "active" degrees of freedom, v_2 and v_3. Up to about E_{trans} = 1900 cm^{-1}, energy originally stored in the high–frequency C–H stretching mode is released in the other degrees of freedom and by no means conserved in v_1. Thus, also the C–H stretching mode plays an active role in the dynamics and should not a priori be neglected. For thermal reactions, the influence of this low–populated mode is fairly small, while in the detailed dynamics of the reaction, in particular at higher energies, also the so-called 'spectator' modes should be included. This conclusion is supported by independent calculations on the decay of the resonance states [94]. However, it should be kept in mind that the lifetimes of localized resonances (v_1, v_2, v_3, v_4), where
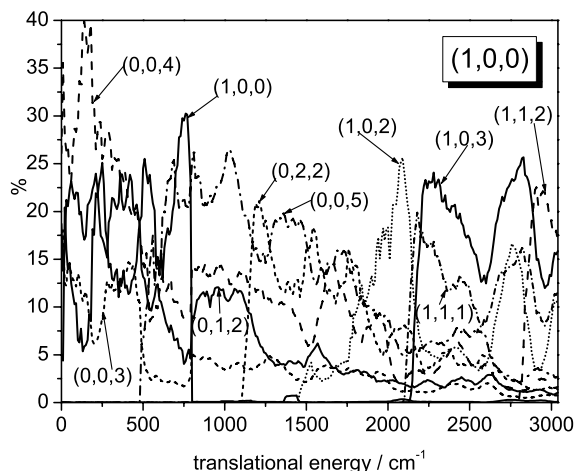
Figure 4.11: Product distribution for $Cl^- + CH_3Cl'$ $(1,0,0) \rightarrow ClCH_3$ $(v'_1, v'_2, v'_3) +$ Cl'^- with the CH_3Cl molecule initially with one quantum in the high–frequency C–H stretching vibration. The data is smoothed over intervals of 80 cm^{-1}.

v_4 is the intermolecular Cl–C stretching mode, in the intermediate complexes and the reaction probabilities dependent on reactant CH_3Cl (v_1, v_2, v_3) are intrinsically differ-ent. Thus, the high reactivity of the resonant states that does not cope with the spectator mode concept and the spectator–like behavior of the reactant C–H stretching mode in the reactive process are not in contradiction. The crossings of the adiabatic states when going from the asymptotic to the interaction region of the PES play a crucial role.

For translational energies higher than 1900 cm^{-1}, preferably T $\rightarrow$ V energy trans-fer takes place, and the v_1 mode behaves adiabatically. This is in close agreement with the energy starting from which the reaction probability is almost coincident with that for reaction out of the vibrational ground state of CH_3Cl as shown in Fig. 4.4 and discussed before. The product states that are excited above $E_{\text{trans}} = 1900$ cm^{-1} are $(1,0,2)$, $(1,0,3)$, $(1,1,1)$ and $(1,1,2)$. Surprisingly, $(1,0,1)$ is not found according to our calculations.

Comparing the product distributions shown in Figs. 4.7–4.11, in particular for ini-tial states $(0,0,0)$, $(0,0,1)$, $(0,0,2)$ and $(0,1,0)$, a surprising similarity can be found, at least up to the openings of the $(0,1,1)$ and $(0,0,3)$ channels. The state–to–state reac-tion probabilities show roughly the same ratios. Obviously, the long–living resonances decay into products independently of the way they were formed from reactants. Only the absolute heights of the state–to–state probabilities vary and depend on the initial vibrational state.

Analysis of Resonance Structure

As inferred from the symmetry of the PES, many resonances appear as double peaks with remarkably small linewidths. The energetically higher lying states (ungerade symmetry) exhibit smaller line widths which is in agreement with the numerically more accurate filter diagonalization results reported in Ref. [91]. A general distinction of the resonances in states with gerade and ungerade symmetry can not be accomplished in the scattering calculations because wavefunctions are not obtained.

Fig. 4.12 contains a comparison with previous 4D resonance calculations [94] showing that the overall agreement of the two distributions is fairly sound. While the underlying Hamiltonian and the PES are identical for both methods – Tschebyscheff filter diagonalization [94] and time–independent scattering in hyperspherical coordinates –, the two approaches themselves are completely different. In Ref. [94], complex absorbing potentials were used and the resonance energies, linewidths and wavefunctions were directly obtained from the diagonalization of a 4D Hamiltonian matrix. The results are limited to localized resonances due to the finite size of the grid. Thus, the lower limit of the resonance distribution is well characterized while the upper limit is not because very far–reaching resonance wavefunctions cannot be calculated exactly. In the present work, we do not obtain wavefunctions and therefore cannot assign quantum numbers. Again, the lower limit of the resonance width distribution is well characterized because – provided the energetic resolution is sufficiently high – the narrow but intense peaks can be fitted to Lorentzian profiles. However, small peaks with large widths are very difficult to identify in the spectrum, in particular in the higher energy regime where the resonances overlap and a considerable background is found. Thus, the upper border of the $\Gamma(E)$ distribution is not well defined. Note in particular that the filter diagonalization method yields some states with extremely large widths which are very well localized above the saddle point region of the PES (see Fig. 4.12 and Ref. [94] for details). These resonances could not be resolved in the present work. However, the time–independent scattering approach has several advantages: First, we obtain additional information about the heights of the peaks in the spectrum and thus about the contribution of the individual resonances to the reactive processes. Second, the energetic range can be considerably extended at much lower cost than in the filter diagonalization procedure where the yield of acceptable resonances becomes extremely low at higher energies compared to the strongly increasing computational effort. To highlight the good agreement of the two distributions shown in Fig. 4.12, we refer to the work of Zhang and Smith [99] who studied the HO_2 system that might be viewed as an intermediate in a complex–forming bimolecular reaction. The authors carried out filter diagonalization calculations using the Lanczos subspace and Tschebyscheff low storage methods (employing identical Hamiltonians and PESs) and obtained similar deviations of their $\Gamma(E)$ distributions.

As is to be expected and can clearly be seen in the overview of the reaction probabilities, Fig. 4, the opening of a new channel has a significant effect on the resonance structure as computed by time–independent scattering calculations, whereas it is not
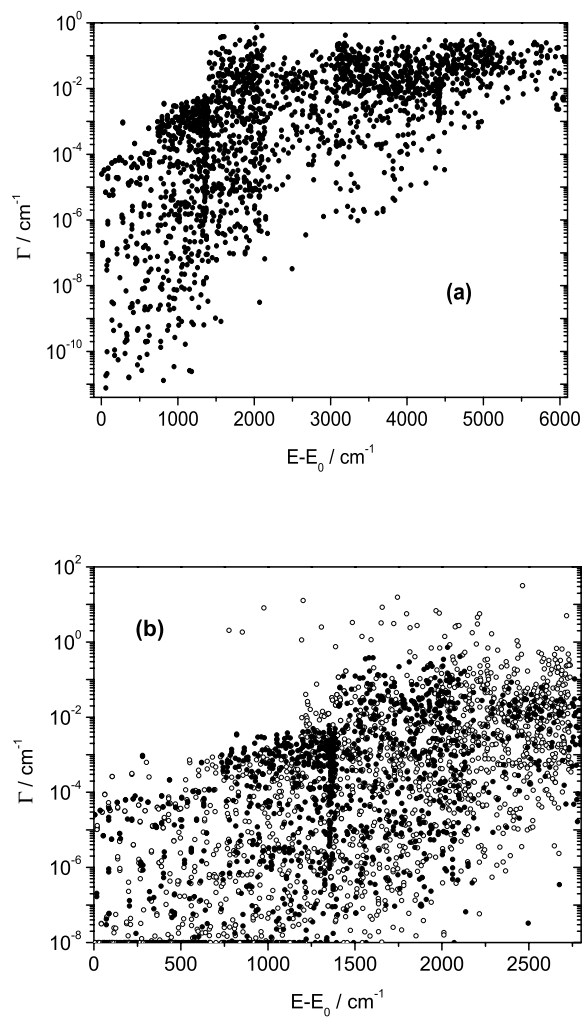
Figure 4.12: (a) Resonance width distribution as function of excess energy $E - E_0$, where E_0 is the vibrational ground state of CH_3Cl. (b) Comparison of the data with results from Ref. [94] (open circles). In (b), all widths below 10^{-8} cm^{-1} are set to 10^{-8} cm^{-1}.
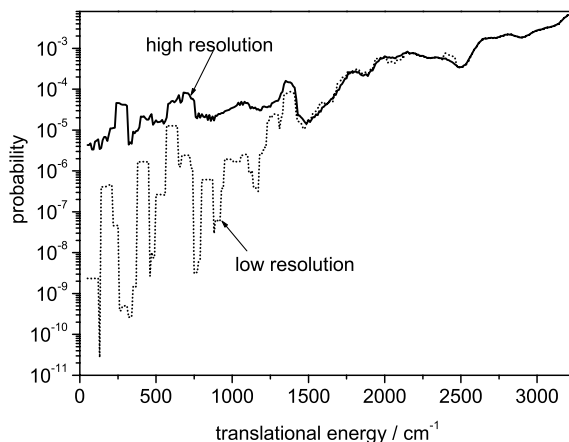
Figure 4.13: Comparison of reaction probabilities for initial state $(0,0,0)$, summed over all product states, from this work, computed employing high energetic resolution (full line) and the coarse energy grid of 0.81 cm^{-1} from Ref. [91] (dotted line).

important in the filter diagonalization.

The significance of the very narrow resonances that were not detected by Clary and Palma [91] and Yu and Nyman [92] is most important in the low translational energy regime, where the density of resonance states is low (see Fig. 4.13). In the higher energy regime where broad resonances dominate the spectrum, their contribution to the reaction probability becomes less important. However, under thermal conditions the low–energy scattering is relevant and thus accurate calculations are necessary.

The sum of all peak heights of a particular resonance appearing in all state–to–state selected reaction probabilities amounts to one[2]; however, the heights of the individual resonance peaks vary over several orders of magnitude (Fig. 4.14). As for the linewidths, the opening of new channels leaves its marks; the obviously smaller density of fitted peaks after an energy of 2000 cm^{-1} can be explained by the opening of the very reactive modes $(0,1,1)$ and $(0,0,3)$; afterwards, the background is considerably higher while the total probability of one is distributed on more channels so that many of the peaks are difficult to identify. Note in addition that the density pattern is somewhat repeated for energies higher than 3000 cm^{-1}, i.e. where states with one quantum in the C–H-stretching mode appear.

Of considerable interest are product distributions computed from complete resonances, Fig. 4.15. They are independent of the initial state, reflecting that a long–lived resonance state decays independently of the way it is formed. This implies that the ratios of the elements of the matrix $\mathbf{P}^{\mathrm{res}}$ containing all the peak heights of a specific resonance are independent of the row of this matrix. Due to symmetry, $P_{mn}^{\mathrm{res}} = P_{nm}^{\mathrm{res}}$, the
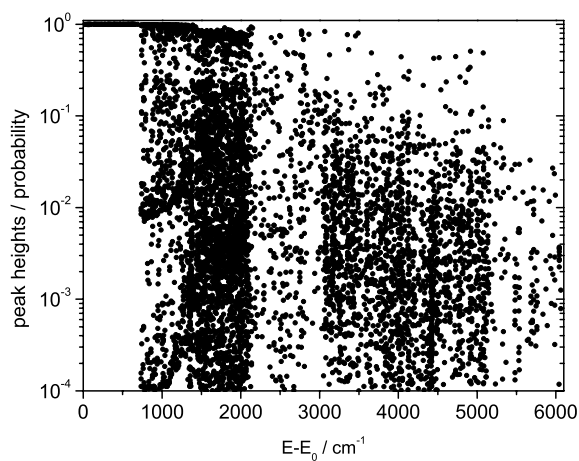
---

[2]See [88] for a similar case.

Figure 4.14: Distribution of peak heights in the reaction probability vs. energy for all possible combinations of initial and final states. Note that resonances have been fitted if $P_{\min} \geq 10^{-4}$.
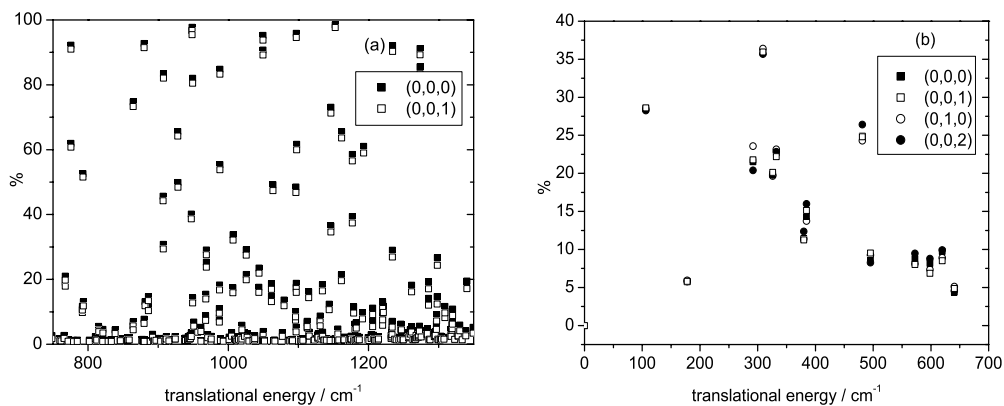

Figure 4.15: Probability for finding product states $(0,0,0)$ (a) and $(0,1,0)$ (b) for different initial vibrational states at resonance energies in selected energy intervals. Only complete resonances (with $\sum\limits_{i,j} P_{ij} = 1$) have been included.

state–to–state selected reaction probabilities show the same ratio. The matrix $\mathbf{P}^{\text{res}}$ (or, respectively, the corresponding resonance state) can thus be characterized by $N-1$ numbers if $N \times N$ is the size of the matrix (and the general requirement that the sum of all elements is equal to unity). Note that the product distributions show obvious differences between the resonances; as can be seen from Fig. 4.15(a), most of the resonances will decay in final states with one quantum of the C–Cl–stretching mode, but some behave just the other way round. In Fig. 4.15(b), the proportion of excitation of the umbrella mode in the decay products also varies largely; it seems to become less important for large energies which corresponds to the overall picture described in the previous sections.

Looking again at the product distributions as computed from the complete spectrum, Figs. 4.7–4.11, independence from the initial state can be found as well, at least in the energetic regime up to $2000 \, \text{cm}^{-1}$ when the $(0,1,1)$ and $(0,0,3)$ modes open up. This is another hint that the reaction up to that energy is driven by resonances as suggested by Fig. 4.13 up to an energy of $1500 \, \text{cm}^{-1}$.

4.1.4   Conclusions

(1) Employing a coupled cluster [CCSD(T)) potential energy surface, time–independent quantum scattering calculations up to $6000 \, \text{cm}^{-1}$ above the vibrational ground state of the reactant molecule have been carried out on the S_N2 reaction $Cl^- + CH_3Cl'$ $\rightarrow ClCH_3 + Cl'$ using hyperspherical coordinates to describe the bonds being broken and formed. The two totally symmetric modes of the methyl group, C–H stretching and umbrella bending, are explicitly included in the model. C_{3v} symmetry is conserved throughout the reaction. The Hamiltonian used is exact within the 4D dimensionality–reduced model.

(2) A very narrow grid in the total energy was employed so that extremely long living resonance states with widths down to $10^{-12} \, \text{cm}^{-1}$ could be resolved. In particular, it was possible to detect two components of these peaks corresponding to gerade and ungerade resonance states, in agreement with recent filter diagonalization calculations in the energetic continuum. The distribution of the resonance widths agrees well with that from the previous work and extends it towards higher energies.

(3) State–selected reaction probabilities as functions of translational energy are presented and discussed in detail. Product distributions, closely related to state–to–state reaction probabilities, are analyzed.

(4) While excitation of the pure umbrella bending mode already leads to a significant enhancement of the reaction probability, its combination with vibrational excitation of the broken C–Cl bond results in a strong synergic effect. This can be explained by the similarity of the combination excitation with the reaction transition mode. The umbrella bending vibration is by no means a pure spectator in the S_N2 reaction.

(5) While exciting the high–frequency symmetric C–H stretching vibration has a considerable influence for low translational energies and initial vibrational states up to $(0,1,0)$, otherwise only a small effect on the reaction probability is observed in

agreement with the spectator mode concept. However, this concept in questionable in so far as energy originally stored in the v_1 mode is released in the other modes of the reaction products. Thus, though quantitatively small, the role of the C–H mode in the reaction dynamics is not negligible.

(6) Product distributions of individual resonances can be calculated from their peak heights in different state–to–state reaction probabilities. It is found that the decay of the resonances is independent of the initial vibrational state of the reactant.

(7) The next step in studying the S_N2 elementary reaction is to leave the collinear reaction pathway and to consider various directions of approximation of the nucleophile towards the methyl halide molecule. It is anticipated that the reaction probability is strongly decreased. While the rotation of the methyl group around its axis of symmetry (A rotational constant) was already an object of investigation [89], the rotation of the methyl halide molecule around an axis orthogonal to its axis of symmetry, i.e. the motion connected with the B rotational constant, requires two different coordinate systems for reactants and products and the use of suitably adapted basis sets.

4.2   Cl–Br Exchange Reaction

4.2.1   Abstract

The exothermic gas–phase S_N2 reaction $Cl^- + CH_3Br$ $(v_1', v_2', v_3') \to ClCH_3$ (v_1, v_2, v_3) $+ Br^-$ and the corresponding endothermic reverse reaction have been studied by time–independent quantum scattering calculations in hyperspherical coordinates on a coupled cluster (CCSD(T)) potential energy surface. The dimensionality–reduced model takes four degrees of freedom into account (Cl–C and C–Br stretching modes (quantum numbers v_3' and v_3); totally symmetric modes of the methyl group, i.e. C–H stretching (v_1' and v_1) and umbrella bending vibrations (v_2' and v_2)). Diagonalization of the Hamiltonian was performed using the Lanczos algorithm with a variation of partial re-orthogonalization. A narrow grid in the total energy was employed so that long–living resonance states could be resolved and extracted. While excitation of the reactant umbrella bending mode already leads to a considerable enhancement of the reaction probability, its combination with vibrational excitation of the broken C–Br bond, $(0, 1, 1)$, results in a strong synergic effect that can be rationalized by the similarity with the classical transitional normal mode. Exciting the C–H stretch has a non–negligible effect on the reaction probability, while for larger translational energies this mode follows the expected spectator–like behavior. Combination of C–Br stretch and symmetric C–H stretch, $(1, 0, 1)$, does not show a cooperative effect. Contrary to the spectator mode concept, energy originally stored in the C–H stretching mode is by no means conserved, but released in other modes of the reaction products. Products are most likely formed in states with a high degree of excitation in the new C–Cl bond, while the internal modes of the methyl group are less important. Reactants with combined

umbrella/C–Br stretch excitation, $(0, 1, 1)$, may yield products with two quanta in the umbrella mode.

4.2.2 Introduction

In this section, we present a four–dimensional (4D) study of the exothermic reaction

$$Cl^- + CH_3Br \rightarrow ClCH_3 + Br^- \tag{4.4}$$
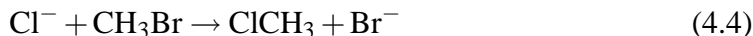
and the corresponding endothermic reverse reaction. The first quantum mechanical study on a gas–phase S_N2 reaction was performed by Wang, Goldfield and Hase [100] who studied the time–dependent dynamics of a two–dimensional (2D) wave packet in a model with the minimum number of degrees of freedom (carbon–halogen bonds being formed and broken). Clary [13] could obtain the thermal rate constant from a dimensionality–reduced three–dimensional (3D) quantum model with an approximate Hamiltonian for the umbrella bending coordinate and found good agreement with experiment. Reaction cross sections in a 2D model were calculated and analyzed by Schmatz and Clary [31]. A 2D investigation of resonance lifetimes for the complexes $Cl^- \cdots CH_3Br$ (entrance channel) and $ClCH_3 \cdots Br^-$ (exit channel), obtained directly as the imaginary parts of the complex eigenvalues, $E = E_{res} - \frac{i}{2}\Gamma$, of a complex–symmetric Hamiltonian matrix was reported by Schmatz *et al.* [32] who employed a coupled–cluster (CCSD(T)) potential energy surface in conjunction with the filter diagonalization method. The five stationary points (reactants, products, saddle point and the two intermediate complexes) on this surface had already been reported in Ref. [101]. In a recent paper, Schmatz [102] reported the linewidths for the same system in a four–mode model on an extended PES. The four–dimensional model also includes the two totally symmetric vibrations of the methyl group (C–H stretch and umbrella bend). The vast majority of bound states and many resonance states up to the first overtone of the symmetric stretching vibration in the exit channel complex have been calculated, analyzed and assigned four quantum numbers. The resonances were classified into entrance channel, exit channel and delocalized states. It could be shown that the widths of the resonances within a small energy window cover more than six orders of magnitude. In addition to a majority of Feshbach–type resonances, exceedingly long-lived shape resonances were found which are associated with the entrance channel and can only decay by tunneling. The state–selective decay of the resonances was studied in detail. The linewidths of the resonances and thus the coupling to the energetic continuum increase with excitation in *any* mode. Due to the strong mixing of the many progressions in the intermolecular stretching modes of the intermediate complexes, this increase as a function of the corresponding quantum numbers is not monotonic, but exhibits pronounced fluctuations.

In the present work, we use the same dimensionality–reduced Hamiltonian as employed in Ref. [102]. A rigorous quantum mechanical treatment appears to be impossible at present because for an exact description of the $Cl^- + CH_3Br$ S_N2 system,

twelve degrees of freedom have to be considered explicitly. The dimensionality of the reaction is thus reduced and the system is studied under the restriction that C_{3v} symmetry is maintained during the reaction. Since the minimum energy path (MEP) of the reaction is strictly collinear and the potential energy rises in all directions perpendicular to that pathway, we adopt the model that explicitly takes into account the two carbon–halogen distances and the totally symmetric coordinates of the methyl group (corresponding to umbrella bending and symmetric C–H stretching vibrations). Due to the low intermolecular frequencies of the complexes, the heavy mass of the bromine nucleus and the far–reaching ion–dipole potentials, the $Cl^- + CH_3Br$ S_N2 system is computationally very demanding, even in the dimensionality–reduced model.

Experimentally, the system $Cl^- + CH_3Br \rightarrow ClCH_3 + Br^-$ has considerable advantages over $Cl^- + CH_3Cl'$ that was previously studied by quantum mechanical methods [79]. The former reaction is faster than the symmetric chlorine exchange by three orders of magnitude, and, owing to asymmetry, reactants and products are easily distinguishable. Viggiano *et al.* [12] investigated the $Cl^- + CH_3Br$ reaction as a function of ion–neutral average center of mass kinetic energy, finding that an increase of CH_3Br temperature does not increase the thermal rate constant. In contrast to results from a 2D quantum scattering study with a coupled–cluster PES [96], activation of the bond being broken does not seem to be necessary. Graul and Bowers [103, 104] found that the translational energy distribution of the products Br^- and CH_3Cl is much smaller than the prediction by phase-space theory; consequently, the products are vibrationally excited. Reaction cross sections and product velocity distributions for the $Cl^- + CH_3Br$ reaction as a function of collision energy in the range 0.06-24.0 eV were measured by Angel and Ervin [18]. Ineffectivity of the S_N2 reaction compared with predictions from phase space and ion–dipole capture theory was found.

4.2.3 Results

Potential and Surface Eigenstates

One-dimensional cuts $V(\delta)$ through the PES for fixed values of the hyperradius ρ are shown in Fig. 4.16. Here, z and q are optimized with respect to energy. The curve for $\rho = 11$ a_0 includes the saddle point region. In the asymptotic region, here at 34 a_0, the well at $\delta \approx 5°$ (35°) belongs to the reactants (products). For short hyperradii, the well depths of the two channels do hardly differ, and for very short values of ρ, there is only a single well in the potential cut.

The energy levels of the asymptotic reactant and product states (calculated in the last sector, $\rho = 33.91$ a_0) up to the maximum total energy considered in this work are collected in table 4.2. The wavenumbers and quantum numbers of the reactants are primed to distinguish them from the corresponding values of the products. The anharmonic vibrational frequencies of the fundamental transitions can be compared with the experimental values [105] (in parentheses), showing good agreement: CH_3Cl: $v_1 = 3045$ (2966) cm^{-1}, $v_2 = 1376$ (1355) cm^{-1} and $v_3 = 719$ (732) cm^{-1}; CH_3Br:
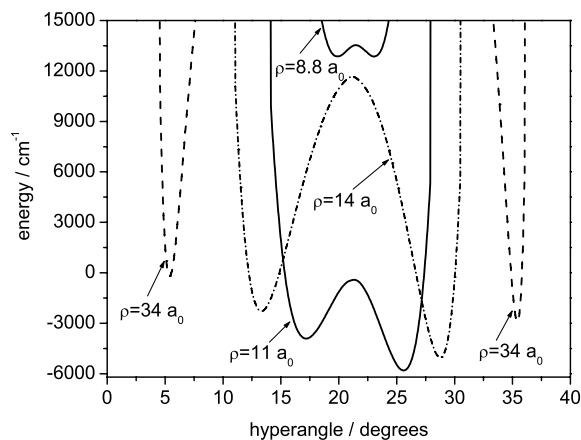
Figure 4.16: Potential cuts along the hyperangle δ for different values of the hyperradius ρ. The energy is optimized with respect to z and q.

$v_1' = 3053$ (2972) cm^{-1}, $v_2' = 1321$ (1305) cm^{-1} and $v_3' = 600$ (611) cm^{-1}. A more detailed discussion is provided in Refs. [79] (CH$_3$Cl) and [102] (CH$_3$Br). Up to the entrance channel level $(0,1,0)$ the asymptotic states are relatively isolated. For higher excitations, however, many reactant states i energetically come close to product states f. Many of these pairs include v_1 product excitation, e.g. $i/f = (0,0,3)/(1,1,0)$, $(0,1,2)/(1,1,1)$, $(0,2,1)/(1,1,2)$ and $(0,3,0)/(1,1,3)$. There are initial states highly excited in v_3' that are near–degenerate with product states: $i/f = (0,0,5)/(0,1,6)$, $(0,0,8)$ and $(0,0,6)/(0,4,1)$, $(0,3,3)$.

Fig. 4.17 graphically displays the hyperspherical adiabatic curves, $\varepsilon_n(\rho)$, in the range from 9 a_0 to 19 a_0 (a) and an enlargement for 10 $a_0 < \rho < 15$ a_0 (b). Full lines belong to asymptotic exit channel states while dotted curves correspond to entrance channel states. Clearly, the lowest curves belong to the exit channel. The reactivity can be traced back to vibrationally non–adiabatic transitions between the $\varepsilon_n(\rho)$ curves. Fig. 4.17(b) shows many multiple avoided crossings that mediate the reaction. Due to the strong mixing, it is not possible to assign the complete adiabatic curves to one particular channel. Only in the asymptotic region, this assignment can be made. The exit channel shows a clustering of asymptotic states due to the near–resonance $2v_3 \approx v_2$ [79].

Resonance states can be regarded as bound states in isolated diabatic 1D potential energy curves. The coupling to states in other potentials leads to decay if the formerly "bound" state is now located in the energetic continuum, i.e. above the asymptotic energy of a particular channel.

Table 4.2:   Assignments of quantum numbers $(v_1^{(')}, v_2^{(')}, v_3^{(')})$ to the initial and final states of CH_3Br and CH_3Cl, respectively.   Here, $v_1^{(')}$, $v_2^{(')}$ and $v_3^{(')}$ denote the C–H stretching, CH_3 umbrella bending and carbon–halogen stretching vibrations. Primed quantities refer to the reactants (CH_3Br). Energies $E - E_{000}^{Cl}$ (in cm^{-1}) are given with respect to the vibrational ground state of CH_3Cl, E_{000}^{Cl}, and for reactant states additionally with respect to the zero–point energy level of CH_3Br, E_{000}^{Br}.

(v_1, v_2, v_3)	(v_1', v_2', v_3')	$E - E_{000}^{Cl}$	$E - E_{000}^{Br}$	(v_1, v_2, v_3)	(v_1', v_2', v_3')	$E - E_{000}^{Cl}$	$E - E_{000}^{Br}$
(0,0,0)		0.0			(0,0,4)	4986.3	2364.4
(0,0,1)		718.9			(0,1,2)	5126.7	2504.8
(0,1,0)		1376.3		(1,1,1)		5135.8	
(0,0,2)		1431.5		(1,0,3)		5186.5	
(0,1,1)		2087.5			(0,2,0)	5252.8	2630.9
(0,0,3)		2137.5		(0,4,0)		5428.7	
	(0,0,0)	2621.9	0.0	(0,3,2)		5471.9	
(0,2,0)		2738.4		(0,2,4)		5501.1	
(0,1,2)		2791.4		(0,1,6)		5535.5	
(0,0,4)		2837.1			(0,0,5)	5562.0	2940.1
(1,0,0)		3045.0		(0,0,8)		5577.9	
	(0,0,1)	3222.0	600.0		(1,0,0)	5674.8	3052.9
(0,2,1)		3442.4			(0,1,3)	5709.7	3087.8
(0,1,3)		3487.8		(1,2,0)		5786.5	
(0,0,5)		3530.5		(1,1,2)		5839.8	
(1,0,1)		3765.0			(0,2,1)	5842.3	3220.4
	(0,0,2)	3816.1	1194.2	(1,0,4)		5887.7	
	(0,1,0)	3942.6	1320.6	(2,0,0)		6056.3	
(0,3,1)		4088.7		(0,4,1)		6118.0	
(0,2,2)		4137.9			(0,0,6)	6131.4	3509.4
(0,1,4)		4176.7		(0,3,3)		6145.3	
(0,0,6)		4218.0		(0,2,5)		6171.8	
	(0,0,3)	4404.3	1782.4	(0,1,7)		6207.6	
(1,1,0)		4424.6		(0,0,9)		6251.1	
(1,0,2)		4478.9			(1,0,1)	6274.3	3652.4
	(0,1,1)	4537.6	1915.7		(0,1,4)	6286.4	3664.5
(0,3,1)		4785.6			(0,2,2)	6425.9	3804.0
(0,2,3)		4824.1		(1,2,1)		6490.0	
(0,1,5)		4858.9		(1,1,3)		6536.5	
(0,0,7)		4900.3			(0,3,0)	6552.2	3930.3

Reaction Probabilities

In calculations on lifetimes of resonance states in the Cl^- + CH_3Br reaction [102], i.e. for energies above the reactant zero–point level, very long-lived states have been found. They live up to several microseconds, corresponding to widths down to the order of 10^{-7} cm^{-1}. Thus, the energetic grid in the scattering calculations had to be relatively fine to resolve as many narrow resonances as possible.

A broad overview of the resonance structure is shown in Fig. 4.18. Here, the reaction probability from the highest open vibrational reactant state (v_1', v_2', v_3') at each energy into the equivalent state $(v_1 = v_1', v_2 = v_2', v_3 = v_3')$ in the product molecule is given. This explains the coarse structure shown in the figure which gives an overview impression of the reaction probabilities. All calculated $P(E)$ data follow this strongly oscillating pattern.
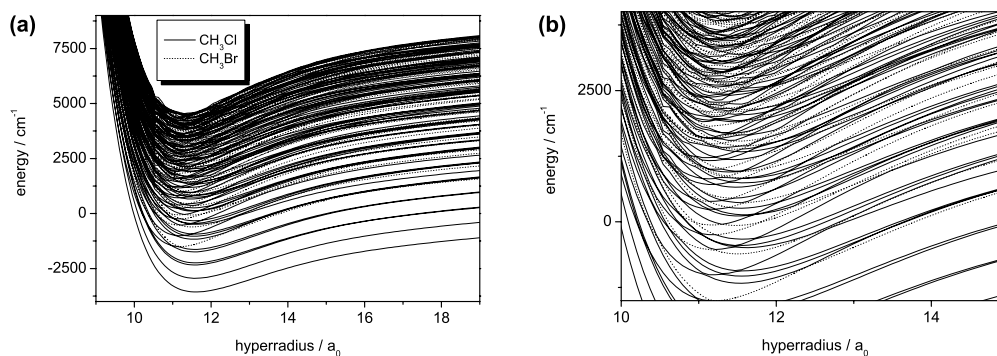
Figure 4.17: Hyperspherical adiabatic curves. Shown are all $N_{ch} = 150$ curves whereof 96 belong to asymptotic exit channel states while 54 are pertinent to entrance channel states. The classical asymptotic limit of the PES is set to zero. While Fig. 3(a) gives the full energy range covered by our calculations, Fig. 3(b) displays only a small part including numerous avoided crossings between the hyperspherical adiabatic curves that mediate the non–adiabatic transitions between the different vibrational states.
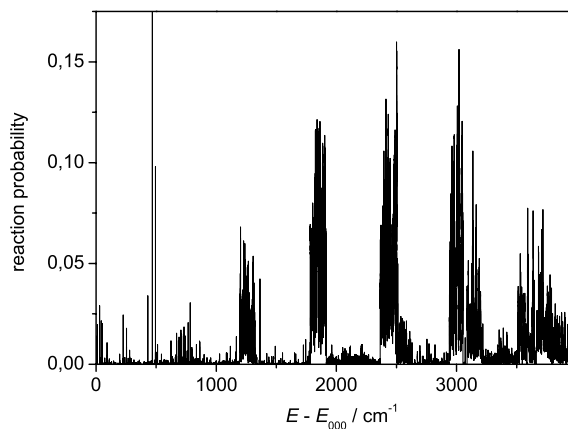
Figure 4.18: The reaction probability $P(E)$ as a function of energy E is strongly dominated by scattering resonances. Shown are the diagonal state–to–state reaction probabilities $P_{i,f}(E)$, i.e. $v'_i = v_i$, $i = 1,2,3$ for the highest reactant channel (v'_1, v'_2, v'_3) at energy E.

To facilitate the comparison between different initial vibrational states, the $P(E)$ curves are averaged over 80 cm^{-1} so that each point is the arithmetic mean of all probabilities in the interval $[E - \Delta, E + \Delta]$ with $\Delta = 40$ cm^{-1}. All initial–state selected $P(E)$ curves shown in the following and all product distributions (which are related to state–to–state reaction probabilities $P_{i,f}(E)$) are averaged according to this procedure.

- The exothermic reaction $Cl^- + CH_3Br$

Fig. 4.19(a) shows the initial–state selected reaction probabilities summed over all product states as a function of initial translational energy,

$$P_i(E) = \sum_f P_{i,f}(E) = \sum_f |S_{i,f}|^2. \tag{4.5}$$

The energetic ranges of the curves are different because the data are not shown as functions of total energy; to recover the probabilities as functions of total energy, the individual curves must be shifted by the corresponding energy levels quoted in table 4.2. There is a clear distinction between three groups of curves. The first group contains initial vibrational states without excitation in the C–Br bond. Here, $P(E)$ is far below 0.1. The second group contains those initial states with one quantum of internal energy in the C–Br stretching mode v_3'; here, the reaction probabilities are considerably increased. Finally, after a clear gap, the third group contains $P(E)$ curves corresponding to initial vibrational states with $v_3' \geq 2$. These curves are found in the probability interval from 0.5 to 0.8 with a tendency to saturation at the latter value which is still below the maximum value of 1.0 that should be reached for a classical barrierless reaction.

Fig. 4.19(b) displays the probability for reaction out of the vibrational ground state which rises exponentially with a pronounced coarse structure. Exciting the umbrella bending mode v_2' in the reactant CH_3Br yields a significant increase of $P(E)$. Interestingly, excitation of the high–frequency C–H stretching mode v_1' shows quantitatively a very similar effect. This observation leads to the conclusion that both totally symmetric modes of the methyl group have a comparable influence on the reactivity in the $Cl^- + CH_3Br$ reaction. Putting two quanta in the umbrella bending mode results in an almost linear increase of $P(E)$ compared to excitation $v_2' = 1$. It should be pointed out that the coarse shape of all curves displayed in Fig. 4.19(b) is quite similar exhibiting a dip at about 750 cm^{-1} of translational energy.

The well–known 'spectator' mode concept states that a bond which is not directly involved in the reaction can be treated adiabatically and does not show a significant influence on the reactivity. The high–frequency C–H stretch is often regarded as a prototypical example of a spectator mode. The mode is present both in reactants and in products and, owing to its large frequency, the coupling to the other modes is expected to be weak. Surprisingly, despite the fairly small influence of these 'spectator' modes on thermal reactions (due to their low population), they should be included if one aims at a detailed understanding of the underlying dynamics: From the present calculations,
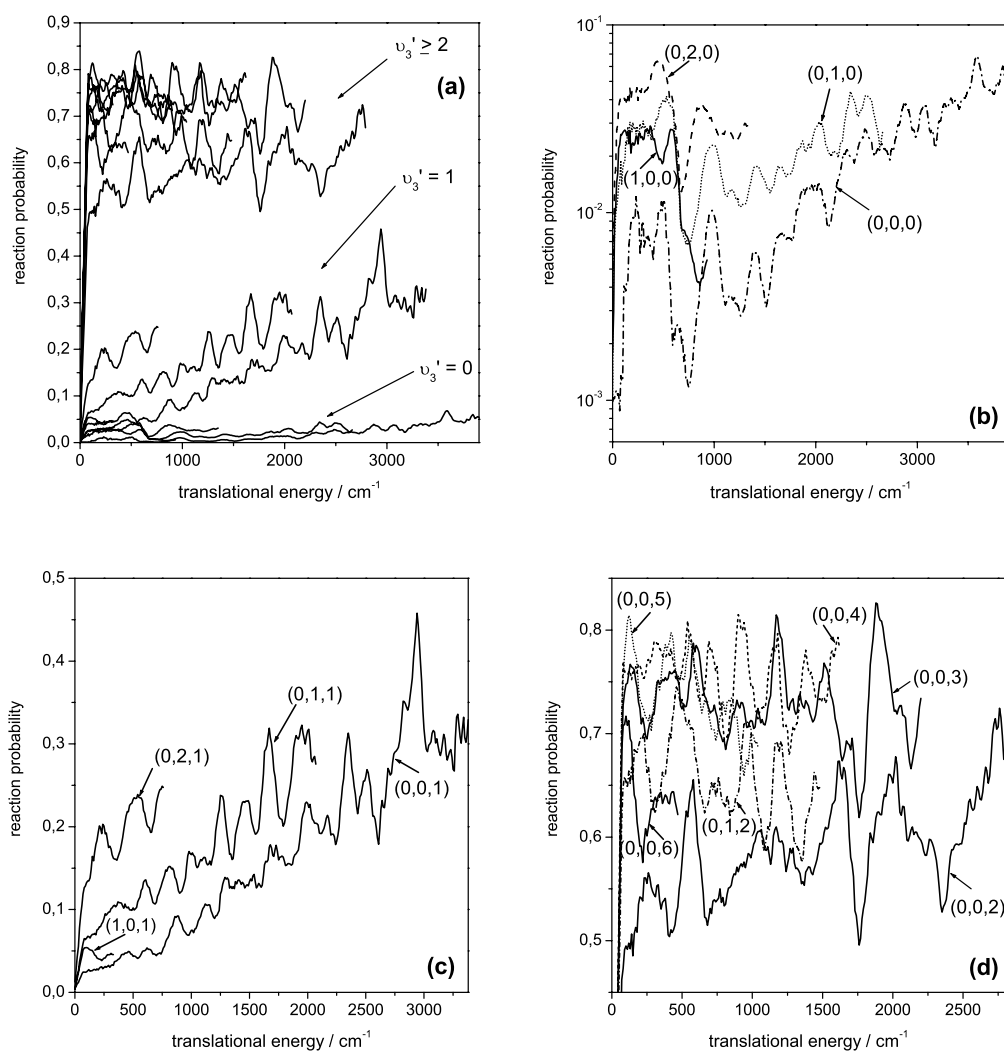
Figure 4.19: Initial state–selected probabilities $P_i(E)$ for the exothermic reaction Cl^- + CH_3Br $(v_1', v_2', v_3') \rightarrow ClCH_3 + Br^-$ as functions of translational energy E_{trans}. The data is smoothed over intervals of 80 cm^{-1}. $P_{i,f}(E)$ is summed over all accessible product channels f. (a) Overview, (b) without excitation in v_3', (c) one quantum in v_3', (d) two or more quanta in v_3'.

there is clear evidence that both the umbrella mode and the symmetric C–H stretch do not behave as spectators. This conclusion is further supported by independent calculations on the decay of individual resonance states [102] employing the same (real part of the) Hamiltonian and the same potential. By analysis of a large set of resonances with four assigned quantum numbers, it could be shown that excitation of the higher–frequency modes leads to a strong decrease of the resonance lifetimes that contradicts the spectator mode concept. The latter would expect that the linewidths of the resonances are only very slightly changed by exciting the umbrella or C–H stretching mode.

As can be seen from Fig. 4.19(c), putting energy into the C–Br bond to be broken considerably increases the reactivity. When additionally one quantum is put in the umbrella bend v_2', the reaction probability rises more strongly than for pure excitation of the bending mode (see Fig. 4.19(b)), an effect that becomes even more pronounced for initial vibrational state $(0, 2, 1)$ compared to $(0, 2, 0)$. This emphasizes the role of a cooperative effect in vibrational excitation in the reactant molecule CH_3Br. The simultaneous excitation of v_2' and v_3' corresponds to the classical transitional mode (with imaginary vibrational frequency) at the saddle point on the PES: During the reaction, the C–Br mode is broken and the methyl group undergoes inversion. The same effect has already been observed in the thermoneutral reaction $Cl^- + CH_3Cl'$ [79]. On the other hand, simultaneous excitation of the C–H stretch, v_1', and the C–Br stretch v_3' has a much smaller effect on the reactivity, in particular when compared to the significance of pure excitation in v_1' (see Fig. 4.19(b); only a short curve for initial excitation $(1, 0, 1)$ can be shown due to the fact that this initial vibrational state is already very high in energy). This additionally underlines the synergic effect exhibited by simultaneously exciting umbrella bend and C–Br stretch.

The influence of exciting the C–Br stretch with two or more quanta is shown in Fig. 4.19(d). As expected from chemical intuition, an increase of $P_m(E)$ is found up to state $(0, 0, 3)$, but then a saturation is observed and the curve for reactant state $(0, 0, 6)$ exhibits a lower reaction probability than in the case of lower excitation in v_3'. This effect can be rationalized by the fact that higher vibrational excitation corresponds to larger expectation values of the C–Br bond distance. Thus, it may be the case that the bond is 'overstretched' with respect to the optimal saddle point geometry which should be attained by the system to overcome the barrier. Distortions from that geometry raise the potential energy and therefore, an optimum value for the number of quanta in v_3' exists. The same finding was made by Schmatz and Clary [31] who report reaction cross sections (summed over all product states) from 2D calculations on a PES resulting from the 4D PES used in this work by minimizing the energy with respect to q and z. For low translational energy, the cumulative reaction probability for initial excitation $(0, 1, 2)$ is considerably higher than the corresponding one for $(0, 0, 2)$. A similar behavior is found for initial states $(0, 0, 0)$ and $(0, 1, 0)$. According to Fig. 4.19(d), saturation of the reaction probabilities is reached at $P = 0.8$.

Figs. 4.20(a)–(f) graphically display the product distributions for six selected initial vibrational states of CH_3Br. They are obtained as the normalized state–to–state reac-

tion probabilities, $P_{i,f}(E)/P_i(E)$. Absolute state–to–state reaction probabilities can be obtained by multiplying the data from Figs. 4.19 with the percentage amounts of Figs. 4.20. Note that all product states with a negligible population are not shown in the figures.

At very low translational energies, reaction out of the CH_3Br ground state (see Fig. 4.20(a)) is most likely to end in product state $(0,0,3)$ whose contribution decreases to ca. 20 % and then on average remains constant. When the $(0,1,2)$ product channel opens, it becomes dominant, but for higher translational energies decreases to smaller values. The $(0,0,2)$ CH_3Cl state is populated fairly low at small E_{trans} but for higher collision energies the percentage amount of this product channel increases to more than 30 %. After opening of the $(0,0,4)$ product channel, its population rises to more than 25 %, but decreases for higher energies. In summary, for reaction out of CH_3Br in its vibrational ground state, products with the C–Cl stretch excited by 2–4 quanta are formed. In agreement with the observation by Graul and Bowers [103, 104], the products are vibrationally hot.

Putting one quantum of energy in the bond being broken, i.e. the C–Br stretching mode (Fig. 4.20(b)), results in a very similar picture. The $(0,0,3)$ product curve starts at ca. 20 % and slightly rises for larger E_{trans}. The $(0,0,2)$ channel starts at ca. 5 % and strongly increases, with pronounced oscillations, up to 40 % in the energy regime considered. The $(0,0,4)$ state is initially relative important, while it becomes less populated at higher energies. The combination level $(0,1,1)$ exhibits a contribution of almost constantly more than 10 %. As for reactant state $(0,0,0)$, the product channel $(0,1,2)$ is initially most important, but becomes much less significant at larger translational energies. Note that all product levels shown in Fig. 4.20(b) are energetically located below the reactant state. The product channel $(0,0,5)$ is insignificant.

For initially one quantum in the umbrella bending vibration ν_2', (Fig. 4.20(c)), product channels with pure ν_2' excitation are most likely formed only at lower translational energies. Product states $(0,0,3)$ and $(0,0,4)$ are on average almost equally probable while showing stronger oscillations. The same observation is made for the $(0,0,5)$ state whose average contribution is considerably higher, however. The CH_3Cl combination modes $(0,1,2)$, $(0,1,3)$ and $(0,1,4)$ show large contributions at small E_{trans}, but then decay fast to values below 5 %. In summary, C–Cl stretching excitation in the products is strongly favored. For small translational energies, the umbrella mode behaves adiabatically, i.e. the energy in this mode is conserved and a considerable part of the collision energy is transformed into vibrational energy (T $\rightarrow$ V process). For large translational energies, the energy originally stored in ν_2' is almost completely redistributed.

For reactants in state $(0,1,1)$ (Fig. 4.20(d)), overall a similar behavior is observed. Product C–Cl stretching states are strongly populated, in particular state $(0,0,5)$ with almost up to 30 %, but also state $(0,0,4)$ and to much less extend $(0,0,3)$. Product combination levels with $v_2 = 1$ are initially quite significant $((0,1,3)$, $(0,1,4)$ and $(0,1,5)$ start at about 10, 15 and 8 %, respectively), but then show a decreasing tendency. Surprisingly, product channel $(0,2,1)$ starts at more than 10 % and then further
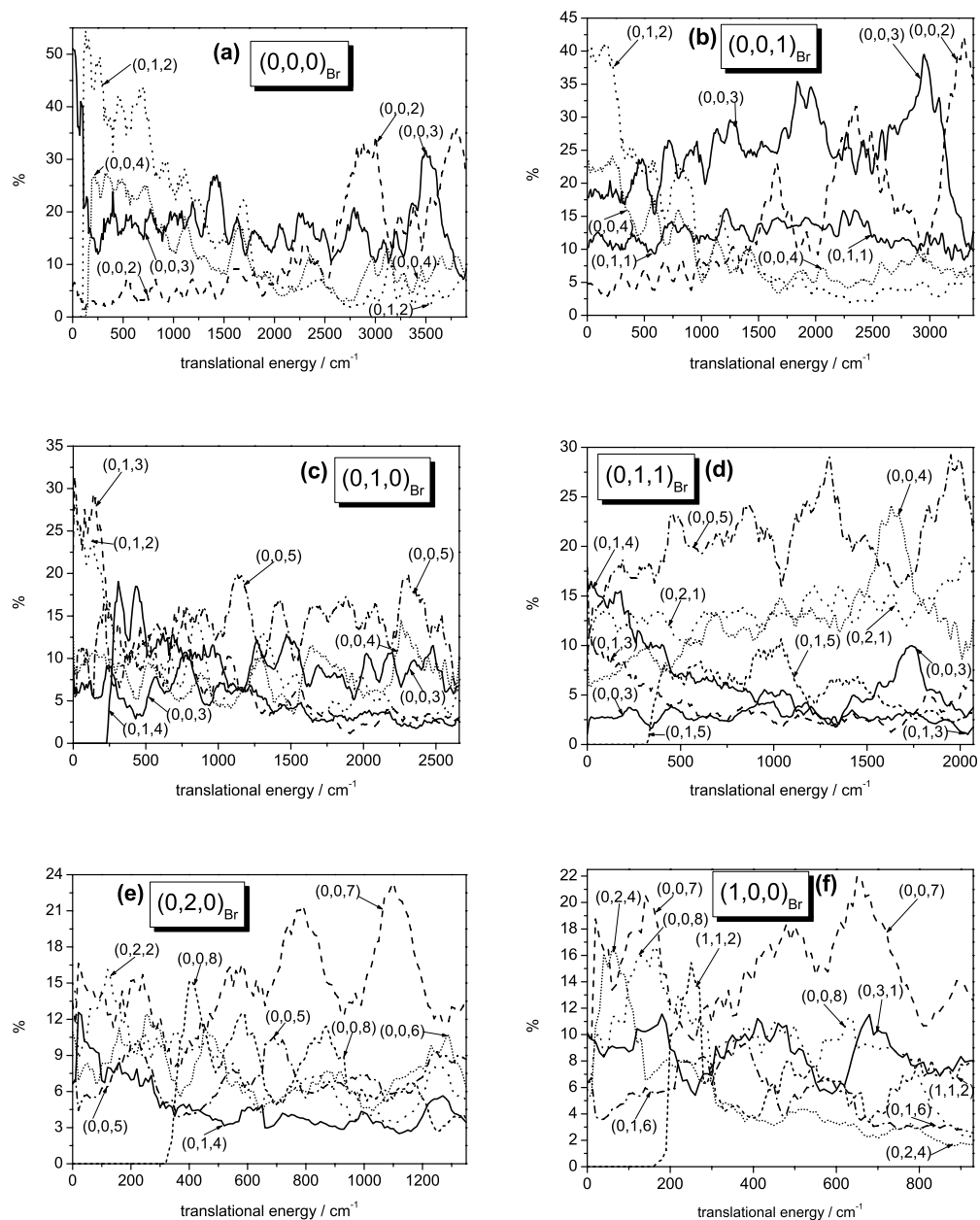
Figure 4.20: Product distribution for $Cl^- + CH_3Br\ (v'_1, v'_2, v'_3) \rightarrow ClCH_3\ (v_1, v_2, v_3) + Br^-$ for CH_3Br being initially in vibrational states $(0,0,0)$, $(0,0,1)$, $(0,1,0)$, $(0,1,1)$, $(0,2,0)$ and $(1,0,0)$. The data is smoothed over intervals of $80\ cm^{-1}$.

increases. With $\Delta v_2 = +1$ this is a T $\rightarrow$ V process. This points out that the umbrella mode clearly is not a spectator mode and that the combination mode exhibits a particularly high reactivity. The $\Delta v_2 = +1$ transition is possible only when additionally the C–Br mode is excited.

Initially two quanta in the umbrella mode, $(0,2,0)$ (Fig. 4.20(e)), again favor the product channels $(0,0,n)$ close in energy. Most significant is state $(0,0,7)$ starting at ca. 15 % and then increasing with strong oscillations. The contribution of channel $(0,0,8)$ rises – after its opening – to almost 15 %, but decreases for higher E_{trans}. Product channels $(0,0,5)$ and $(0,0,6)$ show a relative similar behavior, but are less important compared to state $(0,0,7)$. The isoenergetic product channels $(0,1,4)$ and $(0,2,2)$ initially show significant contributions which for higher energies become less important, in agreement with initial excitation $(0,1,0)$. Overall, the product distribution for $(0,2,0)$ is shifted by two quanta in v_3 compared to initial state $(0,1,0)$. This is not surprising because for CH_3Cl we have $v_2 \approx 2v_3$. Thus, the translational energy distribution is not changed.

CH_3Br initially excited with one quantum in the symmetric C–H stretching mode v_1' (Fig. 4.20(f)) results in the dominant product channel $(0,0,7)$ and a significant contribution of state $(0,0,8)$. The isoenergetic channels $(0,1,6)$, $(0,2,4)$ and $(0,3,1)$ are also important. The only product state with energy stored in v_1 is $(1,1,2)$ that after its opening rises to 15 % and then decreases to on average about 6 %. As can be seen from Fig. 4.20(f), the probability to find products with the umbrella mode excited, in particular in combination with the C–Cl stretch, is high. This underlines the active role of this mode in the reaction.

- The endothermic reaction $Br^- + CH_3Cl$

Fig. 4.21 graphically displays the initial state–selected reaction probabilities for the reverse, endothermic reaction $Br^- + CH_3Cl\ (v_1, v_2, v_3) \rightarrow BrCH_3\ (v_1', v_2', v_3') + Cl^-$. Here, $P(E)$ is much smaller, and Fig. 4.21(a) is given with a logarithmic scale. It is relatively difficult to divide the curves into groups.

Fig. 4.21(b) contains the isolated $P(E)$ curve for reaction out of the vibrational ground state of CH_3Cl. Clearly, it is non–zero only when the total energy is larger than that of the first state at the product side. The reaction probability rises less than exponentially. Fig. 4.21(a) contains four other relatively low probability curves that all belong to initial vibrational states with $v_1 = 1$. Owing to the high frequency of this mode, the curves start at $E_{\text{trans}} = 0$. Excitation of v_1 increases the reactivity. This effect is enhanced by simultaneous excitation of the C–Cl stretch, v_3, and the umbrella bend, v_2. Note that putting one quantum of energy in the umbrella bending mode results in a similar but slightly larger reaction probability than one quantum in the mode corresponding to the bond that is broken. The C–H stretch cannot be considered as a spectator because the energy originally stored in this mode is used to overcome the large reaction barrier.

Fig. 4.21(c) gives the reaction probabilities for pure initial bending states $(0, v_2, 0)$ with $v_2 = 1, 2, 3$ and for the combined excitation of v_2 and v_3, $(0,1,1)$. Also shown is
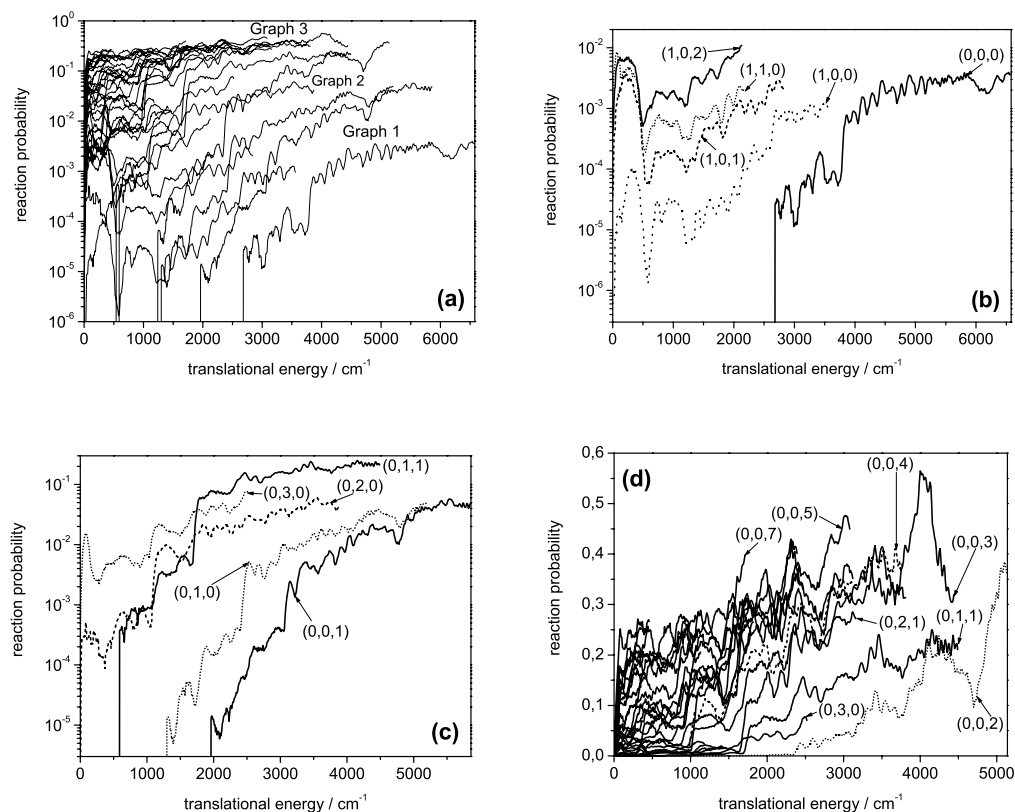
Figure 4.21: Initial state–selected probabilities $P_i(E)$ for the endothermic reaction $Br^- + CH_3Cl\ (v_1, v_2, v_3) \rightarrow BrCH_3 + Cl^-$ as functions of translational energy E_{trans}. The data is smoothed over intervals of 80 cm^{-1}. $P_{i,f}(E)$ is summed over all accessible product channels f. (a) Overview, (b) reaction out of the vibrational ground state and states with excitation $v_1' = 1$, (c) reaction out of states $(0,0,1)$, $(0,1,1)$ and $(0, v_2, 0)$, $v_2 = 1, 2, 3$, (d) higher excitation in v_3 and combination modes $(0, v_2, v_3)$; curves $(0,1,1)$ and $(0,3,0)$ are also shown for comparison.

the curve for initially one quantum in the C–Cl stretch, $(0,0,1)$, which, like $(0,0,0)$, increases not exponentially. The $(0,1,0)$ probability is larger than that for reaction out of the vibrational ground state, confirming that the umbrella mode cannot be treated as a spectator. A drastic increase is observed for the combination mode $(0,1,1)$ which has a larger probability than initial state $(0,0,2)$ (see Fig. 4.21(d)) and, for translational energies larger than ca. $1500\,\text{cm}^{-1}$, also than state $(0,3,0)$.

In Fig. 4.21(d), higher excitations in ν_3 are shown, along with simultaneous excitations in ν_2 and ν_3. Only a few states are explicitly labeled, the other curves are contained in the plot to demonstrate the convergence behavior. Initial states $(0,3,0)$ and $(0,1,1)$ (from Fig. 4.21(c)) are also contained in this figure; note that the scale is linear. There is a strong increase going from initial state $(0,2,0)$ to $(0,2,1)$ which is larger than the addition of the probabilities out of states $(0,2,0)$ and $(0,0,1)$.

The product distributions for a selection of initial vibrational states are reported in Figs. 4.22(a)–(f). Absolute state–to–state reaction probabilities can be obtained by multiplying the data from Figs. 4.21 with the percentage amounts of Figs. 4.22. Reaction out of the vibrational ground state of CH_3Cl (Fig. 4.22(a)) favors the highest available product state $(0,0,\nu_3')$ up to $\nu_3' = 2$. When channel $\nu_3' = 3$ opens, it is about equally populated as $(0,0,2)$. For higher translational energies, $(0,0,1)$ plays a dominant role. Overall, we observe a clear $T \to V$ process.

For initially one quantum in ν_3 (Fig. 4.22(b)), the product distribution is very similar. For high translational energies, however, the contribution of channel $(0,0,1)$ is increased and also $(0,0,2)$ becomes more important. A similar situation is encountered for initial state $(0,1,0)$ (Fig. 4.22(c)). Here, product state $(0,0,2)$ is clearly dominant. The contribution of the 'adiabatic' product state $(0,1,0)$ is vanishingly small. A comparable picture is obtained for the initial combination mode $(0,1,1)$ (Fig. 4.22(d)). Here, the product state $(0,0,2)$ is even more important. Product states with up to five quanta in the C–Br stretching mode play a significant role.

Excitation of the high–frequency C–H stretch ν_1 (Fig. 4.22(e)) yields a slightly more complicated picture for translational energies larger than $1500\,\text{cm}^{-1}$. We observe additional significant product channels $(0,1,\nu_3')$ with $\nu_3' = 1-4$ so that a vibrational redistribution $\nu_1 \to \nu_2'$ is not only possible but also very likely. However, the quantum in ν_1 is not conserved, clearly contradicting the spectator hypothesis.

For the endothermic $Br^- + CH_3Cl$ reaction, results for initial state $(2,0,0)$ for up to more than $500\,\text{cm}^{-1}$ translational energy have been obtained (Fig. 4.22(f)). Again, product states that are close in energy with the initial state are populated: $(0,0,\nu_3')$ with $\nu_3' = 3,\ldots,6$, $(0,1,\nu_3')$ with $\nu_3' = 2,3,4$ as well as $(0,2,1)$ and $(0,2,2)$. The two quanta in ν_1 are not conserved, not even partly, which would result in $\nu_1' = 1$. We point out that this result again clearly contradicts the well–established spectator hypothesis for the high–frequency C–H stretch. This conclusion is not limited to the special case of S_N2 reactions, but should have far–reaching consequences on all systems where similar "spectator" modes are present.

It is remarkable that the product distributions for the endothermic reaction are very similar to each other. The same observation was made for the $Cl^- + CH_3Cl$ system [79]
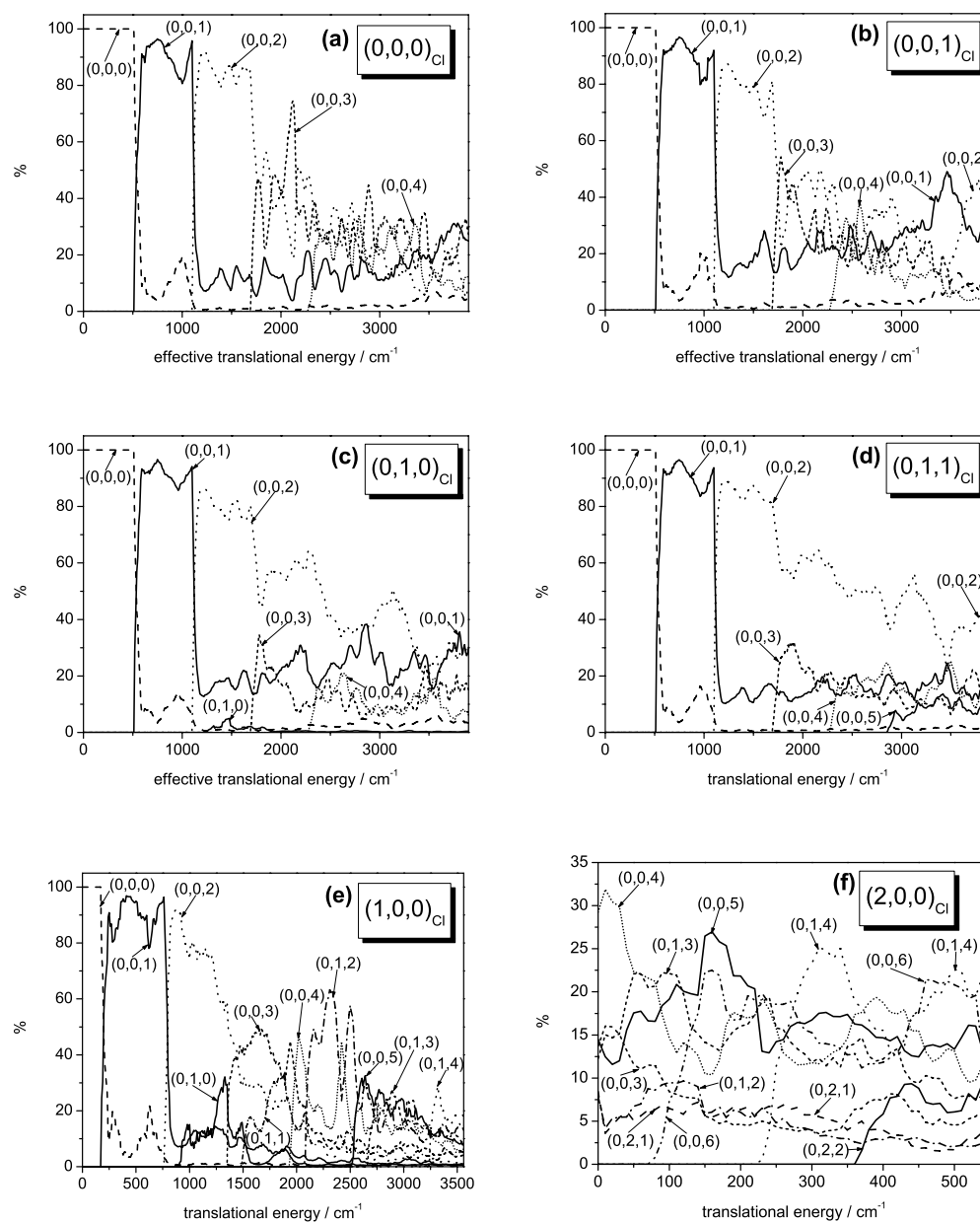
Figure 4.22: Product distributions for $Br^- + CH_3Cl$ $(v_1, v_2, v_3) \rightarrow BrCH_3$ (v'_1, v'_2, v'_3) + Cl^- in vibrational states $(0,0,0)$, $(0,0,1)$, $(0,1,0)$, $(0,1,1)$, $(1,0,0)$ and $(2,0,0)$. The data is smoothed over intervals of 80 cm^{-1}. The effective translational energy denotes that part of E_{trans} that can be converted into product internal energy while the remaining part compensates the endothermicity.
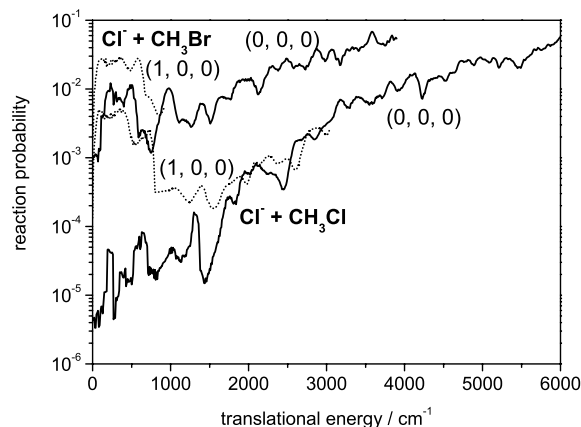
Figure 4.23: Comparison between reactions $Cl^- + CH_3Y \, (v_1, v_2, v_3) \rightarrow ClCH_3 + Y^-$ with Y = Cl and Br. The initial quantum states of the methyl halide molecule are $(0,0,0)$ and $(1,0,0)$.

and can be rationalized by the long lifetimes of the resonance states. Once formed, the state "looses its memory" and decays independently of its origin. For higher–lying resonance levels, in the region of increasing densities of states, the product distributions are more complicated. This statement is obviously also valid for the exothermic reaction $Cl^- + CH_3Br$ with the high–lying product states.

Comparison with the Thermoneutral Reaction $Cl^- + CH_3Cl'$

In Fig. 4.23, reactions of a chloride anion with either CH_3Cl and CH_3Br, both in their vibrational ground state, are compared. Also shown in this figure are the reaction probabilities for initial excitation of the symmetric C–H stretching modes in CH_3Cl and CH_3Br, respectively. For CH_3Br, the reaction probability out of the vibrational ground state is two orders of magnitude larger for small translational energies and one order of magnitude at $E_{trans} = 3500 \, cm^{-1}$. Both $P(E)$ curves for the vibrational ground state on average follow exponential laws, $P(E_{trans}) = Ae^{\alpha E_{trans}}$ with $A_{CH_3Cl} = 1.3 \cdot 10^{-5}$, $A_{CH_3Br} = 2.3 \cdot 10^{-3}$, $\alpha_{CH_3Cl} = 1.55 \cdot 10^{-3} \, 1/cm^{-1}$ and $\alpha_{CH_3Br} = 0.82 \cdot 10^{-3} \, 1/cm^{-1}$.

Putting one quantum in the symmetric C–H stretching mode increases $P(E)$ for CH_3Cl at low E_{trans} by about two orders of magnitude, while this mode becomes a spectator for energies higher than ca. 1700 cm^{-1}. For CH_3Br, the corresponding increase for small E_{trans} is only one order of magnitude and the spectator mode behavior sets in already at ca. 900 cm^{-1}. Obviously, the missing net barrier in the $Cl^- + CH_3Br$ potential is the reason for the different behavior. The barrier in the $Cl^- + CH_3Cl$ potential renders the C–H mode more important as an energy reservoir for surmounting the barrier. The difference between the E_{trans} values where the spectator–like behavior
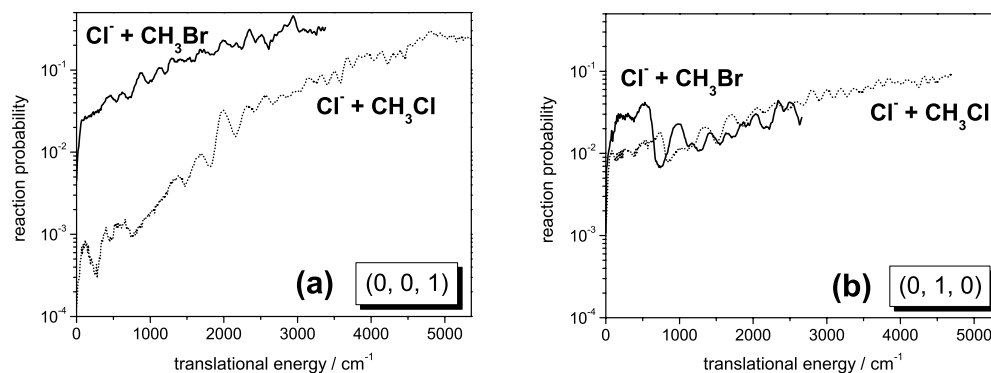
Figure 4.24: Comparison between reactions $Cl^- + CH_3Y$ $(v_1, v_2, v_3) \rightarrow ClCH_3 + Y^-$ with Y = Cl and Br. The initial quantum states of the methyl halide molecule are $(0, 0, 1)$ and $(0, 1, 0)$.

sets in is roughly the value of the potential barrier in the chlorine exchange reaction.

Fig. 4.24 compares $P(E)$ for the two reactions with either one quantum in v_3 or v_2. Exiting the C–Hal stretch yields a similar relative behavior as for reaction out of the vibrational ground state. For excitation of the umbrella bending mode with one quantum, however, the probabilities of the two reactions are very similar to each other. As discussed for the C–H stretch, also the umbrella mode plays a different role in the barrierless reaction $Cl^- + CH_3Br$ and the chlorine exchange reaction with a net barrier. In the latter reaction, the probability is strongly increased because the energy in v_2 can be used to overcome the barrier. In the former case, however, the enhancement of the reaction is less pronounced, apart from the very low translational energy regime. The similarity of the two curves for initial excitation $(0, 1, 0)$ is thus accidental.

Resonance Linewidths

Fig. 4.25 graphically displays the resonance widths distribution as a function of the excess energy which is defined as $E - E_{000}^{CH_3Br}$ with E_{000} being the zero–point energy level of the product. The linewidths are directly proportional to the decay constants k of the resonances, $\Gamma = \hbar k$. Depending on the nature of the resonance, the decay is related to one or more channels: Dissociation of the exit channel, dissociation of the entrance channel and isomerization.

The resonance widths Γ from our scattering calculations (open circles in Fig. 4.25) have been obtained from fitting the reaction probability to Lorentz–type profiles,

$$P(E) = P_{\max} \frac{\Gamma^2}{4(E - E_{\text{res}})^2 + \Gamma^2} \tag{4.6}$$

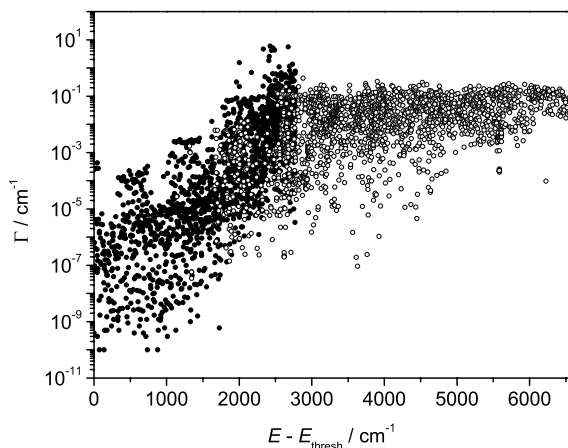employing a fitting procedure similar to that described in Ref. [79]. Widths are shown

Figure 4.25: Resonance width distribution (open circles) as function of excess energy $E - E_{\text{thresh}}$ where E_{thresh} is the vibrational ground state of CH_3Cl, E_{000}^{Cl}. The data are compared with results from 4D filter diagonalization calculations [102] (full circles).

up to 0.2 cm^{-1}. The upper bound of the resonance width distribution is cut because the corresponding resonance heights are too low to be resolved. These broad and unassignable resonances are mostly fully delocalized over both potential wells and partly also the barrier region. By extracting the linewidths employing a fit to $P(E)$, wavefunctions are not obtained and thus, an assignment of the individual resonance states is not possible. However, product distributions of the individual resonances can be calculated. It could be shown in Ref. [79] for the $Cl^- + CH_3Cl$ system that the product distributions of the individual resonances are independent of the initial reactant state [79].

Fig. 4.25 also contains a comparison with recent filter diagonalization calculations [102] (full circles) which yield directly the poles in the complex energy plane, $E = E_{\text{res}} - \frac{i}{2}\Gamma$. Here, resonance wave functions could be obtained and the states were assigned four quantum numbers. Due to limitations of the size of the grid for representing the wave function, only the lower bound of the linewidths is well defined while the upper bound is not. The agreement between the two distributions in the overlap region is overall good. The two methods, quantum reactive scattering and filter diagonalization, are complementary in obtaining the resonance spectrum. The scattering calculations could be extended to even higher energies, but the resonances can hardly be resolved because their heights are too low.

The filter diagonalization treatment could be improved by employing a larger grid. However, for higher energies than shown in Fig. 4.25, the performance of such a calculation cannot be justified from an economical point of view because the gain of information is too low [102]. For higher excess energies, RRKM seems to fit well

while the performance of statistical theories for lower energies is only very poor [102].

The number of resonances obtained from the scattering calculation is much smaller than that resulting from filter diagonalization. For energies below the zero–point level of CH_3Br, only non–reactive processes $Cl^- + CH_3Br\ (v'_1, v'_2, v'_3) \rightarrow Cl^- + CH_3Br\ (v''_1, v''_2, v''_3)$ are possible. In particular, for low energies with just a few open channels, every possible process exhibits a high background probability, which renders the extraction of resonances more difficult. In addition, some of these seem to show a non–Lorentzian behavior. Below the energy of the $(0, 0, 1)$ state, only elastic scattering is possible so that resonances cannot be computed from the squared moduli of the $\mathbf{S}$–matrix elements.

4.2.4 Conclusions

(1) Time–independent quantum scattering calculations have been carried out on the exothermic S_N2 reaction $Cl^- + CH_3Br \rightarrow ClCH_3 + Br^-$ and the corresponding endothermic reverse reaction using hyperspherical coordinates describing the bonds being broken and formed. The two totally symmetric modes of the methyl group are included in the model. C_{3v} symmetry is conserved throughout the reaction.

(2) A variant of the Lanczos scheme with a modified partial reorthogonalization procedure was formulated and employed in the calculations.

(3) A narrow grid in the total energy was employed so that long living resonance states could be resolved. Resonances are extracted by fits to Lorentzian functions. The resonance widths distribution provides a continuation of the data obtained by previous filter diagonalization calculations. The agreement in the overlap region of the two data sets is good.

(4) While excitation of the umbrella bending mode already leads to a considerable enhancement of the reaction probability, its combination with vibrational excitation of the broken C–Br bond results in a strong synergic effect. This can be explained by the similarity of the combined excitation with the classical transitional normal mode. Combination of C–Br stretch and C–H stretch does not show such a cooperative effect.

(5) Exciting the high–frequency symmetric C–H stretching vibration has a non–negligible effect on the reaction probability. For larger translational energies, however, the reaction probability for this mode initially excited follows the expected spectator–like behavior. The spectator concept is also questionable with respect to the product distribution of states initially excited in the C–H stretch. Energy originally stored in this mode is released in other modes of the reaction products and by no means conserved. Thus, the C–H stretch does not behave adiabatically, contrary to chemical intuition and the expectation from the weak coupling to the other modes.

(6) In agreement with chemical intuition, excitation in the bond being broken leads to higher reaction probabilities. However, if this mode contains too many quanta, the expectation value of the bond becomes too large, i.e. the bond is overstretched and away from the optimal geometry in the saddle point structure: The potential energy rises and the reactivity decreases.

(7) Products are most likely formed in states with a high degree of excitation in the newly formed bond. The internal modes of the methyl group are much less important. Reactants with combined umbrella/C–Br stretch excitation (one quantum each) may yield products with two quanta in the umbrella mode. This high reactivity is only observed for the combined initial state, not for pure bending excitation.

(8) In the endothermic reverse reaction, excitation of the symmetric C–H stretching mode plays a very important role to overcome the barrier. Here, also initial states with two quanta in this mode could be considered. This energy is not even partly, i.e. yielding product states with one quantum in the C–H stretch, conserved, but is distributed among the other modes, strongly contradicting the spectator mode concept.

(9) A comparison between the reactions of Cl^- with CH_3Cl and CH_3Br, respectively, yields much higher probabilities for the latter case that are due to the absence of a net barrier. Excitation of the umbrella mode, however, results in comparable reaction probabilities. This effect is accidental and owing to the larger increase of reactivity in the chlorine exchange reaction where the energy may be used to overcome the barrier.

(10) For low initial excitations, the product distributions of the endothermic reverse reaction $Br^- + CH_3Cl$ are similar to each other and also similar to those of the identity reaction $Cl^- + CH_3Cl'$ because the very narrow resonances decay independently of their formation.

4.3   Rate Constants in the Cl–Cl Exchange Reaction

4.3.1   Abstract

Within the framework of reduced–dimensionality quantum scattering theory, we employ Bowman's adiabatic rotation approximation to describe reactive systems that have symmetric top geometries during the entire collision process. The results are compared with the approach of shifting the total energy by a characteristic rotational energy. Initial–state selected and total thermal rate constants have been computed for the complex–forming gas–phase reaction $Cl^- + CH_3Cl' \rightarrow ClCH_3 + Cl'^-$. At room temperature, we find a significant contribution from energetically high vibrational modes. The dependence of the cross sections on the different angular momenta is analyzed in detail and high total angular momenta are found to be of considerable importance. The influence of adiabatic azimuthal rotation on the rate constants turns out to be small compared to other effects. In addition, we use a new model to account for the asymmetric modes not explicitly contained in the scattering calculations. The difference to the only available experimental value confirms our conclusion that the Cl–C–Cl' bending modes are of major importance for this reaction.

4.3.2   Introduction

For reactions involving polyatomic molecules, the calculation of converged quantum mechanical reaction probabilities and cross sections is a formidable task. Usually, only a selection of the internal degrees of freedom of the system can be considered. Employing simple energy–shifting procedures [106, 107, 108, 109, 110, 111], the calculation of thermal rate constants is possible by including the degrees of freedom which are not explicitly taken into account. Moreover, the overall rotational motion is usually considered by shifting the reaction probability for total angular momentum $J = 0$ by the rotational energies of the transition state complex. This procedure could be applied quite successfully for reactions proceeding over a simple barrier while for complex–forming systems where the reaction probability is governed by sharp resonance features, J–shifting is highly questionable.

Using a more sophisticated approach in reduced–dimensionality quantum scattering calculations, approximate probabilities for $J \neq 0$ can be obtained applying the rotating line approximation (RLA) [88] that has been widely used in the past. This method is suitable for collinear reactions with a linear transition state complex and thus a single rotational constant. However, most reactions involving polyatomic molecules do not proceed via transition states with collinear alignment of all nuclei. E.g. for symmetric tops, the projection of $\mathbf{J}$ onto the molecular axis of symmetry has to be taken into account. In this work, we modify the adiabatic rotation approximation (ARA) advocated by Bowman [112, 113, 114] to a simplified version, the rotating (symmetric) top approximation (RTA) which can be applied in the calculation of rate constants from reduced–dimensionality quantum scattering data for true symmetric top geometries during the entire collision process (not only at the transition state).

Complex–forming bimolecular reactions are particularly challenging for studying the applicability of such dimensionality–reduced models because they have turned out to be very sensitive with respect to shifting procedures. Prototypes for this class of reactions are gas–phase S_N2 reactions [1, 2, 3, 4].

Total quantum mechanical cross sections $\sigma(E)$ can be obtained as weighted sums over reactions probabilities $P^J(E)$ for all possible total angular momenta J at given energy E. In a recent paper, Hennig and Schmatz [81] reported four–mode quantum scattering calculations on initial state–selected total cross sections and the rate constant for the above S_N2 reaction. Reducing the dimensionality, the system was studied under the restriction that C_{3v} symmetry is maintained throughout the course of reaction. It turned out that rotational effects must play a crucial role in the dynamics.

It is now important to see how the results change when the rotating top approximation is employed instead of the rotating line approximation. Furthermore, the rate constant calculation can be extended by inclusion of the high–frequency modes not yet incorporated in the model. Moreover, a thorough analysis of the convergence of rate constants with respect to total angular momentum quantum number J in the J–shifting and RTA approximations is very useful to understand the limitations of the models. Finally, a detailed analysis of the contributions of the various initial vibrational states
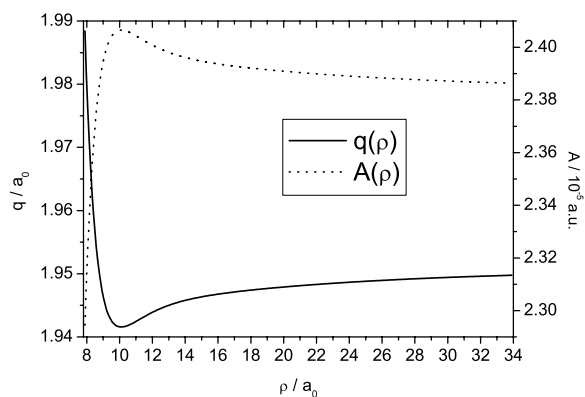
Figure 4.26: Changes of the orthogonal coordinate q and the symmetric top rotational constant A during the reaction (as a function of the hyperradius ρ).

to the rate constants at different temperatures should shed more light on the underlying dynamics.

4.3.3 Results

K–Dependent Reaction Cross Sections

Fig. 4.26 graphically displays the variations of the two most important structural parameters of the C_{3v} symmetric methyl group, the rotational constant $A(\rho)$ and $q(\rho)$, the distance between one hydrogen nucleus and the molecular axis of symmetry. For each value of the hyperradius ρ, the geometries were optimized with respect to energy. The formation of the complex results in a slight shortening of the C–H bond distance and consequently of q, whereas at even shorter distances the H–atoms are pushed away by the energetically unfavorably close Cl–atoms. The resulting ρ–dependent variation of A influences the final reaction cross sections via the changes of the available kinetic energy during the propagation.

The cumulative reaction cross sections summed over all final states and all possible values of the azimuthal quantum number K, $\sum_f \sum_K \sigma_{i,f}^K(E)$, are shown in Fig. 4.27. The small cross section sums for reaction out of the vibrational ground state, and those for initial excitation of the C–Cl and C–H stretching modes $((0,0,1)$ and $(1,0,0))$ as well the combination mode $(1,0,1)$ are displayed as a function of translational energy on a logarithmic scale in Fig. 4.27(a). Fig. 4.27(b) shows reaction cross section sums as a function of total energy when the vibration of the broken C–Cl bond is excited by one to eight quanta while Fig. 4.27(c) shows – for the same range of total energy – the cross section sums for initial excitation of the umbrella bending mode with one to four quanta. Finally, some cross section sums for initially excited combination modes
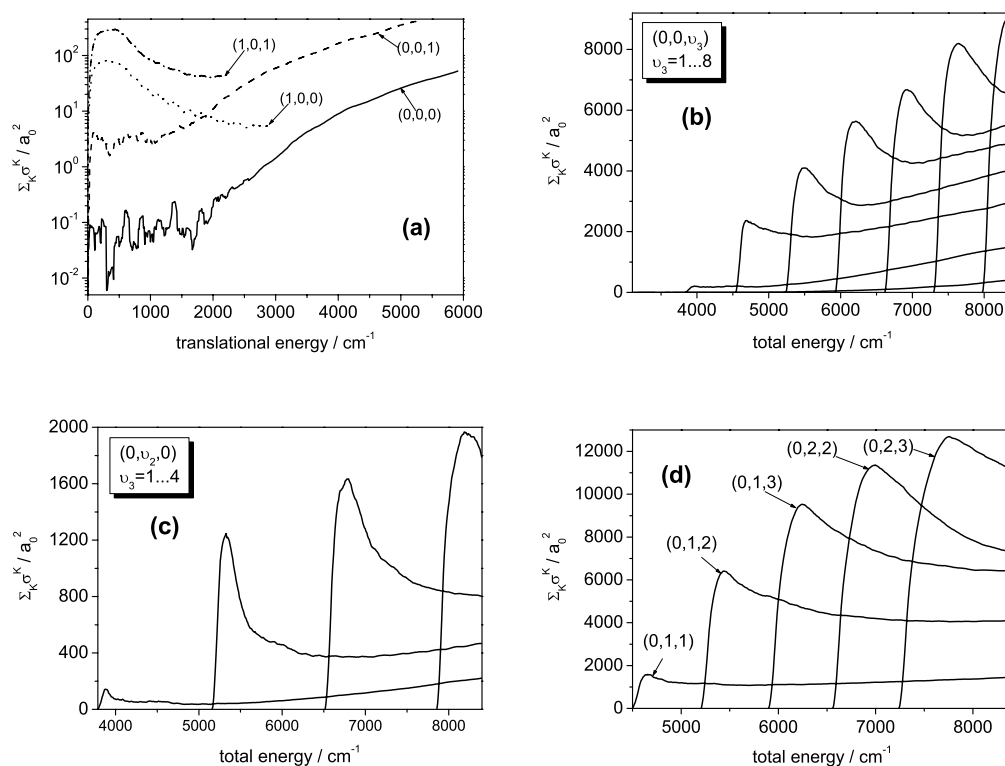
Figure 4.27: Initial–state selected total reaction cross sections for the reaction Cl^- + $CH_3Cl' \rightarrow ClCH_3 + Cl'^-$, summed over all accessible product channel and all values of the quantum number K. The data is averaged over intervals of 80 cm^{-1}. (a) As a function of translational energy, (b)–(d) as a function of total energy, counted from the classical asymptotic limit. (a) Reaction out of the reactant vibrational ground state and excited states $(0,0,1)$, $(0,1,0)$, $(1,0,0)$ and $(1,0,1)$. (b) Excitation of the C–Cl stretching mode v_3 with up to 8 quanta. (c) Excitation of the umbrella bending mode v_2 with up to 4 quanta. (d) Excitation of selected combination modes.
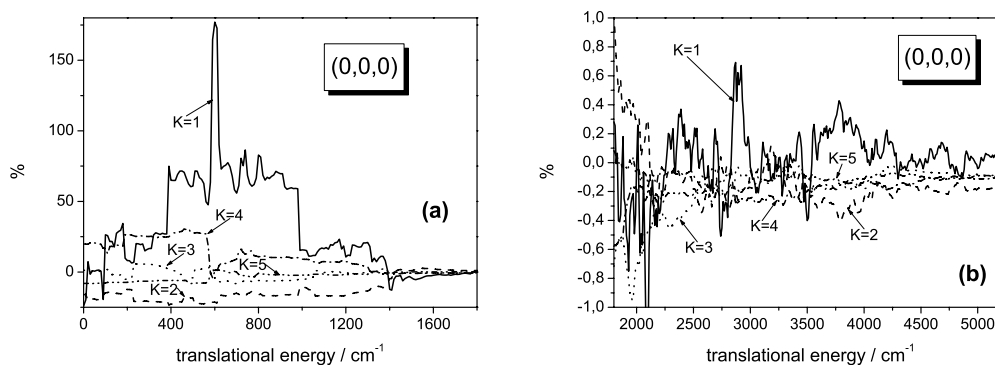
Figure 4.28:   Relative deviation of the state–selected cross section for initial state $(0,0,0)$ for azimuthal quantum number K from the one for $K-1$, weighted by the difference of the squares of the azimuthal quantum numbers (see the text). Each cross section is evaluated at the same translational energy E. The data is averaged over 600 cm^{-1}.

of C–Cl stretch and umbrella bend are displayed. The data can be compared to the $K=0$ cross sections from Ref. [81]. Some of the differences are simply caused by the different setting: In contrast to Ref. [81], the data in Fig. 4.27 has been averaged over intervals of 80 cm^{-1} resulting in less structure and acuteness. As we show cumulative cross sections summed over all K, the scale of the ordinates change by several orders of magnitude. However, some of the features in Fig. 4.27 could not be so easily predicted from our previous calculations: The envelope of the maxima becomes smoother; in Fig. 4.27(b), the increase of the maxima has become much more monotonous (dips at $v_3 = 3$, 5 and 7 are missing). Also in Fig. 4.27(d), some curves change order with respect to their maxima (e.g., $(0,2,2)$ and $(0,2,3)$). For large values of the total energy, nearly all curves show a deviation from the $1/k_i^2$–behavior which is explained by the presence of several of these prefactors due to the summation over different initial states (different K). Finally, in Fig. 4.27(a) the C–H-stretching mode does not reach the spectator mode regime valid for higher translational energies in contrast to Ref. [81] where such a spectator mode behavior can be observed within the displayed energy range. We attribute this to the contribution of cross sections with higher K and thus lower translational energy.

   In order to assess the influence of different values of K on the cross sections, we use the quantity

$$\frac{\sigma_i^K(E) - \sigma_i^{K-1}(E)}{(2K-1)\sigma_i^{K-1}(E)} \tag{4.7}$$

that gives the relative difference of these state–selected cross sections for K and $K-1$ weighted by the difference of the squares of the azimuthal quantum numbers. In
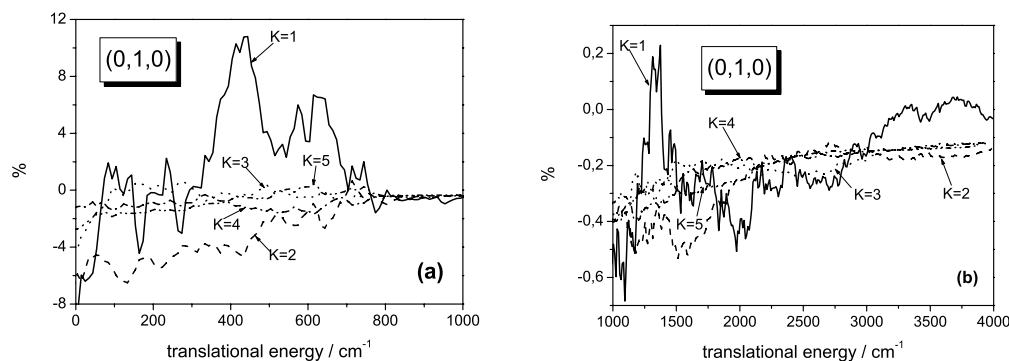
Figure 4.29: Same as Fig. (4.28) for initial vibrational state $(0, 1, 0)$.

Fig. 4.28, this relative difference is plotted for the reactants in their vibrational ground state. The difference is large for low translational energies and decreases with both energy and quantum number K. Particularly large differences can be observed between $K = 0$ and $K = 1$ (more than 75 % deviation between $E_{\text{trans}} = 400$ and $1000 \, \text{cm}^{-1}$). For $E_{\text{trans}} > 1400 \, \text{cm}^{-1}$, the differences rapidly converge to a K–independent value which rises slowly with energy. At high translational energies, (see Fig. 4.28(b)), this value is in the order of 0.2 % to 0.1 %. A similar situation is found for initial excitation of the umbrella bending mode with one quantum (Fig. 4.29). Here, however, the deviations are much smaller (at most up to 10 % with fast convergence down to values below 1 % for $E_{\text{trans}} > 1000 \, \text{cm}^{-1}$). Note that these values are very similar to those found for the ground state. Analogous observations can be made for other initial states and higher values of K, indicating a universal behavior especially for larger K and higher translational energies.

The difference between the cross sections summed over all K values from the rotating top approximation and from K–shifting are shown in Fig. 4.30. In the latter model, the cross section from Ref. [81], $\sigma^{K=0}$, is shifted by E_{trans}^{K}, omitting the contributions from $K > J$, and the resulting curves are summed up. While the results are very similar qualitatively, in particular for vibrational state $(0, 0, 0)$, the differences are in the order of a factor of 2 (for $(0, 1, 1)$) or even larger (for $(1, 0, 0)$). Consistent with Fig. 4.29, the K–shifting cross sections are larger (they would yield a relative difference of zero instead of a negative value) and the difference rises with energy, i.e. the available values for K. We note that the pronounced structure of the K–shifting cross sections is due to interpolation effects.

Rate Constants

The rate constants calculated according to the theory mentioned above are shown in Fig. 4.31 for the temperature range $10 \, \text{K} < T < 1000 \, \text{K}$, together will two enlarge-
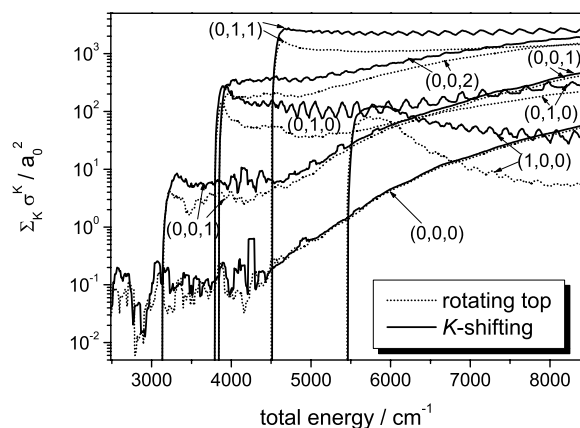
Figure 4.30: Comparison of cumulative state–selected cross sections, summed over all final states and all energetically accessible states with azimuthal rotation labeled by K. The dotted curves represent the data obtained by the rotating top approximation while the solid ones are computed from the cross section for $K = 0$ by adding this curve to itself for every K with the appropriate energy shift, omitting the contributions from $K > J$. The oscillations are due to interpolation effects. All curves are averaged over $80\,\mathrm{cm}^{-1}$.

ments (from 50 and 285 K, respectively, to 1000 K). In addition to our reduced–dimensionality quantum treatment, we also present results obtained with the J– and K–shifting models, with all CH_3Cl rotations excluded and from transition state theory (TST) with two different potential surfaces. Except for the RD quantum curve, the results in Fig. 4.31(a) have already been presented in Ref. [81]. Note that the "red. dim. quantum" curve from this reference is labeled here by "K–shifting, lower resolution". Despite the extreme computational effort of the calculations we now have further increased the energetic resolution down to $10^{-1}\,\mathrm{cm}^{-1}$. All curves show a linear Arrhenius behavior in both the high and low temperature regimes with a slope greater in magnitude in the first limit which is characteristic for a reaction with tunneling through a single barrier [115].

In Fig. 4.31(b), the influence of J–shifting and K–shifting is shown. While increasing the resolution has quite a strong effect on the rate constant below room temperature, inclusion of K via the RTA has only a small effect, yielding a very slight decrease of the rate constant, i.e. farther away from the experimental value. Thus, the azimuthal rotation is of minor influence in this system in accordance with the expectation from the overall small decrease of the cross sections in the RTA model (cf. Fig. 4.30). J–shifting, on the contrary, leads to significantly lower rate constants in all temperature ranges. These findings strongly support our conclusions drawn in Ref. [81] that (a) J–shifting is not appropriate for complex–forming reactions and (b) that rotations (j
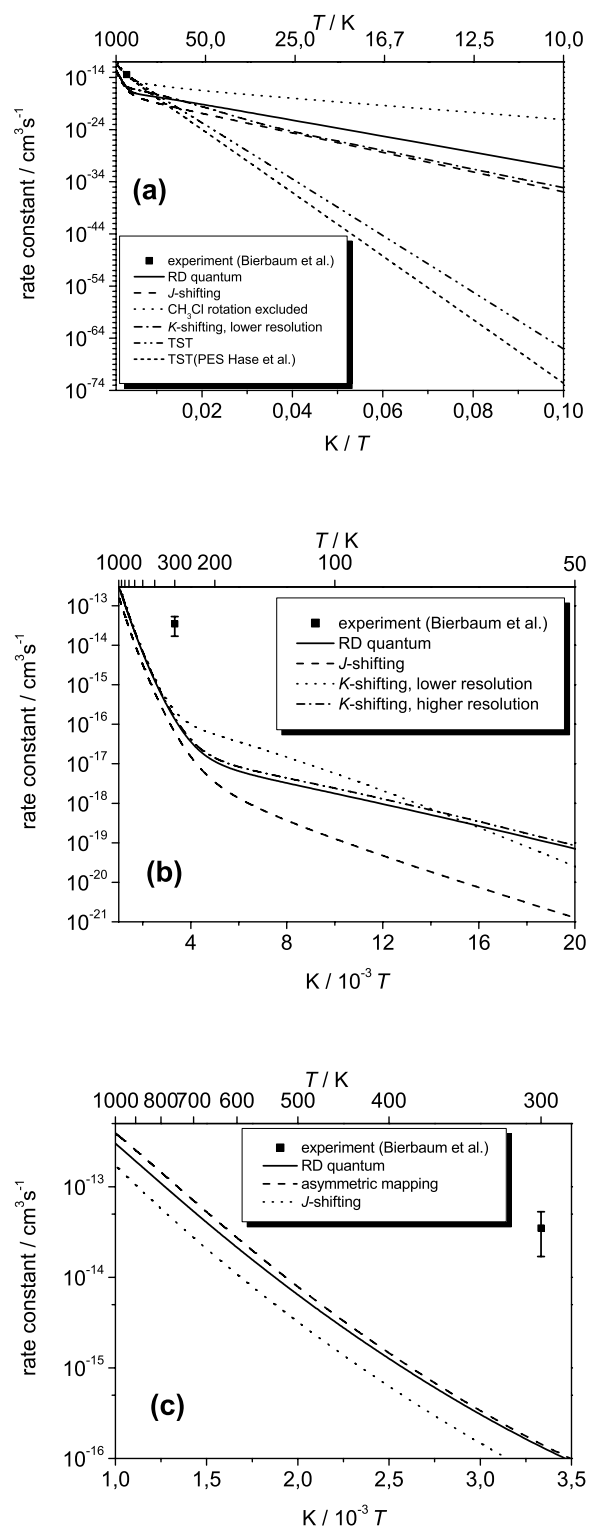
Figure 4.31: Thermal rate constants for the gas–phase S_N2 reaction $Cl^- + CH_3Cl' \rightarrow$ $ClCH_3 + Cl'^-$. Eight different models are applied (for a description see the text).

rotations of the reactant and product symmetric tops) play a crucial role in the system. For chemically relevant temperatures starting from 250 K, the results from K–shifting and RTA are almost indistinguishable on the given scale and resolution effects become negligible.

It remains to study the influence of the asymmetric modes (i.e.,the higher–frequency doubly–degenerate C–H stretching and H–C–H bending modes) on the rate constants (see Fig. 4.31(c)). We only present the combination with the RTA model and observe a slight increase of $k(T)$ where this effect becomes somewhat more pronounced for higher temperatures. The effect is significantly smaller than that going from J–shifting to RTA. Consequently, the asymmetric modes will have only a slight effect on the rate constants within this temperature range as they are already expected to be largely overestimated in the asymmetric mapping model [83] and thus their explicit inclusion cannot explain the discrepancy to the experimental value. Note that also the symmetric modes do not yield the dominant contribution to the rate constant (cf. Fig. 4.32).

The influence of asymmetric modes compared to their symmetric counterparts has been studied explicitly by several others. Wang and Bowman found the symmetric stretch of the H_2O molecule in the $OH+H_2 \rightarrow H+H_2O$ reaction to be more populated than the corresponding antisymmetric mode [116], whereas in the $H+C_2H_2 \rightarrow H_2+C_2H$ reaction the antisymmetric C–H stretch showed a higher effectivity to promote the reaction [117]. In the $O+CH_4 \rightarrow OH+CH_3$ reaction which is the most comparable one to our investigations, calculations by Clary and Palma [86] resulted in a smaller reaction probability for the antisymmetric C–H stretch, but of comparable magnitude. Experiments on the $Cl + CH_4 \rightarrow HCl + CH_3$ reaction [118] show almost indistinguishable state–selected differential cross sections and rovibrational distributions when the reactants are excited either in the symmetric or the antisymmetric C–H stretching vibration. However, in all of these reactions the antisymmetric mode is intrinsically coupled to the reaction coordinate which is not the case for our reaction.

In Fig. 4.32, the contributions of the various initial vibrational states to the total rate constant are analyzed in detail. The various curves show a linear Arrhenius behavior within the selected temperature range and a lot of crossings; the ground state itself exhibits two different slopes as does the total rate constant (with a different bridging region, however), cf. Ref. [115]. This is very much different compared to non–complex–forming bimolecular reactions. A comparable system (however with light atoms only), the abstraction reaction between a hydrogen atom and methane/methanol, was recently studied by Kerkeni and Clary with a state–selective analysis of the rate constants [119, 120]. A direct comparison of the overall behavior is difficult because the higher barriers in these reactions cause the relevant interesting features to appear at higher, rarely investigated temperatures, and the smaller number of degrees of freedom considered yields less curves.

The relative contributions of the different initially excited vibrational states are shown in Fig. 4.32(b). The individual curves show a strikingly similar shape. Under thermal conditions, the state with two quanta in the C–Cl stretching mode of the
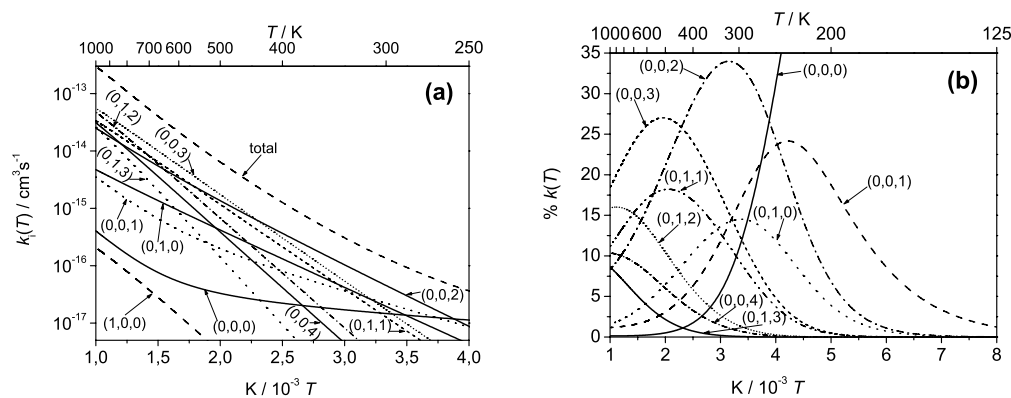
Figure 4.32: Contribution of the individual reactant vibrational states to the thermal rate constant in the reduced–dimensionality quantum model, i.e. summed over all J and K. (a) Absolute state–selected rate constants. (b) Percentage contribution of the reactant vibrational states.

reactant molecule, $(0,0,2)$, contributes most (35 %), followed by the umbrella bend $(0,1,0)$ and one or three quanta in the C–Cl stretch $(0,0,1)/(0,0,3)$ (15 % each). The combination mode $(0,1,1)$ and the vibrational ground state $(0,0,0)$ contribute with 10 % each. In general, excitations with quanta in the umbrella mode contribute less than pure excitations of the C–Cl–bond which is one of the reasons for the low influence of the asymmetric modes (cf. Fig. 4.31(c)). Note that the $(0,0,2)$ mode opens at a total energy of 1432 cm^{-1} above the ground state of CH$_3$Cl which is about seven times larger than the average thermal energy at room temperature. Similar observations hold for other temperatures which infers that fairly high energies are relevant for this reaction because the corresponding modes are much more effective in promoting the reaction as the low–lying ones.

To shed more light on the contribution of different translational energies on the rate constants, we evaluate the ratio $k_E(T)/k_{E_{\max}}(T)$ by computing the corresponding integral up to translational energy E. The quantity $E_{\max}$ denotes the highest energy for which cross sections have been computed in the present work. Results are shown in Fig. 4.33 for three different temperatures (150 K, 300 K and 1000 K). For each temperature, the major contribution to the rate constant stems from an energetic region far above the average thermal energy. At room temperature, about 80 % can be traced back to the translational energy above 1400 cm^{-1} where the $(0,1,0)$ and $(0,0,2)$ modes open up which is consistent with Fig. 4.32. For $T = 1000$ K, we conclude that the value is not fully converged as the slope of the displayed curve does not approach zero for $E_{\max}= 6000$ cm^{-1} which is still nine times as large as the average thermal energy at this temperature. The negative curvature above $E= 5000$ cm^{-1} implies convergence in the order of magnitude, however, which justifies the inclusion of
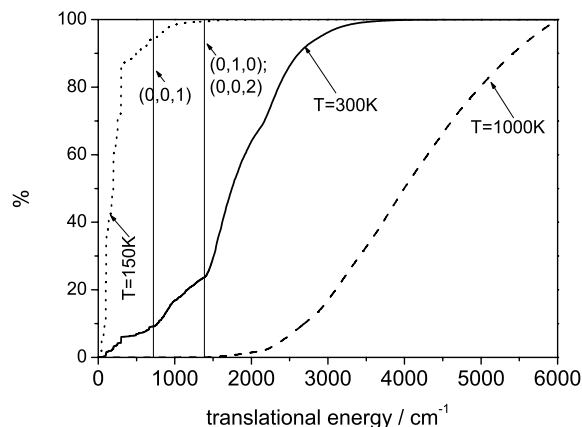
Figure 4.33: Contribution of different translational energies to the rate constants at $T = 150$ K, $T = 300$ K and $T = 1000$ K. For each temperature, the graph shows the ratio $k_E(T)/k_{E_{\max}}(T)$, where $k_E(T)$ is obtained by cutting the corresponding integral at translational energy E and $E_{\max}$ is the highest translational energy for which cross sections have been computed. Opening of the first three stretching modes $(0,0,1)$, $(0,1,0)$ and $(0,0,2)$ is indicated by the vertical lines.

these high temperatures in our plots.

In Fig. 4.34, the cumulative contributions c of angular momenta to the rate constant are given as a function of $1/T$. The unusual scaling of the ordinate results from plotting $100\% - c$ on a logarithmic scale in order to demonstrate the deviation of the RTA/RLA–model from J–shifting; in the latter model, the resulting curves are straight lines as inferred by the rotational partition function. For each model, two different temperature regimes are shown. If curves are not labeled, the maximum value of J increases by ten for each curve from the first to the last corresponding label. For temperatures starting at $T = 10$ K, we observe a very irregular pattern and several jumps with respect to the individual contributions of the total angular momenta. These features cannot be attributed to a physical origin, but are consequences of the limited energy grid size: The individual probabilities $P^J(E)$ do not have a fully resolved resonance structure, resulting in under/overweighing of the individual contributions. Anyway, summation of these yields results that are also reliable for low temperatures in the order of magnitude: Even for the most striking irregularity at $T = 50$ K where the large gap between $J = 140$ and $J = 150$ is clearly due to the energy resolution, the contribution of $J \leq 140$ is still 50 %. The increasing importance of higher angular momenta shows a clear deviation from the linear behavior in the J–shifting which for values from $T = 100$ K up to room temperature is due to the dominant contributions of energetically higher modes; the smaller amount of kinetic energy left in these modes
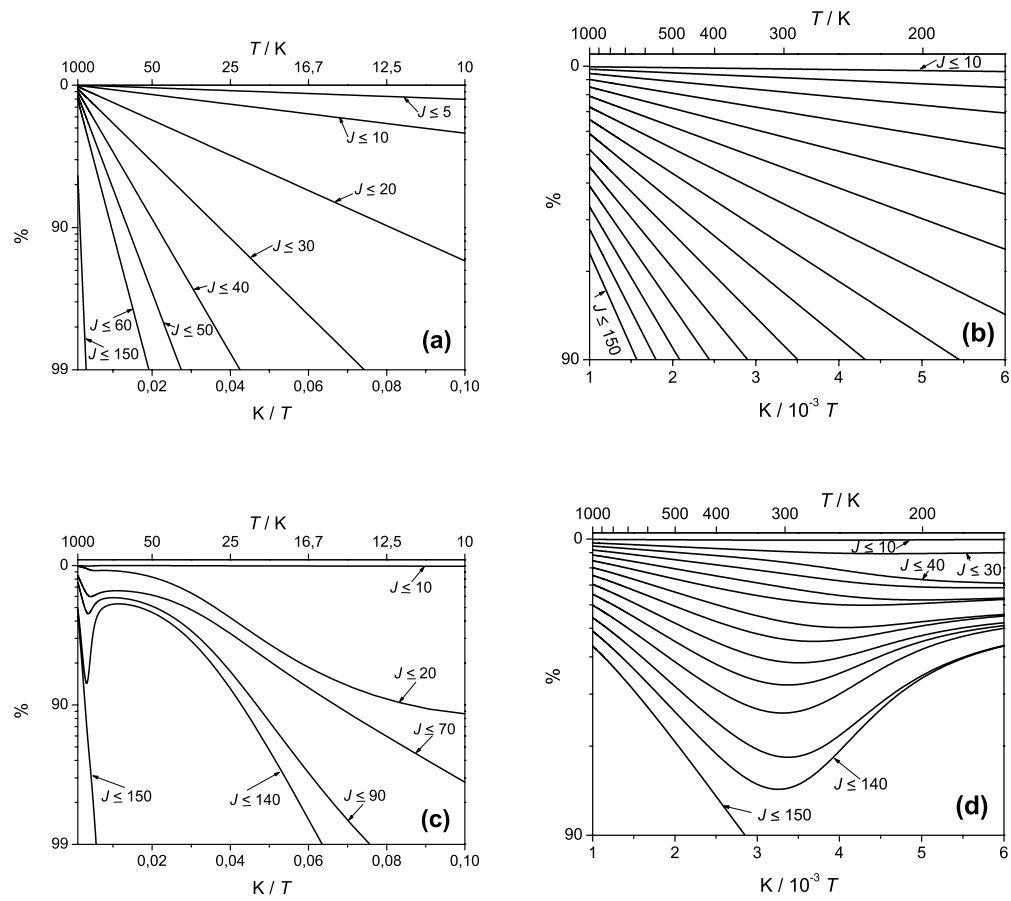
Figure 4.34: Cumulative contribution c of angular momenta to the rate constant as a function of $1/T$ (see the text). (a) and (b) refer to J–shifting, whereas (c) and (d) contain the analogous data for the RTA/RLA–model.

favors smaller angular momenta. Starting from $T = 250$ K, the distances of the curves become increasingly regular indicating less importance of the energy resolution in this temperature region, consistent with Fig. 4.31. Above $T = 400$ K, the curves become straight lines as in the J–shifting model with the only difference that more angular momenta contribute to the final value. This observation, which is valid also for the low temperature regime, explains the overall lower rate constants obtained by J–shifting.

4.3.4   Conclusions

(1) Based on Bowman's adiabatic rotation approximation in quantum reactive scattering, the rotating top approximation is introduced that allows for explicit consideration of the rotational quantum number K in reduced–dimensionality calculations for reactions with true symmetric top geometries during the entire collision process.

(2) Time–independent quantum scattering calculations have been carried out for the S_N2 reaction $Cl^- + CH_3Cl' \rightarrow ClCH_3 + Cl'^-$ using hyperspherical coordinates describing the bonds being broken and formed. The two totally symmetric modes of the methyl group are included in the model and C_{3v} symmetry is conserved throughout the reaction. Making use of the rotating top approximation, converged state–to–state selected total reaction cross sections, summed over all K–rotor contributions, could be calculated.

(3) The thermal rate constant has been calculated and compared with the ones obtained from more approximate models (J–shifting/K–shifting quantum and transition state theory). While TST rate constants show fortuitous good agreement with experiment, the physically more sound reduced–dimensionality quantum calculations show large deviations from the only available experimental data point.

(4) Contributions of the individual K quantum numbers in the rotating top approximation have been analyzed and found to decrease the cross sections in an overall small amount compared to K–shifting. The resulting differences of the rate constants are negligible with respect to the order of magnitude.

(5) A new model has been proposed to estimate the influence of asymmetric modes when quantum results for the symmetric counterpart are available, indicating a negligible influence on the rate constant at room temperature.

(6) State–selected and energy–dependent rate constants have been analyzed. The results underline the importance of certain energetically high–lying modes even at low temperatures, especially those with excitations in the C–Cl–bond.

(7) An analysis of the contribution of the different total angular momenta showed the convergence for small temperatures to occur only via summation. The lower rate constants of J–shifting could be traced back to contributions of higher angular momenta.
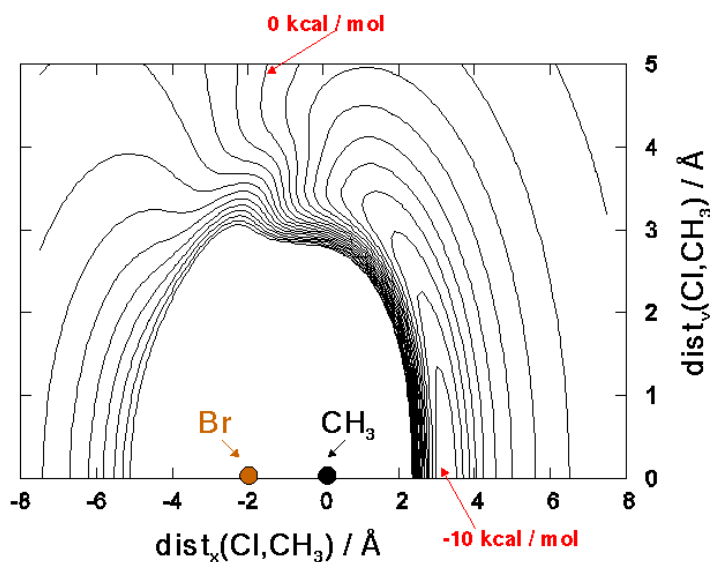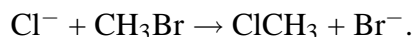
Figure 4.35: Potential "seen" by the chloride ion with the bromine atom and the methyl group in their equilibrium position according to the surface of Hase *et al.* [98].

4.4   Rotational Effects in the Cl–Br Reaction

In this section, we show first results on the quantum mechanical treatment of rotation in the exothermic Cl–Br exchange reaction

$$Cl^- + CH_3Br \rightarrow ClCH_3 + Br^-.$$

The Hamiltonian (2.12) is used at total angular momentum $J = 0$; the dynamical degrees of freedom are the Jacobi coordinates R and r (transformed to hyperspherical coordinates) and the angle γ.

4.4.1   Potential Energy Surface

The potential energy surface employed has been derived from the full dimensional potential energy function by Hase and coworkers [98]. The remaining degrees of freedom have been minimized "on the fly" using the algorithm praxis [121]. Fig. 4.35 depicts the potential resulting from keeping the bromine nucleus and the methyl group at the $Cl^- \cdots CH_3Br$ geometry and varying the position of the chlorine atom. The deep potential well shows the possible range for angular vibration for the front–side attack, whereas back–side attack is energetically unfavorable.

Fig. 4.36 graphically displays the potential for the surface Hamiltonian in hyperspherical coordinates in the coordinate system using the chlorine–carbon system as a diatom for different values of the hyperradius ρ. For small values of the hyperradius,
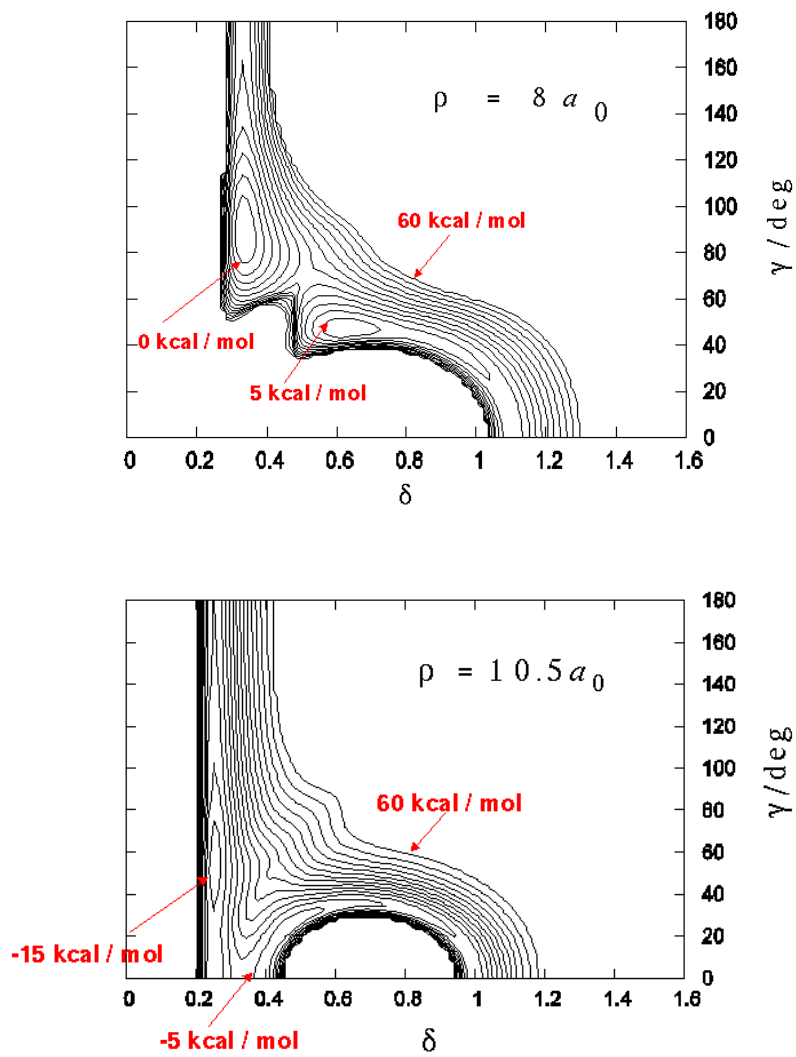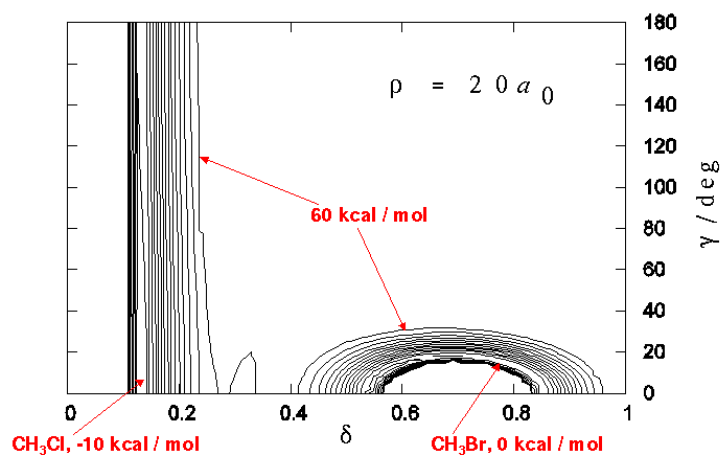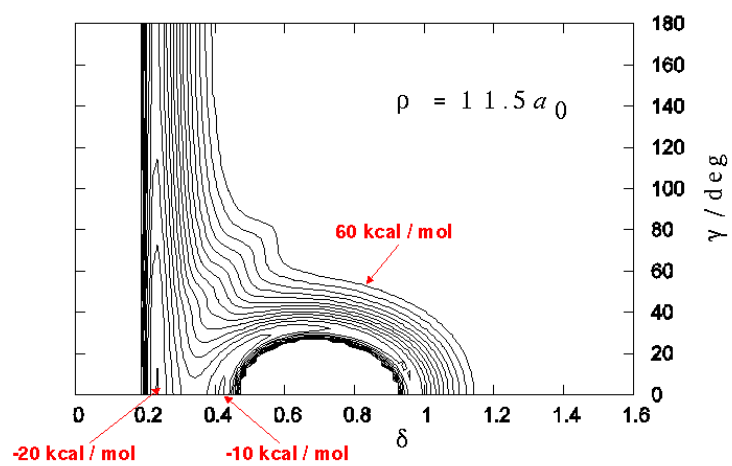
Figure 4.36: Cuts through the same potential energy surface as in figure 4.35 for fixed values of the hyperradius ρ.

the equilibrium geometry is not collinear, but T–shaped. The situation changes with increasing hyperradius. This gives rise to two different types of ground states depending on the value of the reaction coordinate, and the crossing of these can clearly be seen in the hyperspherical adiabatic curves, Fig. 4.37. For asymptotic values of the hyperradius, the two reaction channels split. Owing to the nature of the coordinates preferring one arrangement, the two asymptotic configurations give rise to completely different shapes in the potential energy surface.

4.4.2 Numerical Details

We employed the Hamiltonian (2.12) in hyperspherical coordinates at total angular momentum $J = 0$ with the chlorine–carbon entity treated as the diatom. The method of **R**–matrix–propagation was used to compute the **S**–matrix. The surface Hamiltonian was diagonalized at distances of $d\rho = 0.1$ between $\rho_{min} = 6.5a_0$ and $\rho_{max} = 20.0a_0$, where in the last sector convergence was checked by recomputing the eigenstates in the other coordinate system (with the bromine–carbon entity treated as the diatom). All channels up to a total energy of $E_{max} = 1500$ cm^{-1} have been computed and included in the **R**–matrix–propagation (with a maximum number of $N_{ch,max} = 1061$ channels). No averaging of the final reaction probabilities w.r.t. ρ was used due to the rapidly changing number of channels. The final **S**–matrix was computed at energy intervals of $\Delta E = 15$ cm^{-1}.

The basis for the matrix representation of the Hamiltonian was constructed by a PODVR (see Sec. 3.5) in both the hyperangle δ and the physical angle γ. For the latter, the construction of the reference Hamiltonian needs some consideration as it contains a rotational constant depending on the hyperangle δ:

$$\hat{H}_{ref}^{rot} = \underbrace{\frac{\hbar^2}{2}\left(\frac{1}{\mu\rho^2\cos^2\delta} + \frac{1}{\mu\rho^2\sin^2\delta}\right)}_{:= B(\delta)} j(j+1) + V_{ref}(\gamma). \qquad (4.8)$$

We could have used a different constant $B(\delta(\gamma))$ for each value of gamma; for example, one could choose the hyperangle $\delta(\gamma)$ to be the value where $V(\gamma, \delta(\gamma)) = V_{ref}(\gamma)$. This would lead to an operator that is not symmetric. It can easily be symmetrized, but we found it nevertheless to be superior to use the minimum rotational constant $B_{min} := \min_{\delta^{PO}} B(\delta^{PO})$ for all values of γ where δ^{PO} denotes the collocation points in the hyperangle δ (the collocation basis in this coordinate needs to be constructed first). $N_\delta = 1000$ primitive sinc–collocation functions were used and $N_\gamma = 1400$ Legendre polynomials for $\rho \leq 15.1a_0$; for $15.1a_0 \leq \rho \leq 20a_0$, this number was increased to $N_\gamma = 1900$. The final sector–dependent potential optimized basis in each coordinate was constructed from all corresponding collocation functions below a certain energy. For the hyperangle δ, we set this energy E_{PO}^δ to $E_{PO}^\delta = E_{max} + E_{add}^{PO}$ with $E_{add}^{PO} = 6000$ cm^{-1}; for the coordinate γ, the analogous quantity E_{PO}^γ was com-
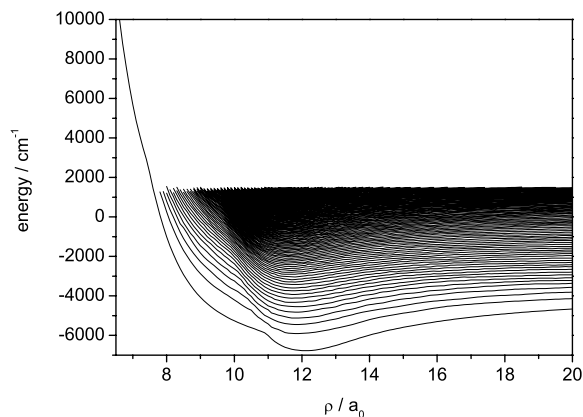
Figure 4.37: Hyperspherical adiabatic curves. Shown is every tenth eigenvalue of the surface Hamiltonian as a function of ρ.

puted from

$$E_{PO}^{\gamma} = \max_{\delta^{PO}} \frac{B_{min}}{B(\delta^{PO})} \left(E_{ref}^{\gamma} - V_{ref}(\delta^{PO})\right)_{+} + V_{min} \qquad (4.9)$$

where $V_{ref}(\delta)$ is the minimum of the potential in the corresponding sector with the value δ of the hyperangle kept fixed, $V_{min} := \min_{\delta^{PO}} V_{ref}(\delta^{PO})$, $E_{ref}^{\gamma} = E_{PO}^{\delta}$ in this calculation and $x_{+} := \max(x,0)$ for any real number x.

The cutoff energy V_{cut} was chosen to be $V_{cut} = 21000\,\text{cm}^{-1}$. The eigenvectors were computed by the Lanczos algorithm with partial reorthogonalization (Sec. 3.6.2) using the convergence criterion (3.89) and $\varepsilon = 10^{-6}$.

4.4.3   Results

Fig. 4.37 shows the hyperspherical adiabatic curves, where for clarity only a tenth of the eigenvalues has been included in the plot. The rapidly increasing density of the eigenstates with energy becomes apparent. An interesting feature is the crossing of the curves at $\rho \approx 11a_0$ due to the ground state changing to collinear geometry. Below that value, a non–collinear state will define the minimum energy configuration. Consequently, for small hyperradii $\rho \leq 8a_0$, a collinear treatment yields practically infinite energies while inclusion of the coordinate γ provides lower eigenstates which are finally T–shaped. In this way, we obtain an additional reaction mechanism without inversion of the methyl group (at still large energies, however).

Fig. 4.38 shows initial state–selected probabilities $P_i(E)$ as functions of translational energy E_{trans}. The curves are labeled with the initial number v of quanta in the C–Br stretching vibration and the angular quantum number j of the diatom (which at this distances still corresponds to a vibration). Most striking is the increase of the
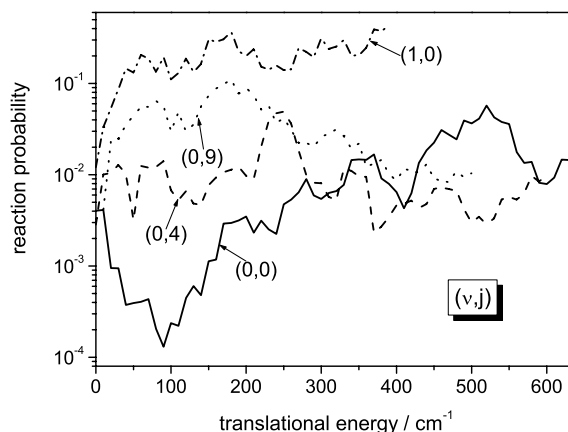
Figure 4.38: Initial state–selected probabilities $P_i(E)$ as functions of translational energy E_{trans}. The data is smoothed over intervals of 80 cm^{-1}. $P_{i,f}(E)$ is summed over all accessible product channels f.

reaction probability with the angular quantum number j. This points to an efficient transfer of rotational energy to the reactive degrees of freedom, in agreement with our conclusions from the previous sections.

To compare the collinear and three–dimensional results, Fig. 4.39 contains the initial state–selected probabilities $P_i(E)$ for two common states from the previous collinear calculations, the ground state $v = 0$ and the first excited state of the C–Br stretching vibration $v = 1$. In addition, the states with $v = 0$ (with $j = 0$) and $j = 9$ (with $v = 0$) from the three–dimensional calculations have been included. While there is no significant enhancement of the reaction probability in the ground state, the situation is clearly different for the $v = 1$ state. The $j = 9$ already shows reaction probabilities comparable to those for the $v = 1$ state in the collinear calculations, clearly pointing to the importance of this degree of freedom for the reaction. The larger variation of the three–dimensional reaction probabilities is purely technical (due to a larger spacing of the points for which values have been obtained).

To obtain an estimate for the quality of the convergence of the data w.r.t. the hyperradius ρ, Fig. 4.40 shows a comparison with reaction probabilities obtained by computing the **S**–matrix at $\rho = 15.1a_0$ (where the wavefunctions in the two arrangement configurations already do not overlap). The clear enhancement of both the $v = 0$ and the $v = 1$ probabilities can be attributed to the long range nature of the potential and indicates the importance of evaluating the **S**–matrix at asymptotic regions of the configuration space. (This might be of some importance for the computation of rate constants for high particle densities when the mean free path drops below the value where the reactants can be considered free). In conjunction with established projec-
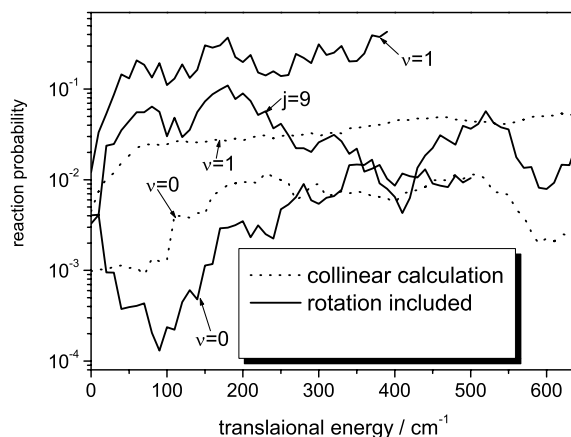
Figure 4.39: Comparison of initial state–selected probabilities $P_i(E)$ as functions of translational energy E_{trans} for a collinear calculation and the present one including rotation. The data is smoothed over intervals of 80 cm^{-1}. $P_{i,f}(E)$ is summed over all accessible product channels f.
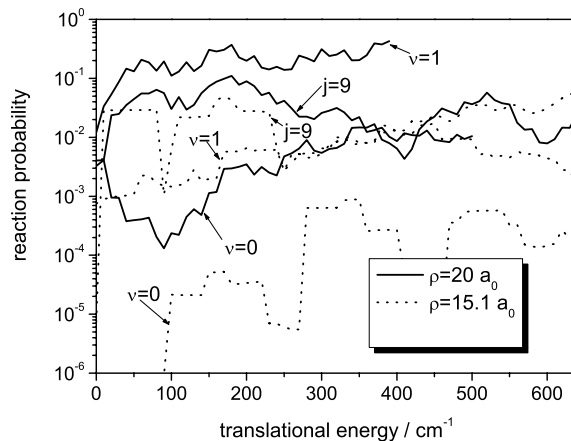

Figure 4.40: Comparison of initial state–selected probabilities $P_i(E)$ as functions of translational energy E_{trans} for evaluating the final **S**–matrix at $\rho = 15.1a_0$ and $\rho = 20a_0$. The data is smoothed over intervals of 80 cm^{-1}. $P_{i,f}(E)$ is summed over all accessible product channels f.

tion techniques for the **S**–matrix, the algorithmic implementations in the present work open up the window for such calculations.

Chapter 5

Summary and Outlook

In this thesis, the S_N2 mechanism was investigated on a quantum mechanical level by means of time–independent scattering theory. Two model systems were considered, the thermoneutral chlorine–chlorine exchange reaction and the exothermic chlorine– bromine substitution.

For the first time, all degrees of freedom within C_{3v} symmetry were treated exactly in four–dimensional calculations. It could be shown that the umbrella bending motion and the C–H stretching vibration do not behave as spectator modes, but actively take part in the reaction and enhance the reaction probability. Despite chemical intuition, the contrary is reported for the umbrella bending motion in the literature. For the C–H stretching vibration, this effect could be traced back to long–lived resonances during the formation of the complex in comparison with filter–diagonalization studies. By a specific algorithm, resonance linewidths were obtained in the scattering calculations which varied over ten orders of magnitude. For the carbon–halogen stretching vibration, a saturation effect was observed which could be explained by an overstretching of the bond beyond the optimal transition state geometry. Simultaneous excitation of the carbon–halogen stretching vibration and the umbrella bending motion resulted in a strong increase of the reaction probability due to the correspondence of this excitation to the transitional normal mode.

A detailed analysis of the cross sections and rate constants has been carried out. Different levels of approximation for the angular momenta involved and the remaining vibrational degrees of freedom have been investigated, using a new model for the asymmetric vibrations of the methyl group. State–selective analysis of the rate constants confirmed our conclusions about the influence of the symmetric vibrational modes in the S_N2 process. Comparison with experimental data indicated that the rotation of the attacked methyl halide should be investigated on a quantum mechanical level as could be already inferred from trajectory calculations.

For that purpose, algorithms for a spatially three–dimensional treatment of an S_N2 reaction have been developed. While in the literature there is an abundance of results for light three–atom systems with short range potentials, starting with collinear models on $H+H_2$ [122, 123] to a state–selective comparison of theoretical and experimental

differential cross sections [124], the present work represents the first investigation of rotational effects in a heavy six–atom system with long–range interaction potentials on a quantum mechanical time–independent level. The results point indeed to an enhancement of the reaction probability with an excitation of the angular degree of freedom. Computations of state–selective differential cross sections are now within reach and together with promising advances in the experimental setup [125] a better understanding of the $S_N 2$ mechanism becomes feasible.

Acknowledgements

Bibliography

[1] W. L. Hase, *Science* **266**, 998 (1994).

[2] M. L. Chabinyc, S. L. Craig, C. K. Regan and J. I. Brauman, *Science* **279**, 1882 (1998).

[3] J. K. Laerdahl and E. Uggerud, *Int. J. Mass Spectrom. Ion Proc.* **214**, 277 (2002).

[4] S. Schmatz, *Chem. Phys. Chem.* **5**, 600 (2004).

[5] Retrieved December 8, 2005, from Wikipedia, The Free Encyclopedia, on the World Wide Web: *http://de.wikipedia.org/wiki/Bild:Adrenalin3d.PNG* and *http://de.wikipedia.org/wiki/Bild:Biosynthese_Adrenalin.png*

[6] C. L. Gee, J. D. A. Tyndall, G. L. Grunewald, Q. Wu, M. J. McLeish and J. L. Martin, *Biochemistry* **44**, 16875 (2005).

[7] W. N. Olmstaed and J. I. Brauman, *J. Am. Chem. Soc.* **99**, 4219 (1977).

[8] J. A. Dodd and J. I. Brauman, *J. Phys. Chem.* **90**, 3559 (1986).

[9] J. I. Brauman, *J. Mass Spectrom.* **30**, 1649 (1995).

[10] S. E. Barlow, J. M. VanDoren and V. M. Bierbaum, *J. Am. Chem. Soc.* **110**, 7240 (1988).

[11] S. Kato, G. E. Davico, H. S. Lee, C. H. Depuy and V. M. Bierbaum, *Int. J. Mass Spectrom.* **210/211**, 223 (2001).

[12] A. A. Viggiano, R. A. Morris, J. S. Paschkewitz and J. F. Paulson, *J. Am. Chem. Soc.* **114**, 10477 (1992).

[13] J.-L. Le Garrec, B. R. Rowe, J. L. Queffelec, J. B. A. Mitchell and D. C. Clary, *J. Phys. Chem.* **107**, 1021 (1997).

[14] V. F. DeTuri, P. A. Hintz and K. M. Ervin, *J. Phys. Chem.* **101**, 5969 (1997).

[15] K. M. Ervin, *Int. J. Mass Spectrom.* **187**, 343 (1999).

[16] L. A. Angel and K. M. Ervin, *J. Phys. Chem. A* **105**, 4042 (2001).

[17] L. A. Angel, S. P. Garcia and K. M. Ervin, *J. Am. Chem. Soc.* **124**, 336 (2002).

[18] L. A. Angel and K. M. Ervin, *J. Am. Chem. Soc.* **125**, 1014 (2003).

[19] R. Wester, A. E. Bragg, A. V. Davis and D. M. Neumark, *J. Chem. Phys.* **119**, 10032 (2003).

[20] S. R. Vande Linde and W. L. Hase, *J. Chem. Phys.* **93**, 7962 (1990).

[21] Y. J. Cho, S. R. Vande Linde, L. Zhu and W. R. Hase, *J. Chem. Phys.* **96**, 8275 (1992).

[22] W. L. Hase and Y. J. Cho, *J. Chem. Phys.* **98**, 8626 (1993).

[23] G. H. Peslherbe, H. Wang and W. L. Hase, *J. Chem. Phys.* **102**, 5626 (1995).

[24] G. H. Peslherbe, H. Wang and W. L. Hase, *J. Am. Chem. Soc.* **118**, 257 (1996).

[25] D. J. Mann and W. L. Hase, *J. Phys. Chem. A* **102**, 6208 (1998).

[26] T. Su and W. L. Hase, *J. Phys. Chem. A* **102**, 9819 (1998).

[27] G. S. Li and W. L. Hase, *J. Am. Chem. Soc.* **121**, 7124 (1999).

[28] K. Y. Song, L. P. Sun and W. L. Hase, *J. Am. Chem. Soc.* **123**, 5753 (2001).

[29] S. C. Tucker and D. G. Truhlar, *Chem. Phys. Lett.* **157**, 164 (1989).

[30] Y. Wang, W. L. Hase and H. Wang, *J. Chem. Phys.* **118**, 2688 (2003).

[31] S. Schmatz and D. C. Clary, *J. Chem. Phys.* **110**, 9483 (1999).

[32] S. Schmatz, P. Botschwina, J. Hauschildt and R. Schinke, *J. Chem. Phys.* **117**, 9710 (2002).

[33] J. Makarewicz, *J. Phys. B: At. Mol. Opt. Phys.* **21**, 1803 (1987).

[34] J. R. Henderson, S. Miller and J. Tennyson, *J. Chem. Soc. Faraday Trans.* **86**, 1963 (1990).

[35] G. C. Schatz, *Chem. Phys. Lett.* **150**, 92 (1988).

[36] D. C. Clary, *J. Chem. Phys.* **95**, 7298 (1991).

[37] J. Echave and D. C. Clary, *J. Chem. Phys.* **100**, 402 (1994).

[38] S. K. Pogrebnya, J. Echave and D. C. Clary, *J. Chem. Phys.* **107**, 8975 (1997).

[39] A. Kuppermann, J. A. Kaye and J. P. Dwyer, *Chem. Phys. Lett.* **74**, 257 (1980).

[40] J. Römelt, *Chem. Phys. Lett.* **74**, 263 (1980).

[41] B. Podolsky *Phys. Rev.* **32**, 812 (1918).

[42] F. T. Smith, *Phys. Rev.* **118**, 349 (1960).

[43] M. S. Child, *Molecular Collision Theory* (Dover, New York, 1996).

[44] R. T. Pack and G. A. Parker, *J. Chem. Phys.* **87**, 3888 (1987).

[45] K. Museth and A. Kuppermann, *J. Chem. Phys.* **115**, 8285 (2001).

[46] E. B. Stechel, R. B. Walker and J. C. Light, *J. Chem. Phys.* **69**, 3518 (1978).

[47] C. Canuto, M. Y. Hussaini, A. Quarteroni and T. A. Zang, *Spectral Methods in Fluid Dynamics* (Springer Verlag, New York, 1988).

[48] R. N. Ashcroft, *Asset Pricing with Spectral Methods*, (Stanford, PhD Thesis, 1995).

[49] D. O. Harris, G. G. Engerholm and W. D. Gwinn, *J. Chem. Phys.* **43**, 1515 (1965).

[50] A. S. Dickinson and P. R. Certain, *J. Chem. Phys.* **49**, 4209 (1968).

[51] H. Wilf, In *Mathematics for the Physical Sciences* (John Wiley & Sons, Inc., New York, 1962), Chapter 2.

[52] J. Echave and D. C. Clary, *Chem. Phys. Lett.* **190**, 225 (1992).

[53] D. T. Colbert and W. H. Miller, *J. Chem. Phys.* **96**, 1982 (1992).

[54] G. C. Groenenboom and D. T. Colbert, *J. Chem. Phys.* **99**, 9681 (1993).

[55] G. H. Golub and J. Welsch, *Math. Comp.* **23**, 221 (1969).

[56] W. Gautschi, *Math. Comp.* **24**, 245 (1970).

[57] D. Baye and P. H. Heenen, *J. Phys. A: Math. Gen.* **19**, 2041 (1986).

[58] R. G. Littlejohn and P. Wright, *J. Math. Phys.* **43**, 4668 (2002).

[59] V. Szalay, G. Czakó, Á. Nagy, T. Furtenbacher and A. G. Csázár, *J. Chem. Phys.* **119**, 10512 (2003).

[60] J. C. Light and T. Carrington Jr., *Adv. Chem. Phys.* **114**, 263 (2000).

[61] N. L. Carothers, *A Short Course on Approximation Theory* (Lecture Notes, Department of Mathematics and Statistics, Bowling Green State University, 1998).

[62] M. J. Bramley and T. Carrington Jr., *J. Chem. Phys.* **99**, 8519 (1993).

[63] J. P. Boyd, *Chebyshev and Fourier Spectral Methods* (Second Edition, Dover, New York, 2001).

[64] R. Jaquet, *Comput. Phys. Commun.* **58**, 257 (1990).

[65] A. G. Abrashkevich, D. G. Abrashkevich, M. S. Kashiev and I. V. Puzynin, *Comput. Phys. Commun.* **85**, 40 (1995).

[66] H. Wei, *J. Chem. Phys.* **106**, 6885 (1997).

[67] R. G. Littlejohn, M. Cargo, T. Carrington Jr., K. A. Mitchell and B. Poirer, *J. Chem. Phys.* **116**, 8691 (2002).

[68] J. C. Light, I. P. Hamilton and J. V. Lill, *J. Chem. Phys.* **82**, 1400 (1984).

[69] R. B. Lehoucq, D. C. Sorensen and C. Yang, *ARPACK Users' Guide: Solution of Large–Scale Eigenvalue Problems with Implicitly Restarted Arnoldi Methods* (SIAM, Philadelphia, 1998).

[70] Z. Bai and R. Li, In *Templates for the Solution of Algebraic Eigenvalue Problems*; D. Bai, J. Demmel, J. Dongarra, A. Ruhe, H. von der Vorst, Ed. (SIAM, Philadelphia, 2000), p. 106.

[71] C. Davis and W. Kahan, *III. SIAM J. Numer. Anal.* **7**, 1 (1970).

[72] G. W. Stewart and J. G. Sun, *Matrix Pertubation Theory* (Academic Press, New York, 1990).

[73] C. Lanczos, *J. Res. Natl. Bur. Stand.* **45**, 255 (1950).

[74] H. D. Simon, *Math. Comput.* **42**, 115 (1984).

[75] H. G. Yu, G. Nyman, *Chem. Phys. Lett.* **298**, 27 (1998).

[76] G. L. G. Sleijpen and H. A. van der Vorst, *SIAM J. Matrix Anal. Appl.* **17**, 401 (1996).

[77] E. R. Davidson, *J. Comput. Phys.* **17**, 87 (1975).

[78] C. C. Page and M. A. Saunders, *SIAM J. Numer. Anal.* **12**, 617 (1975).

[79] C. Hennig and S. Schmatz, *J. Chem. Phys.* **121**, 220 (2004).

[80] P. Botschwina, C. Hennig and S. Schmatz, *Phys. Chem. Chem. Phys.* **6**, 4630 (2004).

[81] C. Hennig and S. Schmatz, *Phys. Chem. Chem. Phys.* **7**, 1552 (2005).

[82] C. Hennig and S. Schmatz, *J. Chem. Phys.* **122**, no. 234307 (2005).

[83] C. Hennig and S. Schmatz, *J. Phys. Chem. A* **110**, 1524 (2006).

[84] C. Hennig, R. B. Oswald and S. Schmatz, *J. Phys. Chem. A* **110**, 3071 (2006).

[85] J. Palma and D. C. Clary, *J. Chem. Phys.* **112**, 1859 (2000).

[86] J. Palma and D. C. Clary, *Phys. Chem. Chem. Phys.* **2**, 4105 (2000).

[87] H. G. Yu and G. Nyman, *J. Chem. Phys.* **112**, 238 (2000).

[88] M. S. Child, *Mol. Phys.* **12**, 401 (1967).

[89] S. Schmatz and D. C. Clary, *J. Chem. Phys.* **109**, 8200 (1998).

[90] M. I. Hernández, J. Campos-Martinez, P. Villarreal, S. Schmatz, and D. C. Clary, *Phys. Chem. Chem. Phys.* **1**, 1197 (1999).

[91] D. C. Clary and J. Palma, *J. Chem. Phys.* **106**, 575 (1997).

[92] H. G. Yu and G. Nyman, *Chem. Phys. Lett.* **312**, 585 (1999).

[93] S. Schmatz, P. Botschwina, J. Hauschildt and R. Schinke, *J. Chem. Phys.* **114**, 5233 (2001).

[94] S. Schmatz and J. Hauschildt, *J. Chem. Phys.* **118**, 4499 (2003).

[95] J. L. Duncan and M. M. Law, *J. Mol. Spectrosc.* **140**, 13 (1990).

[96] S. Schmatz, *Chem. Phys. Lett.* **330**, 188 (2000).

[97] S. R. Vande Linde and W. L. Hase, *J. Phys. Chem.* **94**, 2778 (1990).

[98] H. Wang, L. Zhu and W. L. Hase, *J. Phys. Chem.* **98**, 1608 (1994).

[99] H. Zhang and S. C. Smith, *J. Chem. Phys.* **115**, 5751 (2001).

[100] H. Wang, E. M. Goldfield and W. L. Hase, *J. Chem. Soc. Faraday Trans.* **93**, 737 (1997).

[101] S. Schmatz, H. Stoll and P. Botschwina, *Int. J. Mass Spectr. Ion Proc.* **291**, 277 (2000).

[102] S. Schmatz, *J. Chem. Phys.* **122**, no. 234306 (2005).

[103] S. T. Graul and M. T. Bowers, J. Am. Chem. Soc. **113**, 9696 (1991).

[104] S. T. Graul and M. T. Bowers, J. Am. Chem. Soc. **116**, 3875 (1994).

[105] G. Herzberg, *Molecular Spectra and Molecular Structure. II. Infrared and Raman Spectra of Polyatomic Molecules* (Van Nostrand Reinhold, New York, 1945).

[106] J. M. Bowman, *Adv. Chem. Phys.* **65**, 61 (1985).

[107] J. M. Bowman and A. F. Wagner, In *The Theory of Chemical Reaction Dynamics*; D. C. Clary, Ed. (Reidel: Dordrecht, 1986), p. 47.

[108] R. B. Walker and E. F. Hayes, In *The Theory of Chemical Reaction Dynamics*; D. C. Clary, Ed. (Reidel: Dordrecht, 1986), p. 105.

[109] J. M. Bowman, *J. Chem. Phys.* **95**, 4960 (1991).

[110] J. M. Bowman and D. Wang, In *Advances in Molecular Vibration and Collision Dynamics*; J. M. Bowman, Ed. (JAI, Greenwich, 1994, Vol. II B), p. 187.

[111] F. N. Dzegilenko and J. M. Bowman, *J. Chem. Phys.* **105**, 2280 (1996).

[112] J. M. Bowman, *Chem. Phys. Lett.* **217**, 36 (1994).

[113] J. M. Bowman, *J. Phys. Chem. A* **102**, 3006 (1998).

[114] J. M. Bowman, *Theor. Chem. Acc.* **108**, 125 (2002).

[115] R. P. Bell, *Proc. R. Soc. A* **139**, 466 (1933).

[116] D. Wang, and J. M. Bowman, *J. Chem. Phys.* **96**, 8906 (1992).

[117] D. Wang and J. M. Bowman, *J. Chem. Phys.* **101**, 8646 (1994).

[118] H. A. Bechtel, J. P. Camden, D. J. Ankeny Brown and R. N. Zare, *J. Chem. Phys.* **120**, 5096 (2004).

[119] B. Kerkeni and D. C. Clary, *J. Chem. Phys.* **120**, 2308 (2004).

[120] B. Kerkeni and D. C. Clary, *J. Chem. Phys.* **121**, 6809 (2004).

[121] R. P. Brent, *Algorithms for Minimization without Derivatives* (Prentice–Hall, 1973); program available from a.cs.okstate.edu in the /pub/jpc directory.

[122] E. M. Mortensen and K. S. Pitzer, Chem. Soc. (London), *Spec. Publ.* **16**, 57 (1962).

[123] D. G. Truhlar and A. Kuppermann, *J. Chem. Phys.* **52**, 3841 (1970).

[124] S. D. Chao, S. A. Harich, D. X. Dai, C. C. Wang, X. Yang and R. T. Skodje, *J. Chem. Phys.* **117**, 8341 (2002).

[125] J. Mikosch, U. Frühling, S. Trippel, D. Schwalm, M. Weidemüller and R. Wester, *Phys. Chem. Chem. Phys.* **8**, 2990 (2006).

Lebenslauf

Dipl.–Phys. Carsten Hennig, M.S. (USA)
geboren am 17.4.1974 in Hamburg
Staatsangehörigkeit: deutsch

09/1980 – 06/1993	Schulbesuch in Isernhagen; Abitur
10/1993 – 09/1994	Wehrdienst
10/1994 – 07/1999	Studium der Physik und der Mathematik an der Universität Göttingen
07/1996	Vordiplom in Mathematik
10/1996	Vordiplom in Physik
07/1997 – 10/2000	Stipendiat der Studienstiftung des deutschen Volkes
07/1999	Diplom in Physik mit einer Diplomarbeit in theoretischer Physik
08/1999 – 07/2000	Mathematikstudium an der Michigan State University (USA); Master of Science in Mathematics
10/2000 – 06/2002	Wissenschaftlicher Mitarbeiter an der Universität Göttingen
seit 10/2002	Doktorand in theoretischer Chemie an der Universität Göttingen